

SEASONAL CIRCULATION AND THERMOHALINE STRUCTURE OF
THE CASPIAN SEA

A THESIS SUBMITTED TO
THE GRADUATE SCHOOL OF MARINE SCIENCES
OF
THE MIDDLE EAST TECHNICAL UNIVERSITY

BY

MURAT GÜNDÜZ

IN PARTIAL FULFILLMENT OF THE REQUIREMENTS
FOR
THE DEGREE OF DOCTOR OF PHILOSOPHY
IN
THE DEPARTMENT OF PHYSICAL OCEANOGRAPHY

FEBRUARY 2008

Approval of the thesis

**“SEASONAL CIRCULATION AND THERMOHALINE
STRUCTURE OF THE CASPIAN SEA”**

submitted by **Murat Gündüz** in partial fulfillment of the requirements for
the degree of **Doctor of Philosophy in Physical Oceanography** by,

Prof. Dr. Ferit Bingel _____
Director, **Graduate School of Marine Sciences**

Prof. Dr. Emin Özsoy _____
Head of Department, **Physical Oceanography**

Prof. Dr. Emin Özsoy _____
Supervisor, **Institute of Marine Sciences, METU**

Examining Committee Members:

Prof. Dr. Temel Oğuz _____
Institute of Marine Sciences, METU

Prof. Dr. Emin Özsoy _____
Institute of Marine Sciences, METU

Assoc. Prof. Dr. Zahit Uysal _____
Institute of Marine Sciences, METU

Prof. Dr. Mehmet Karaca _____
Eurasia Institute of Earth Sciences, ITU

Assoc. Prof. Dr. Rashit Ibrayev _____
Institute of Numerical Mathematics, RAS of Russia

Date: _____

I hereby declare that all information in this document has been obtained and presented in accordance with academic rules and ethical conduct. I also declare that, as required by these rules and conduct, I have fully cited and referenced all material and results that are not original to this work.

Name, Last name : Murat Gündüz

Signature :

ABSTRACT

SEASONAL CIRCULATION AND THERMOHALINE STRUCTURE OF THE CASPIAN SEA

Gündüz, Murat

Ph.D., Department of Physical Oceanography

Supervisor: Prof. Dr. Emin Özsoy

February 2008, 146 pages

A high resolution ocean model (HYCOM) was designed to investigate the seasonal circulation, and the building blocks of the mesoscale dynamics of the Caspian Sea. The model was able to reproduce the main oceanographic characteristics of the sea, namely, upwelling along the eastern coast, southward current along the eastern and western coasts, cyclonic circulation in the Middle Caspian Sea (MCS) during winter, two-gyre structure in the South Caspian Sea (SCS) with an anticyclonic cell northwest of the basin, and a cyclonic in the southeast, dense water formation near the northern shelf zone and mesoscale structure of the sea. The model also reproduced the observed seasonal variability of sea level and sea surface temperature (SST) climatology.

Three experiments have been designed beside the control run to investigate the relative effects of wind stress and river runoff on the circulation characteristics of the sea: (1) barotropic sea, no thermal fluxes; (2) baroclinic sea, no thermal fluxes; (3) twin of control run but no river runoff. By comparing the

results of these three experiments it is shown that baroclinicity is an important factor for the generation of the cyclonic/anticyclonic cell in the MCS and SCS. Rivers is also important as it intensify the cyclonic/anticyclonic gyres in both basins.

Keywords: Caspian Sea, HYCOM, seasonal circulation

ÖZ

HAZAR DENİZİNİN MEVSİMSEL SİRKÜLASYONU VE TERMAL YAPISI

Gündüz, Murat

Doktora, Fiziksel Oşinografi Bölümü

Tez Yöneticisi: Prof. Dr. Emin Özsoy

Subat 2008, 146 sayfa

Yüksek çözünürlüklü bir okyanus modeli (HYCOM) Hazar denizinin mevsimsel sirkülasyonunu ve temel mezoscale dinamiklerini incelemek için dizayn edildi. Model denizin temel oşinografik özelliklerini, doğu kıyısındaki upwelling, doğu ve batı kıyılarıdaki güneyli akıntıları, Orta Hazar Denizindeki (OHD) kışın oluşan siklonik sirkülasyonu, güney hazardaki iki-döngülü sistemi (basenin kuzeybatısında antisisiklon ve güney doğusunda siklon), kuzey sığlığında yoğun su oluşumunu ve denizin mezoscale durumunu, başarıyla taklit etmiştir. Model aynı zamanda gözlemlenen deniz seviyesi ve deniz yüzey sıcaklığının mevsimsel değişiminide başarıyla taklit etmiştir.

Rüzgar stresi ve nehir akısının Hazar denizinin sirkülasyon rejimi üzerine etkisini anlamak için kontrol deneyinin yanı sıra üç deney daha dizayn edildi, bunlar; (1) termal flux yokken barotropic deniz (2) termal flux yokken baroclinic deniz (3) kontrol deneyinin ikizi fakat nehir girdisi yok. Bu deneylerin sonuçlarını karşılaştırarak, baroclinicity'nin siklon/antisiklon hücrelerinin

oluşumunda önemli olduğu gösterilmiştir. Nehir girdisi her iki basende siklon/antisiklon dönüşlerinin şiddetini arttıran önemli bir faktördür.

Anahtar Kelimeler: Hazar Denizi, HYCOM, mevsimsel sirkülasyon

ACKNOWLEDGMENTS

This study was supported by the NATO SfP Project No 981063 "Multidisciplinary Analysis of the Caspian Sea Ecosystem" (MACE).

TABLE OF CONTENTS

ABSTRACT	iv
ÖZ	vi
ACKNOWLEDGMENTS	viii
TABLE OF CONTENTS	ix
LIST OF FIGURES	xii
LIST OF TABLES	xx
LIST OF SYMBOLS	xxii
CHAPTER	
1 INTRODUCTION	1
2 REVIEW OF REGIONAL CHARACTERISTICS	7
2.1 Caspian Sea Level Change	7
2.2 Atmospheric Circulation	8
2.3 Sea Surface Temperature (SST) variability	11
2.4 Circulation	14
2.5 Upwelling	17
2.6 Dense Water Formation	19
3 THE DATA AND MODEL	23
3.1 The Data	23
3.1.1 Sea Surface Temperature	23
3.1.2 MODIS chlorophyll concentration	24

3.1.3	Sea Level Anomaly	24
3.1.4	Drifters	25
3.2	Model Characteristics and Setup	25
3.2.1	The HYbrid Coordinate Ocean Model (HYCOM)	25
3.2.2	Caspian Sea Model	28
3.3	Float Package	43
4	MODEL VALIDATION	45
4.1	Model comparison with Pathfinder SST	45
4.2	Model comparison with satellite derived sea surface height	50
4.3	Comparison to Climatological observations	52
5	ANNUAL MEAN AND SEASONAL ANALYSIS	56
5.1	Circulation	56
5.2	Temperature	67
5.3	Mesoscale Circulations	71
5.3.1	Mesoscale Features in the Northern and Middle Caspian Sea	74
5.3.2	Mesoscale Features in the Southern Caspian Sea	78
5.3.3	High Frequency Variability	90
5.4	Upwelling	92
5.5	Dense Water Formation	98
5.5.1	Effect of Freshwater and E-P on MLD	107
5.5.2	Float Experiments	110
6	SENSITIVITY EXPERIMENTS	115
6.1	Buoyancy effect	116
6.2	Effects of wind stress and baroclinicity	118
7	LARGE SCALE CONTROLS	123
7.1	A possible link between North Sea Caspian Pattern (NCP) and SST over the Caspian Sea	123

8 CONCLUSIONS	127
REFERENCES	132
VITA	143

LIST OF FIGURES

FIGURES

Figure 1.1	The land topography of the Euro-Asian-Mediterranean Region including the Caspian Sea region, showing mountain chains, flat areas, national borders and rivers. . . .	2
Figure 2.1	Yearly mean values of the Caspian Sea level measured by sea level gauges (1837-2004)	8
Figure 2.2	Mean Sea Level Pressure distribution pattern (hPa) for winter (December-January-February) period of 1948-2007. Iceland low and Azore high are evident in the figure, Siberian high pressure is seen in red colour near the eastern boundary of the plot.	9
Figure 2.3	Mean Sea Level Pressure distribution pattern (hPa) for summer (June-July-August-September) period of 1948-2007. Strong Azores high and Tibetan low are evident. . .	10
Figure 2.4	Climatological monthly mean (January through December) AVHRR Pathfinder SST ($^{\circ}C$).	12
Figure 2.5	Schematic representation of the Caspian Sea currents (Lednev, 1943)	14
Figure 2.6	Energy spectrum of time variability for currents at levels of 200m as recorded by moored station off the Apsheron peninsula. Obtained from Kosarev and Yablonskaya, 1994	17

Figure 2.7	AVHRR SST ($^{\circ}C$) on 17 July 2001	18
Figure 2.8	Cross section (see inset for the location of the section) of salinity (psu) in the Caspian Sea (a) August 1976 and (b) September 1995. From Kostianoy and Kosarev 2005.	21
Figure 3.1	The Caspian Sea bathymetry (m) and the model coastline used in the HYCOM simulations. The model land-sea boundary is the 4 m isobath which is shown with light brown in color. The Kara Bogaz Gol is excluded in the model simulations	31
Figure 3.2	Annual mean of basin averaged climatological monthly mean temperature and salinity profiles obtained from Russian data set.	32
Figure 3.3	Climatological SST $^{\circ}C$ based on hydrographic observa- tions in February and July	34
Figure 3.4	Climatological SSS (psu) based on hydrographic observa- tions in February and July	34
Figure 3.5	Climatological upper: temperature $^{\circ}C$, lower: salinity (psu) section based on the hydrographic observartions along the $50^{\circ}E$ in July.	35
Figure 3.6	Climatological momentum fluxes averaged over the Caspian Sea from ERA-40 Re-Analysis	36
Figure 3.7	Climatological monthly mean wind stress fields (N/m ²) over the Caspian Sea from January through December calculated by using ERA-40 Re-Analysis data set and interpolated to the model grid.	37
Figure 3.8	Climatological monthly mean surface heat fluxes aver- aged over the Caspian Sea from ERA-40 Re-Analysis	38

Figure 3.9	Climatological monthly mean precipitation (m/s) fields over the Caspian Sea from January through December calculated by using ERA-40 Re-Analysis data set and interpolated to the model grid.	41
Figure 4.1	Annual mean model SST mean bias ($^{\circ}C$) and RMS difference ($^{\circ}C$) with respect to the satellite-based Pathfinder SST climatology	47
Figure 4.2	Climatological monthly mean model SST Mean Error ($^{\circ}C$) with respect to the Pathfinder SST climatology which has a resolution of 4km. upper figures: From January June, lower figures: From July to December	49
Figure 4.3	Skill score	50
Figure 4.4	Model and satellite based Sea Level Anaomaly (SLA) (m) in January. Note the different scale in each figure.	52
Figure 4.5	Model and satellite based Sea Level Anaomaly (SLA) (m) in August. Note the different scale in each figure.	53
Figure 4.6	Comparison of observed (upper figure) and modelled temperatures $^{\circ}C$ along the $51^{\circ}E$ transect for the month of August.	54
Figure 4.7	Basin averaged model and climatology temperature $^{\circ}C$ at depths of 0, 10, 50, 150 m. Solid lines are climatology from observation, red triangles are model temperature.	55
Figure 5.1	Model-derived annual mean currents (cms^{-1}) from control run averaged over depth intervals of 0-30 m, 30-150 m and 150-300 m. Red lines shows the 100, 200, 300 m bathymetry contours.	58
Figure 5.2	Model derived monthly circulation from control run averaged over the 0 to 30m, 30 to 150m and 150 to 300m for December	59

Figure 5.3	Model derived monthly circulation from control run averaged over the 0 to 30m, 30 to 150m and 150 to 300m for May	60
Figure 5.4	Model derived monthly circulation from control run averaged over the 0 to 30m, 30 to 150m and 150 to 300m for August	61
Figure 5.5	Schematic representation of annual mean circulation of the Caspian Sea for the depth ranges (a) Surface (0-10 m), (b) Intermediate (50-100 m) (c) Deep (200-1000 m). . .	64
Figure 5.6	Climatological monthly mean barotropic stream function (m^3/s) over the Caspian Sea from January through December	66
Figure 5.7	Vertical cross-section of the annual mean alongshore currents along (m/s^{-1}) the (a) center of the MCS, (b) Apsheron peninsula (c) $38^{\circ}E$ and (d) $39.5^{\circ}E$	68
Figure 5.8	Model derived monthly mean temperature at $50^{\circ}E$ from January through December.	70
Figure 5.9	Model derived eddy kinetic energy (cm^2/s^2) map at first model level during (a) January and (b) August. The white contours are the bathymetric contours from 100 m to 300 m with 100 m interval.	73
Figure 5.10	Eddy Kinetic energy (m^2/s^2) along the $50^{\circ}E$ transect in January and August	75
Figure 5.11	Model derived current in July over the MCS. The southward flow along the north-eastern coast of the MCS is evident in this figure.	76
Figure 5.12	Sea Surface Salinity (SSS) for a series of model days 210, 212, 213, 214, 215, 221.	77

Figure 5.13 Sequence of chlorophyll concentration (in mgm^{-3}) on 27,29,30 July and 1,2,8 August of the year 2004. The chlorophyll concentration contours are plotted with different colours and intervals for a better visualization of structure.	79
Figure 5.14 Sequence of chlorophyll concentration (in mgm^{-3}) 29 June and 1,4,7,8,9 July of the year 2005. The chlorophyll concentration contours are plotted with different colours and intervals for a better visualization of structure.	80
Figure 5.15 The evolution of the flow field in the SCS during (a) 15 (b) 45 (c) 75 (d) 105 (e) 135 (f) 165 days of the model days overlain on current magnitude	83
Figure 5.16 The evolution of the flow field in the SCS during (a) 195 (b) 225 (c) 255 (d) 285 (e) 315 (f) 345 days of the model days overlain on current magnitude	84
Figure 5.17 Sequence of chlorophyll concentration (in mgm^{-3}) on 18,19,20,21,22,26 August of the year 2006. The chlorophyll concentration contours are plotted with different colours and intervals for a better visualization of structure.	85
Figure 5.18 Snapshot of model derived SST ($^{\circ}C$) at model day of 70, the black line shows the 100 m bathymetry contour. The strong temperature gradient is evident at the shelfbreak separating the shelf water from the slope inner water. The unstable motions, meanders along the black line are also evident in this figure.	87
Figure 5.19 The trajectory arising from September 2007 deployment. Dot indicate the deployment site.	88
Figure 5.20 The trajectory arising from September 2007 deployment. Dot indicate the deployment site.	89

Figure 5.21 The trajectory arising from September 2007 deployment. Dot indicate the deployment site.	90
Figure 5.22 Spectra of u component of current at 5 m, at $52^{\circ}E$, $42^{\circ}N$, this point was chosen since there is a observational spec- tra near this location, offshore of the Apsheron peninsula.	91
Figure 5.23 Snapshot of the model SST ($^{\circ}C$) of the 8th model year. The model days are shown at upper left side of the each figure.	93
Figure 5.24 Howmoeller plots of sea surface temperature ($^{\circ}C$) aver- aged over $40^{\circ} - 42^{\circ}N$. X axis is the longitude and y axis is time.	94
Figure 5.25 August alongshore currents (north-south) in the upwelling region averaged over $41^{\circ} - 44^{\circ}N$. Positive (negative) means toward to north (south).	95
Figure 5.26 (a) V-velocity (m/s), (b) salinity (psu) and density evolu- tion during the model annual cycle at 5 m at the station $51^{\circ}E$, $43.4^{\circ}N$. X axis is model annual cycle (366 days).	96
Figure 5.27 August temperature and cross-shore (east-west) currents in the upwelling region averaged over $41^{\circ} - 44^{\circ}N$	97
Figure 5.28 ECMWF wind-stress curl averaged over $41^{\circ} - 44^{\circ}N$	99
Figure 5.29 Model derived monthly density(sigma) section at $50^{\circ}E$ from January through December.	101
Figure 5.30 Density (sigma) section along the $49.5^{\circ}E$ in February.	102
Figure 5.31 Density of deepest depth at model days 2, 20, 40, 60, 80, 100. white areas shows the density less than 9	103
Figure 5.32 Mixed layer depth (m) of the control run from January to December	105
Figure 5.33 Depth of 9.8 density at the model day 80	106

Figure 5.34 Meridionally averaged south-north cross sections of SST, net heat flux, salinity and Mixed Layer Depth (MLD) along the 50°E in March. The details of the each experiments are explained in the text.	109
Figure 5.35 Float positions released in HYCOM, each float was integrated 30 days. The floats released again at the same location in each months. The floats can move in three dimension.	111
Figure 5.36 Float paths, color-coded to reveal monts, red is December, green is January and yellow is February. Each float was integrated 30 days. The floats can move in three dimension.	112
Figure 5.37 Float pats, color-coded to reveal monts, red is December, green is January and yellow is February. Each float was integrated 30 days. The floats can move in three dimension.	113
Figure 5.38 Float paths, color-coded to reveal depths along the paths, in July. The numbers indicate the release points of the floats. Each float was integrated 30 days. The floats can move in three dimension. The contours in the figure show the 20 m and 50 m depth.	114
Figure 6.1 Model surface velocity vector mean and rms vector amplitude over the year simulation, with rivers and without rivers. Means are denoted with arrows while rms amplitude is color contoured. Every fourth vector is shown in the along-shore and across-shore direction.	117
Figure 6.2 Circulation pattern averaged over different depth intervals in February for the four experiment mentioned in the text, upper figures 0-30m lower figures 30-150m	119

Figure 6.3	Circulation pattern averaged over different depth intervals in August for the four experiment mentioned in the text, upper figures 0-30m lower figures 30-150m	120
Figure 7.1	Correlation coefficients between moving averaged SST with 2 points and NCP index for the time period from February to May	125
Figure 7.2	Meridional dependence of the correlation coefficient between zonally averaged SST of the Caspian Sea and the NCP index	126
Figure 7.3	Time series of SST averaged meridionally and over the $36 - 38^{\circ}N$ (i.e southern Caspian Sea) ,blue triangles, and NCP index red dots. The time series was also moving averaged with a 2 point	126

LIST OF TABLES

TABLES

Table 3.1	Constant parameter values used in the HYCOM Caspian Sea simulations. In the ocean interior, the contribution of background internal wave breaking, shear instability mixing, and double diffusion (both salt fingering and diffusive instability) are parameterized by the KPP model. In the surface boundary layer, the influence of wind-driven mixing, surface buoyancy fluxes, and convective instability are parameterized. The KPP algorithm parameterizes the influence of nonlocal mixing of temperature and salinity, which permits the development of countergradient fluxes.	30
Table 3.2	Climatological mean flow values obtained from RivDIS (see online at http://daac.ornl.gov/rivdis/), for the river discharge into the Caspian Sea.	42
Table 3.3	HYCOM simulations performed in this thesis to test the influence of wind stress and river input on circulation pattern and buoyancy fluxes on the surface properties of the sea. The model uses climatological wind and thermal forcing (i.e, air temperature at 10 m, air mixing ratio at 10 m, shortwave and longwave radiation) constructed from European Centre for Medium Range Weather Forecasts (ECMWF) re-analysis product.	43

Table 5.1 HYCOM simulations to test riverine input. 108

LIST OF SYMBOLS

MCS	Middle Caspian Sea
NCS	North Caspian Sea
SCS	South Caspian Sea
SST	Sea Surface Temperature
SLA	Sea Level Anomaly

CHAPTER 1

INTRODUCTION

The Caspian Sea extends for about 1200 km in the north-south direction, between 36°34' to 47°13' N and for about 300 km in the east-west direction between 46°38' to 54°44' E. It lies east of the Caucasus mountains, west of the vast steppe of central Asia and north of the Elburz Mountains (Figure 1.1) at the boundary between Europe and Asia. The Caspian Sea is surrounded by continental land masses with has high mountain chains, deserts and flatlands. The sea level of the Caspian Sea is currently 28 m below the mean global sea level.

The relatively large meridional extent ($> 10^\circ$ in latitude) of the Caspian Sea appears to be linked with a strong north-south gradient in its properties. Geographically, the Caspian Sea consists of three distinct basins (north, middle and south regions), each of which has its own physical and biological properties. The Northern Caspian Sea (NCS), north of the line connecting Chechen island to Mangyshlak peninsula, is relatively shallow, with an average depth of approximately 5 m. The Ural Furrow is the only depression (8-10 m) in the otherwise flat continental shelf area of the NCS. This shallow shelf area suddenly deepens at the shelf edge to join the deeper basin of the Middle Caspian Sea (MCS), which has an average depth of 190 m, and a maximum depth of 788 m (at the Derbent depression in the west). The western slope of this basin is quite steep, wheares the eastern slope has a milder slope. The Kara Bogaz Gol, a small enclosure of shallow water connected to the basin

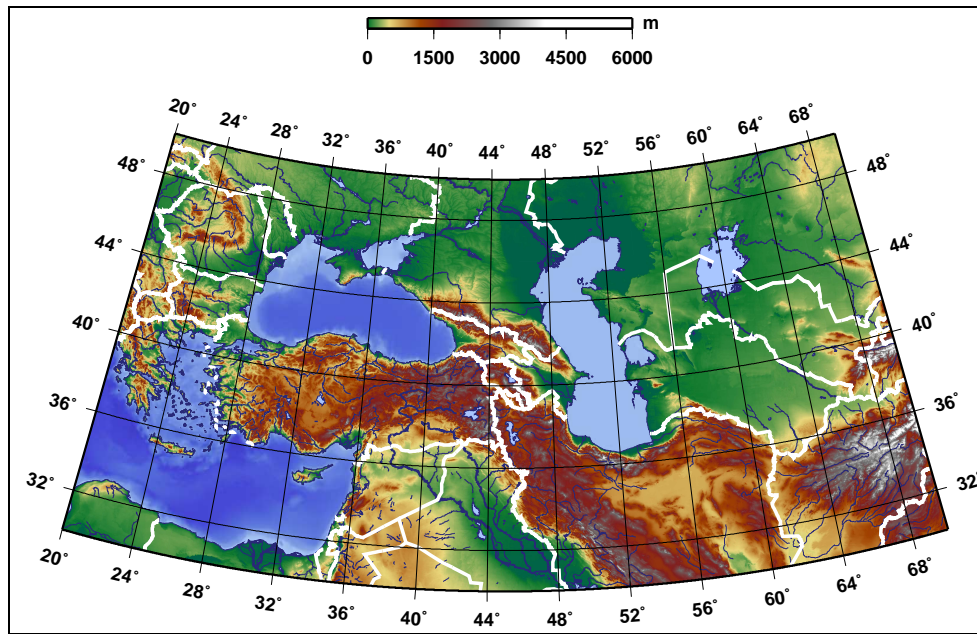


Figure 1.1: The land topography of the Euro-Asian-Mediterranean Region including the Caspian Sea region, showing mountain chains, flat areas, national borders and rivers.

with a narrow channel, is located east of the basin with a maximum depth of 10 m. Finally, the Southern Caspian Sea (SCS) is the deepest basin of the Caspian Sea, with a maximum depth of 1025 m. It is separated from the Middle Caspian by the Apsheron Ridge (connecting Zhiloy island in the west to Cape Kuuli in the east). The bottom topography of Southern Basin inclines to the west, reaching depths of 900 to 1000 m in separate depressions of the same basin. Having such topographical features makes the Caspian Sea an ideal laboratory and a test-bed for studying combined effects of coastal and open ocean processes.

While the NCS accounts for 1/100 of the total volume of the Caspian Sea, the MCS and SCS basins respectively account for about 1/3 and 2/3 of the total volume. The Volga and Ural rivers (respectively accounting for %80 and %5 of fresh water inflow) located in the NCS, and the Kura river (accounting for % 7-8 of the inflow) located in the SCS are the main rivers of the Caspian

Sea. Caspian Sea has brackish waters which is three times less salty than oceanic waters. Salinity sharply changes in the northern part of the sea from 0.1 ‰ in estuaries of the Volga and Ural rivers, to 10-12 ‰ at the border with the Middle Caspian Sea. Middle and Southern Caspian Sea basins have salinities in the range of 12.5-13.5.

At present, the enclosed Caspian Sea is a forgotten component of the global ocean system. It is included neither in the high resolution eddy resolving ocean models nor in the existing operational models. Given the lack of reliable eddy-resolving numerical ocean models for investigating dynamical and physical processes of the Caspian Sea, there is strong motivation to develop one. The Caspian Sea is unique in that the surface heat fluxes, evaporation and precipitation as well as river fluxes have significant influences on surface features and the dynamics of the circulation. In fact, sea level in this region is strongly controlled by seasonal changes in evaporation and precipitation. The latter is related to variations in the amount of North Atlantic depressions reaching the interior, that are in turn affected by cycles of North Atlantic Oscillation (NAO) (Rodinov, 1994). Despite its small size, these factors makes the Caspian Sea a challenging region to study climate effects.

Among many ocean models available today, HYCOM seems to be a good candidate for modeling of the Caspian Sea because of the flexibility of its coordinate system and the physical processes that can be represented in this model. The hybrid coordinate used by HYCOM is isopycnal in the open ocean, but smoothly reverts to a terrain-following coordinate in shallow coastal regions, and to z -level coordinates in the mixed layer or in weakly stratified regions. The optimal coordinate is chosen using a hybrid grid generator at each model time step based on the mass continuity equation (Bleck, 2006). Therefore, the model combines the advantages of different coordinate systems within a single framework to allow for the optimal coordinate choice in simulating coastal and open-ocean features. This flexibility is needed in the Caspian Sea since the hybrid coordinate system extends the geographic range of applicability of the

model from the deep basins continuously towards the shallow coastal regions and unstratified shallow parts of the Caspian Sea. The capability- to switch between z -level, sigma and isopycnic coordinate systems is essential for the Caspian Sea to handle complex interactions between coastal and open ocean, motivated by its specific geometry and bathymetry.

Previously, HYCOM was successfully implemented for the Black Sea, where interactions between coastal and open ocean regions are of interest (Kara et al., 2005b, Kara et al., 2005c) and carry similarities with the Caspian Sea. There are distinct similarities between bathymetries of these enclosed seas, both of which have steep slopes between continental shelf and open ocean regions. The Black Sea has very shallow shelf area in the northwestern part where it receives significant inflow from the Danube river, and similarly the Caspian Sea has a shallow northern shelf which is affected by the Volga River. The Sea of Azov is a relatively small body of water connected to the Black Sea in the northern part, similar to the very shallow northern shelf and the KaraBogaz Gol connected to the Caspian Sea.

The Caspian Sea has other unique characteristics, which make it a very challenging enclosed body of water for ocean modeling: The sea level displays a clear seasonal cycle, reaching its lowest value in winter and highest value during May-July, following the spring floods (Rodinov, 1994). The change in sea level is a function of evaporation minus precipitation and river fluxes, indicating that buoyancy changes associated with freshwater fluxes can be as important as those due to changes in heat flux.

The Caspian Sea has very low salinity (< 13), which is about one third of the typical salinity of seawater over much of the global ocean. In deep water, salinity varies little with depth (Kosarev and Tuzhilkin, 1995), and thermal properties almost totally determine the density stratification. In addition, the existence of extensive shallow regions sensitive to atmospheric forcing in the Caspian Sea points to the importance of properly representing stratification and mixing processes. Since greater constraints need to be imposed in formu-

lation of surface fluxes in an enclosed basin in comparison to semi-enclosed or open ocean domains, improperly accounting for mass or buoyancy fluxes could lead to unrealistic trends of total stored heat, salt and mass in model. Given the fact that sea level change is a direct result of water balance, which depends on river inflows, precipitation and evaporation, reliable determination of buoyancy fluxes due to salt becomes a critical issue in the Caspian Sea. The HYCOM model has demonstrated capability in similar situations and also includes a thermodynamic sea-ice model to be able to simulate ice processes in the northern Caspian Sea.

Using a fully eddy-resolving HYCOM Caspian Sea model, a series of numerical experiments have been carried out to address the following fundamental questions:

- (1) general and mesoscale ocean circulation features during a climatological seasonal cycle,
- (2) the individual roles of buoyancy (fresh water inflow, surface fluxes), winds and topography, barotropic versus baroclinic circulations,
- (3) water mass characteristics, mixing and dense water formation processes,
- (4) upwelling, mainly along the eastern coast.

Neither the reasons for the observed general circulation features of the Caspian Sea nor the above physical processes have been fully examined earlier, making use of eddy-resolving ocean models. We attempt to provide a first glimpse to these unresolved or poorly understood dynamical features of the Caspian Sea.

This thesis is organized as follows: Chapter 2 reviews certain regional characteristics and oceanographic processes in the Caspian Sea. Chapter 3 outlines the available data and describes the model characteristics. In Chapter 4, the model is evaluated by using the available observational data. Chapter 5 details the spatial and temporal variability of the currents derived from the ocean model. A number of sensitivity experiments designed to explore physical processes are discussed in Chapter 6. The influence of the large scale climate

patterns on the sea surface temperature (SST) are investigated in Chapter 7. The main results of the thesis are discussed and recommendations for future investigations are given in Chapter 8.

CHAPTER 2

REVIEW OF REGIONAL CHARACTERISTICS

2.1 Caspian Sea Level Change

Environmental disasters related to sudden changes of the Caspian Sea Level (CSL) constitute a major problem for local communities (Dumont 1995). Figure 2.1 presents Caspian Sea level changes from 1837 to 2004. Large changes in sea level have occurred during the past decades. After decades of decreasing water level from 1930 to 1977, the sea level rapidly began to rise in 1978 and presently it fluctuates near the -27 m level.

Large scale atmospheric circulation patterns such as the El Nino - Southern Oscillation, ENSO, and the North Atlantic Oscillation, NAO and Volga River runoff (which in turn appears strongly related to these atmospheric patterns) are the main factors controlling the sea level in the Caspian Sea. For example, Arpe et al. (2000) have shown an integrated influence of the Southern Oscillation Index, SOI on the Caspian Sea level. On the other hand, Rodionov (1994) has shown the effect of the NAO on the Volga river discharge and consequently on the Caspian Sea level change. Anthropogenic effects, such as the extensive use of Volga water for irrigation, and the build-up surface oil films from oil production activities resulting in a decrease of evaporation, can also be shown to be important factors contributing to the control of the Caspian sea level

fluctuations (Klinge and Myagkov 1992).

Predictability of the Caspian Sea Level (CSL) still remains an elusive matter, in relation to the uncertainty in estimating the total evaporation from the surface of the Caspian Sea, a prominent component of the Caspian Sea water budget.

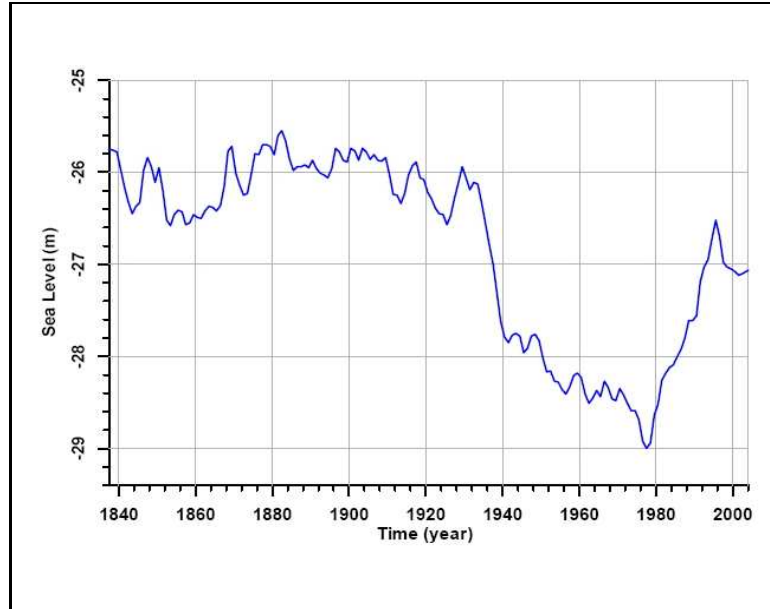


Figure 2.1: Yearly mean values of the Caspian Sea level measured by sea level gauges (1837-2004)

2.2 Atmospheric Circulation

The changes in geographic and the land/sea surface characteristics (across large water bodies and high mountain chains, vast continental flatlands, arid and semi-arid lands) result in very steep climatic gradients in the Southwestern Asia region.

Atmospheric conditions near the Caspian Sea is related to changes in atmospheric circulation in the Atlantic-European sector of Northern Hemisphere.

One of the known patterns governing the winter atmospheric conditions is known as North Atlantic Oscillation (NAO). This pattern characterizes the motions of mid-tropospheric jet-stream over Europe, and therefore represents the eastward extension and the influence over European-Mediterranean region of the NAO pattern originating in the Atlantic sector.

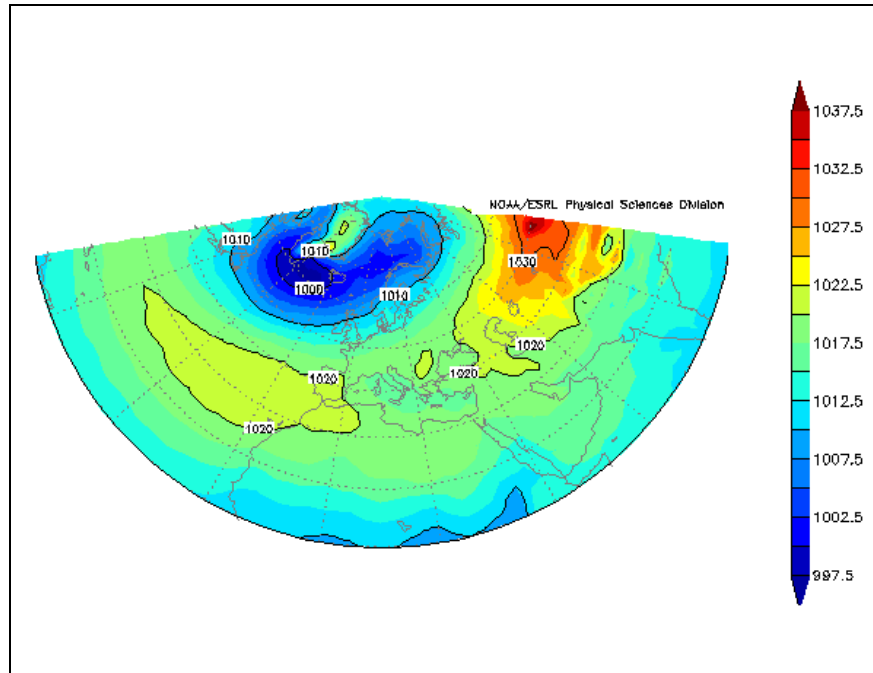


Figure 2.2: Mean Sea Level Pressure distribution pattern (hPa) for winter (December-January-February) period of 1948-2007. Iceland low and Azore high are evident in the figure, Siberian high pressure is seen in red colour near the eastern boundary of the plot.

Atmospheric circulation is important in formation of the sea's hydrometeorological regime in closed Sea like Caspian. Distinctive general circulation of an atmosphere, field of temperature that is created by the sea itself and a relief of its coasts determines the direction and strength of wind blowing over Caspian.

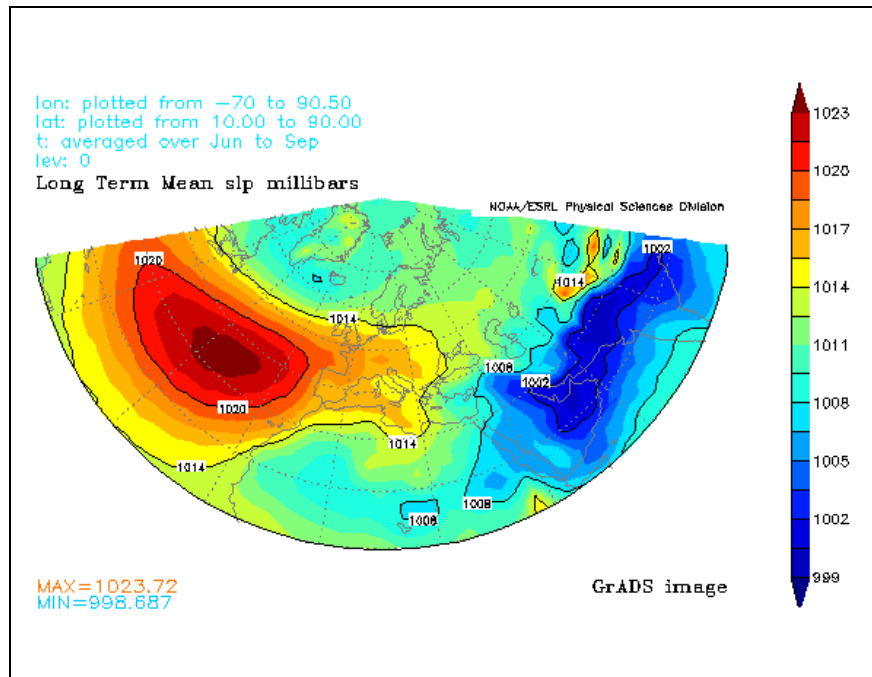


Figure 2.3: Mean Sea Level Pressure distribution pattern (hPa) for summer (June-July-August-September) period of 1948-2007. Strong Azores high and Tibetan low are evident.

Atmospheric circulation over the sea shows very strong seasonal cycle. During the winter, the sea under the influence of Asiatic anti-cyclone (or known as Siberian anti-cyclone, a semipermanent system of high atmospheric pressure centered in northeastern Siberia during the colder half of the year), as clearly seen in Figure 2.2 in red colour near the eastern boundary of the plot. This anti-cyclone creates easterly winds of cold, clear air. Iceland low and Azores high are also evident in winter months. During the summer, the weather is dominated by the Azores high-pressure (Figure 2.3) that causes northerly winds, particularly along its western shore (Nihoul 2004). The Iceland low seems to disappear in winter months. The Tibetan low located south of the Caspian sea and extend to the east (blue color over the south-east part of the figure) present during the summer. As a summary, there are two main atmospheric circulation patterns over the Caspian Sea. First pattern comprises strong northern direction winds (Northwest, North, and Northeast). Northerly

winds are predominant in the course of the year with a probability 41 % with maximum in the summer (Koshinsky, 1960). Second group includes strong southerly winds, cyclonic activity over and to the west of the Caspian Sea causes this type of pattern.

2.3 Sea Surface Temperature (SST) variability

Figure 2.4 shows the climatological monthly mean SST in the Caspian Sea. SST in the Caspian Sea shows strong seasonal variability due to the geographic position of the Sea. Since Caspian Sea elongated in north-south direction, there are three climate regime along its latitude. There is strong temperature gradient from north to south, the SST gradient is about $0.8^{\circ}C$ per degree latitude (Sur and Ozsoy 2000) in winter. SST is rather uniform from north to south in summer.

The timing of the cooling and warming of the basins are different. The fastest cooling and warming is observed in the Northern basin because of the shallowness of the basin. Same is true for the shallow eastern coast of the southern basin. The warmest basin is the southern part and the warmest region in this basin is the shallow eastern coast. In Middle Caspian Sea there is cold water along the eastern coast in summer and early autumn because of the coastal upwelling in the basin. In this basin, relatively cold water is also observed in the western coast in May.

The three basins of the Caspian Sea shows distinct features with respect to cooling/warming period and other thermal structure. The northern basin heats up rapidly in late spring and summer after ice melt and because of its shallowness, reaches very fast the same temperatures as the southern basin, while the central basin lags in heating.

Northern shelf seems to cool first in the eastern part and starts warming in April-May uniformly over the shelf domain, but sometimes warming can occur at coastal areas and center remains colder or warming occurs in the southern

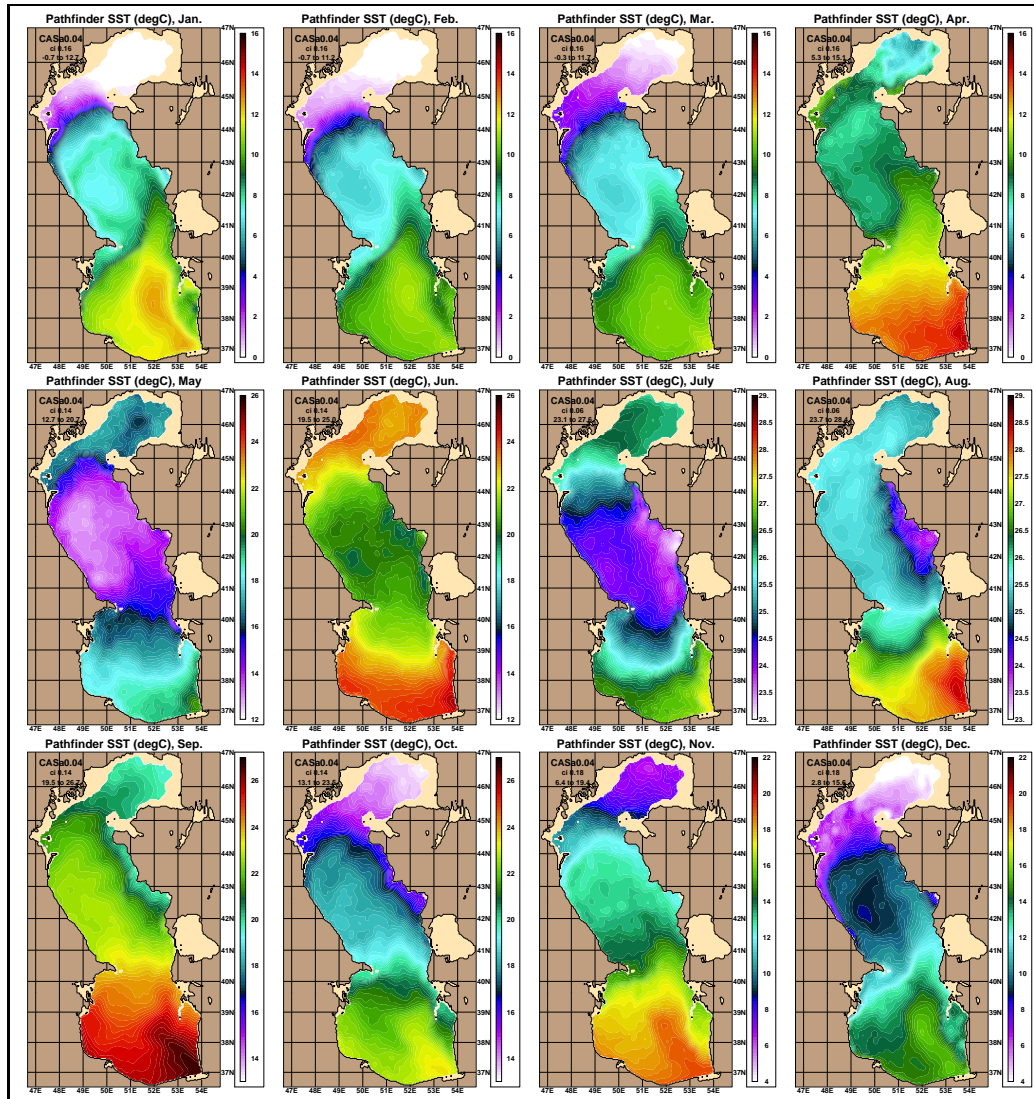


Figure 2.4: Climatological monthly mean (January through December) AVHRR Pathfinder SST ($^{\circ}\text{C}$).

of the north shelf and northern part remains cold. The most striking feature of the Middle Caspian Sea is the upwelling along the eastern coast, most clearly occurs in July-August-September but can also be detected slightly in other times. The timing of maximum upwelling and its center of action changes from year to year (sometimes occur later, and in some years the central part is more active, while in other years it shifts north). The southern basin is always very warm, the eastern part except the easternmost shallow area seems always warmer, the easternmost shallow shelf seems to cool faster in early winter and because of its shallowness, this basin warm up faster to a higher temperature.

There is a curious contrasting vein of warm water sneaking into the upwelling zone from the southern basin toward the middle basin, along the eastern coast, this warm water vein seems to have bypassed the upwelling patch and reach to northern part of the middle basin. Similar intrusion is seen in the northern shelf, cold water from the northern shelf and the Volga along the western shelf extend into the southern basin, past Apsheron peninsula in some years, and remains short of it in some other years.

An important aspect of the Caspian Sea oceanography is the existence of ice, typically formed in the shallow North Caspian Sea region in winter (Kosarev and Yablonskaya, 1994). During severe winters drifting ice is found as far south as the Apsheron peninsula. As expected, sea-ice profoundly modifies the surface heat, mass and momentum exchange, and also alters the radiative and turbulent component of the surface heat balance due to its high albedo and low thermal conductivity. This results in reduction of the absorption of short-wave radiation by as much as 80%, and the turbulent heat fluxes by one to two orders of magnitude. Ice generally forms in mid-November (in mild winters, ice formation starts 20-30 days or more later, while in severe winters it forms 20-30 days earlier) and decays in mid-March. Ice typically disappears in the northeastern part at the beginning of April (Kouraev et al., 2004). Therefore, it is essential to model the seasonal variation of ice related thermodynamics in the Caspian Sea.

2.4 Circulation

There is some uncertainty in constructing seasonal circulation of the Caspian Sea, as short term hydrographic data available mostly in the shelf zones are only sufficient to characterize some synoptic variability of circulation without revealing its essential details. Complexity arising due to strong variability of the atmospheric forcing, its topography, the enclosed geometry of the basin with shallow continental shelves and sills, the combined effects of baroclinicity creates significant challenges for diagnosing the seasonal circulation of the Caspian Sea.

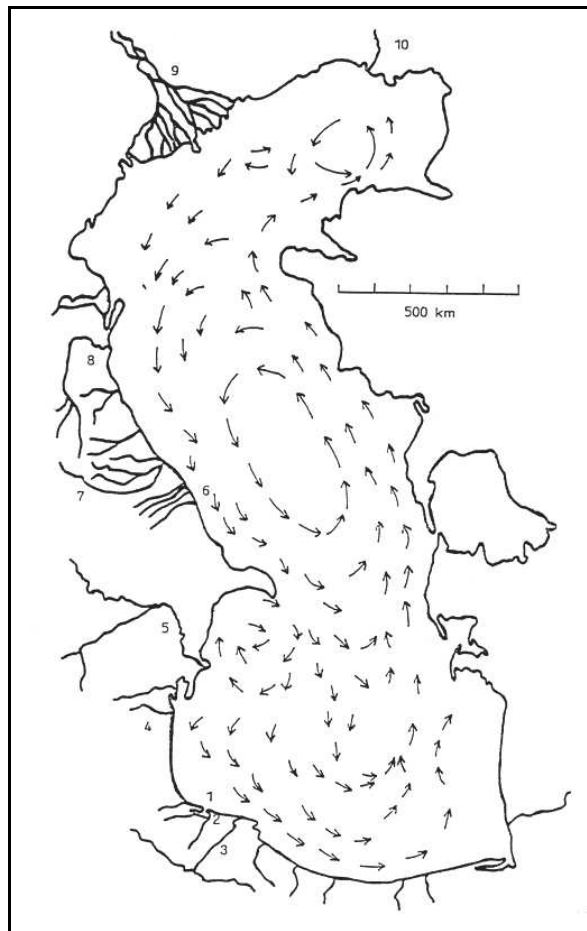


Figure 2.5: Schematic representation of the Caspian Sea currents (Lednev, 1943)

The general circulation detected by the available data from hydrographic surveys from the end of the 19th century till the 1950s has been described to be cyclonic in the Middle Caspian Sea (MCS). The most striking results of the six instrumental surveys along the western coast of the MCS, carried out in 1935-37 (Stockman 1938, Baydin and Kosarev 1986), shows predominantly southward currents along the western coast of the basin.

Data from the regular oceanographic observations since 1950's in coastal areas of the sea have confirmed the above mentioned southward currents along the western coast of the MCS (Klevtsova 1968) and the semi-permanent anti-cyclonic vortex south of the Apsheron peninsula (Tsytsarev 1967). Southward surface currents along the eastern coast of the MCS (Klevtsova 1967, Bondarenko 1993) are also evident in these observations which contradict with the mentioned general cyclonic circulation of the MCS, but below this depicted surface circulation, northward currents are known to exist along the eastern coast of the basin with some seasonal dependence, supporting evidence for the proposed cyclonic circulation. A southward current east of the Apsheron peninsula passing to the southern Caspian Sea is inferred from the hydrographic observations, with currents velocities of $50 - 60\text{cm/s}$ at the surface, decreasing to $40 - 50\text{cm/s}$ near the bottom (Kosarev and Yablonskaya 1994). In the shallow northern Caspian Sea, the circulation appears to be almost totally controlled by local winds (Bondarenko 1992, 1993, Terziev et al 1992).

Because the information that can be deduced from hydrographic observations is limited, the construction of the missing elements of the seasonal circulation pattern depends on the detailed results obtained from numerical models. The first numerical models designed sea were performed in the middle 1970s. Later diagnostic models by Trukhchev et. al (1995) and Tuzhilkin et. al (1997) have indicated dipole structures in the Middle Caspian Sea (MCS) and the Southern Caspian Sea (SCS). A cyclonic gyre in the northwestern part and an anticyclonic gyre in the southeastern part of the MCS. A similar pattern is also predicted for the SCS, with an anticyclonic cell in the northwest,

and a cyclonic cell in the southeast. Based on above mentioned feature, Lednev (1943) have generated the schematic representation of the Caspian Sea currents as shown in Figure 2.5.

As a shallow basin, Northern Caspian surface currents are controlled by local winds. (Bondarenko 1993, Terziev et. al., 1992). Middle Caspian Sea shows cyclonic circulation with narrow flow over the western coast of the basin, while northward currents are observed along the eastern coast. The currents isolated from each other at some extent, because of the relief of the bottom.

Recently, Ibrayev (unpublished) have shown the cyclonic circulation in the MCS in winter, southward surface current and northward subsurface current along the eastern shelf. Schrum have noted the same pattern as Ibrayev in winter, by using HAMSOM model conducting interannual simulation from 1979 to 1993. However they showed that the pronounced cyclonic and topography driven circulation turns for typical summer wind conditions to an anticyclonic circulation in MCS contradict with the finding of the Ibrayev et. al.

Besides modelling efforts, the circulation characteristics of the Caspian Sea was also investigated by using satellite driven SST and chlorophyll by Sur et. al. They have revealed the sign of cold southward flow along the west coast and warm water intrudes northward from the SCS to the MCS.

The largest inflow of fresh water comes from the Volga River, accounting for about 80% of the climatological mean river discharge of $250\text{km}^3 \text{ yr}^{-1}$ (Kosarev and Yablonskaya, 1994). It is known that, buoyant coastal river discharge produces large-scale plumes and coastal currents in waters of the continental shelf and shelf seas (Garvine, 2001). Thus, the inflow from the Volga river would be expected to play a significant role in the dynamics of the region.

The lack of information about upper ocean quantities in the Caspian Sea makes it essential to study spatial and temporal variability of various variables, including direction and magnitude of currents in addition to SSH and SST over the seasonal cycle using an eddy-resolving ocean model.

The spectra of the current fluctuations and water temperatures in the deep

open sea there appear four basic period (Kosarev and Yablonskaya, 1994), the natural synoptical of five days, the quasi-inertial of 19 hours, the semi-diurnal tidal, and the nine hour seiche period (Figure 5.22). Near the coastline the energy spectrum of the currents are complicated.

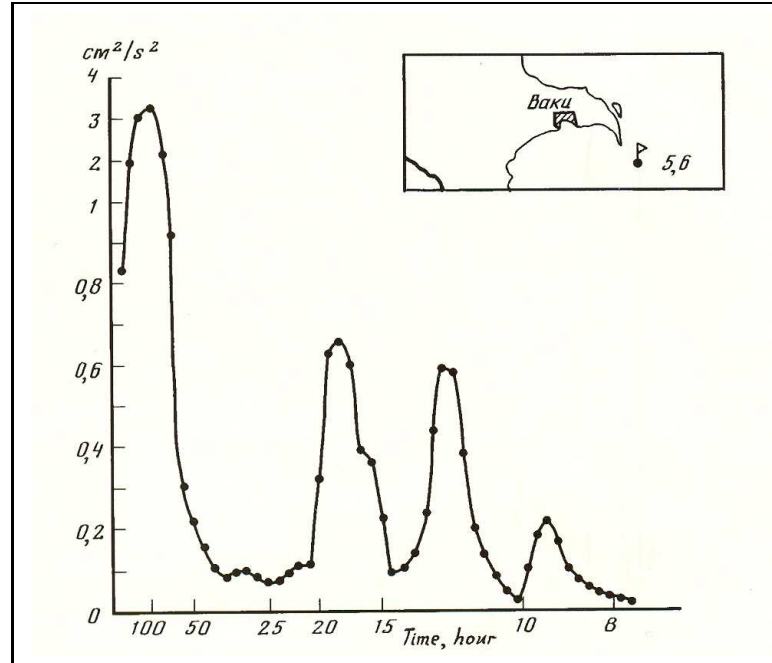


Figure 2.6: Energy spectrum of time variability for currents at levels of 200m as recorded by moored station off the Apsheron peninsula. Obtained from Kosarev and Yablonskaya, 1994

2.5 Upwelling

In summer through early fall there is continuous upwelling along the eastern coast of the Caspian Sea. This summer upwelling was studied by numerous authors (Baidin 1986, Kosarev 1975, Terziev 1992, Kosarev 1990, Sur et al., 2000). Upwelled water is easily detected by satellite SST data with relatively colder waters along the coast and filaments penetrating offshore from the up-

welling region. Figure 2.7 shows such a satellite SST image obtained from AVHRR satellite. The upwelling region extends from 41° to 44°N along the eastern coast with temperature $2 - 3^{\circ}\text{C}$ lower than the surrounding water in a region extending 5-20 km from the coast. The upwelling at the central part of the eastern coast appears more active in this image, but a review of similar data shows that the upwelling region shifts to the north or south during other times. The eastern coast upwelling is closely related with the predominant northerly winds in summer. The upwelling distribution evidently changes with the wind intensity and direction.

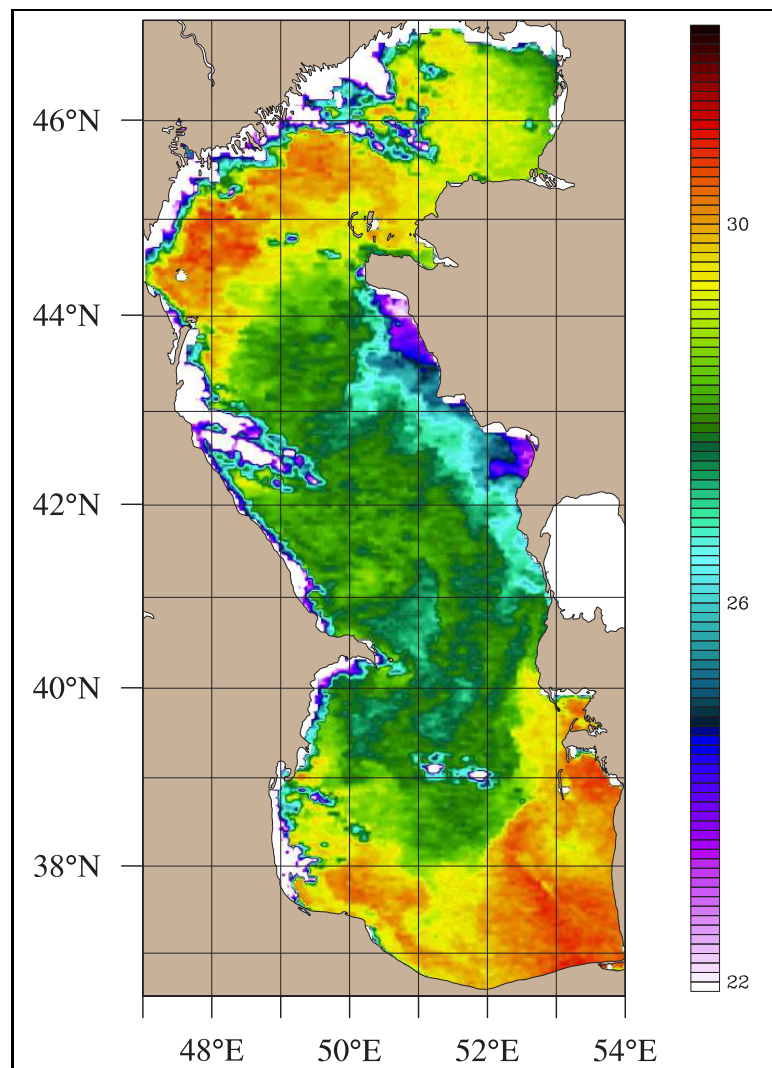


Figure 2.7: AVHRR SST ($^{\circ}\text{C}$) on 17 July 2001

Geometric / topographic irregularities along the coast such as headlands influence the upwelling, as well as the stability of the upwelling front (Peffley and O'Brien 1976).

The structure of the marine atmospheric boundary layer is often modified by gradients in sea surface temperature (Song et. al. 2006), such as those present in upwelling regions. These changes have been observed and modelled in different parts of the world ocean (Chelton et al., 2001; Chelton 2005). In the Caspian Sea, the SST gradient along the eastern coast is likely to generate similar effects and is likely to influence the exchange with the atmosphere over the sea and the adjacent desert land.

Compared to the other biologically active upwelling regions of the world ocean, plankton blooms with high chlorophyll concentration are peculiarly not evident in satellite images of the upwelling region along the eastern coast of the Caspian Sea.

An important consequence of Caspian Sea upwelling is the advection of high salinity water onto the shelf by compensation currents along the coast, creating favorable conditions (pre-conditioning) for dense water formation during the later winter period, leading to intense slope convection that can ventilate the deeper waters of the Middle Caspian Sea.

2.6 Dense Water Formation

Ventilation of the deep waters of the Caspian Sea occurs through complex processes. The rate of formation of dense water is controlled by complex factors such as the rate of cooling in the shallow continental shelf areas in the northern part of the Caspian Sea, ice formation in the North Caspian Sea, saline water ejection by ice, the background stratification and fronts, fresh water input, surface fluxes and meso-scale circulation. The fate of the sinking dense water depends on topography which also influences the circulation.

Dense water formation contributes to renewal of the deep water, and thereby

affects the circulation of the sea. The mechanism for dense water formation is not clear in the Caspian Sea. Kosarev (1985) has suggested two possible mechanisms for sinking of dense water: (1) in summer, evaporation increases the density of sea water at the surface, which then sinks deeper, especially along the eastern coast, (2) in winter, salt ejection by freezing results in a saline surface waters in the NCS. In addition, surface waters flowing northward along the eastern coast of the MCS come into contact with the ice on the northern slopes of the MCS, become denser by cooling and sink to greater depths of the MCS (Ferronsky 2003). Kosarev and Yablonskaya (1994) have also noted that the conditions for development of winter-time vertical motions are more favorable along the eastern coast compared to the other regions.

Based on two cruises performed in September 1995 and September 1996 Peeters et al. (2000) have suggested a similar mechanism for dense water formation, whereby water transported north along the eastern part of the Caspian Sea becomes colder by encountering the ice and less saline cold water in the north and sinks to the deeper parts of the Middle Caspian Sea. Climatological data show a cold water mass with high density near the eastern coast at 44°N latitude (Figure 5.29).

Based on isotope techniques, Froehlich et al. (1998) investigated the deep-water renewal process in relation to the effects of the water balance and sea-level change. They concluded from a study of tracers that the mixing in the Caspian Sea occurs in several stages: first in the MCS and later transmitted into the SCS by overflow across Apsheron sill. They also argue that, one of the possible mechanism for dense water formation (the surface water of the MCS flow northward along the eastern coast. After reaching the edge of the ice on the northern slope of the MCS, they cool down, become denser, and sink in deepwater layers of the MCS.) is consistent with the character of the linear relationship between the isotopic composition of O and the salinity in deep waters of the MCS. From their results, the average age of water in the middle and southern Caspian Sea is 22 (1995-1973) and 25 (1995-1970) years,

respectively. For samples of 1996, the age of water in the MCS and SCS was estimated by 24 and 26 years, respectively. Therefore, they concluded that the rate of the vertical mixing of seawater slowed down between 1995 and 1996, suggesting that the amount of river waters entering the sea diminished.

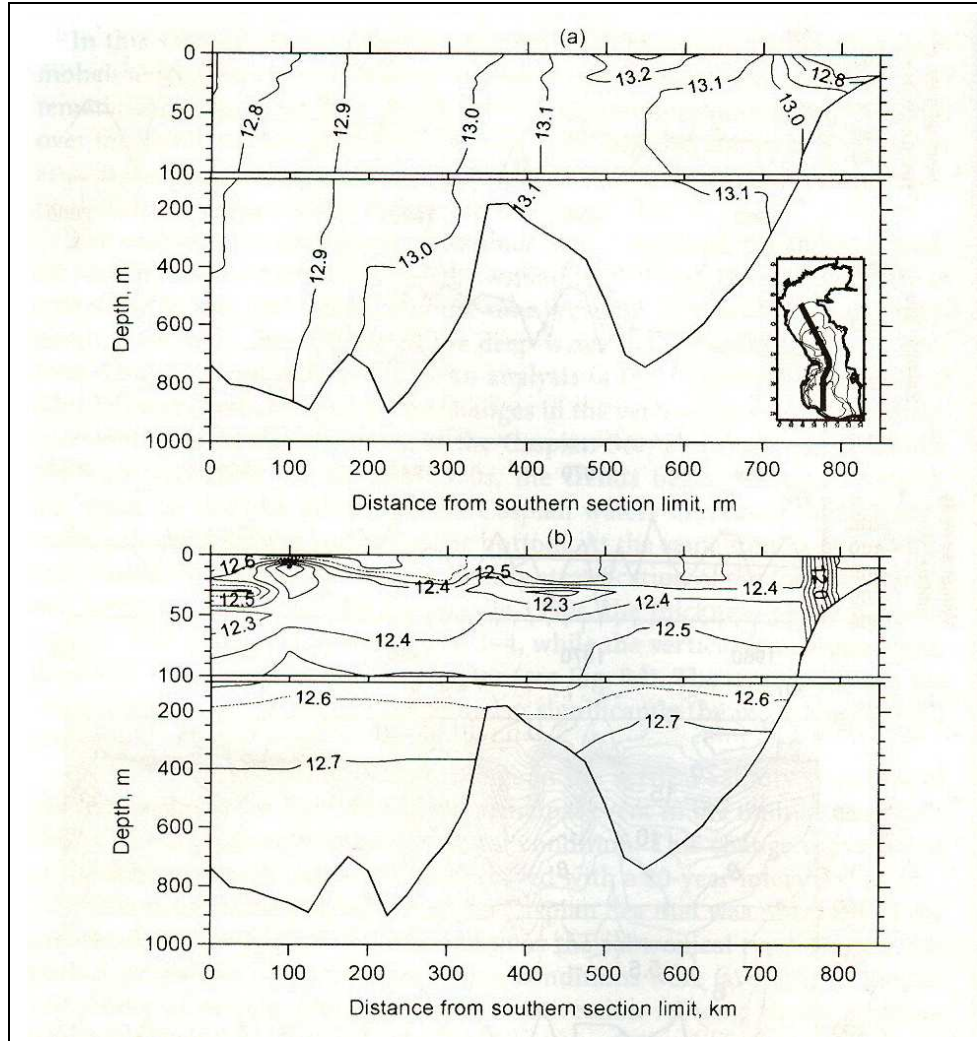


Figure 2.8: Cross section (see inset for the location of the section) of salinity (psu) in the Caspian Sea (a) August 1976 and (b) September 1995. From Kostianoy and Kosarev 2005.

Ventilation of deep waters is sensitive to changes in sea level (Kosarev

1975, Terziev 1992, Ferronsky 2003, Peeters 2000). Deep-water renewal in the Caspian Sea appears to be an intermittent process with extreme large-scale convective mixing events taking place on an interannual basis. It is often argued that the rise and fall of the Caspian Sea level associated with varying degrees of fresh water influence changes the stratification and thereby affects the thermohaline circulation and the mixing processes of the Caspian Sea (Kosarev and Yablonskaya 1994, Ferronsky 2003).

The dramatic effect of sea level change on the mixing properties of the Caspian Sea can be easily seen in the Figure 2.8. In this figure cross section (see inset for the location of the section in the figure) of the Salinity was shown for two years. While upper figure shows the condition when sea level is lowest, the lower figure shows the condition when sea level is higher. In the upper figure, the entire water column of two basins of the sea is mixed evident from the constant vertical salinity contours from surface to the bottom of the sea. However, during the higher sea level conditions, the stratification is evident at 100 m depth.

By using the isotopic composition of water masses Peeters et al. (2000) and Ferronsky et al. (2003) have also investigated the water-exchange processes in this basin. They have concluded that the decrease in sea level could have caused a major mixing event in 1976. It is reasonable that after that time no major mixing has occurred, because the sea level rise leads to a decrease in surface-water salinity and thus reduces the probability of large-scale convective mixing.

CHAPTER 3

THE DATA AND MODEL

3.1 The Data

The following data have been collected and analyzed in the present thesis, in order to interpret and compare the model results:

3.1.1 Sea Surface Temperature

The Advanced Very High Resolution Radiometer (AVHRR) Ocean Pathfinder global equal-angle SST data set (Version 5.0) has been obtained from the U.S. National Oceanographic Data Center (NODC) public web site (<http://www.nodc.noaa.gov/SatelliteData/pathfinder4km/>). This 4 km AVHRR Pathfinder data set is based on a new reanalysis of the AVHRR data stream, developed jointly by the Rosenstiel School of Marine and Atmospheric Science, University of Miami (RSMAS) and the NODC. An improved version of the Pathfinder algorithm and its processing steps have been used to produce twice-daily global SST and related parameters since 1985, at a resolution of approximately 4 km, the highest possible for a global AVHRR data set. Improvements in the data, relative to the original 9 km Pathfinder SST data set, include a more accurate, consistent land mask, higher spatial resolution, and the consideration of sea ice information.

Monthly SST is calculated by averaging daily SST data, and the SST

anomaly is calculated by subtracting the climatological SST from these monthly values. Because we are interested in establishing relationships with climate patterns, and in particular with the North Sea - Caspian Pattern (NCP), the SST data were then windowed to include data between February and May of each year, representing mid-winter to mid-spring months shown by earlier studies (Ghasemi and Khalili 2007, Tatli 2007) to be most relevant for the effects of NCP on the climate of the region.

The NCP index was calculated following Kutiel and Benaroch (2002), with the time range of the index extended to 2006. For this purpose, the NOAA/NCEP-NCAR monthly intrinsic geopotential height at 500 hPa was averaged over the two rectangular center regions defined by Kutiel and Benaroch (2002): in the North Sea between $0^{\circ}E$, $55^{\circ}N$ and $10^{\circ}E$, $55^{\circ}N$, and in the North Caspian Sea between $50^{\circ}E$, $45^{\circ}N$ and $60^{\circ}E$, $45^{\circ}N$, selected on the basis of linear correlation analysis by the same authors

3.1.2 MODIS chlorophyll concentration

The 1 km resolution MODIS chlorophyll data, retrieved by instruments on board the Aqua polar orbiting environmental satellite, are provided by the NASA OceanColor project at <http://oceancolor.gsfc.nasa.gov/>. Level 2 MODIS data, available since from June 2002 till the present time were obtained and processed by the SeaDAS (SeaWiFS Data Analysis System, version 4.9.4) software, with the data windowed in the $36.5^{\circ}N$ to $46.5^{\circ}N$ and $47.5^{\circ}E$ to $55^{\circ}E$ region. With Mercator projection, the the data array for each image has a size of 710 x 1224.

3.1.3 Sea Level Anomaly

The Sea Level Anomaly (SLA) data covering the Caspian Sea were obtained from A. Kostianoy, following the work of Kostianoy and Lebedev (2006). The TOPEX/Poseidon (T/P) and Jason-1 (J1) satellites were used to construct the Caspian Sea SLA. The positions of the T/P and J1 ground tracks are optimal

for the analysis of sea level variations in the Caspian Sea. The orbital repeat period (10 days) enables the analysis of interannual and seasonal variability of sea level. These data represent the longest time-series of satellite altimetric measurements (from September 1992 to August 2002, cycles 1 to 365 for T/P, which is extended from August 2002 till the present time by the J1 along the same tracks).

Kostianoy and Lebedev (2006) have analyzed 13 years of T/P and 3.5 years of J1 data for the September 1992 to December 2005 period, obtained from the NASA Goddard Space Flight Center (GSFC) Ocean Altimeter Pathfinder Project (Koblinsky et al., 1999).

The climatological monthly means of the data were calculated from the time-series data available for the above period, and compared with model results to evaluate model performance.

3.1.4 Drifters

Three SVP-BT Lagrangian drifters were deployed in the Caspian Sea. (the Technical Specification for the drifters is accessible on Marin-Yug site - <http://marlin.stel.sebastopol.ua/>). The drifters transmit the sea surface temperature, air pressure and subsurface temperature at the 12 m depth in every 60 minutes. The longitude and latitude of the location of the drifters transmitted in randomly time intervals. The data is low-pass filtered with one hour period before calculating the drifter currents.

3.2 Model Characteristics and Setup

3.2.1 The HYbrid Coordinate Ocean Model (HYCOM)

The model is a generalized (hybrid, isopycnal / terrain-following σ / z -level) coordinate primitive equation model whose original features are described by Bleck (2002). The hybrid coordinate extends the geographic range of appli-

cability of traditional isopycnal coordinate circulation models toward shallow coastal seas and unstratified parts of the ocean.

The original hybrid coordinate approach was accomplished using a hybrid vertical coordinate grid generator (Bleck 2002). Any remapper of this kind must be based on a full vertical profile that is consistent with the model fields (which represent vertical averages across each layer). The original remapper in HYCOM assumed that each field was constant in the vertical within each layer. This is the simplest possible profile, and it may be the best choice when remapping layers that are nearly isopycnal. However, when remapping layers that are far from isopycnal this approach can lead to excessive diffusion. HYCOM’s current remapper, as used in the Caspian Sea simulations presented in this thesis, allows the profile to vary linearly across a layer if the layer is not close to being isopycnal, which significantly reduces diffusion. The remapping process can be thought of as finite volume vertical advection (Leveque 2002). In terms of the finite volume methodology, the original remapper corresponds to donor–cell upwind advection, while the remapper used in this study is based on the piecewise linear method with a monotonized central–difference limiter (van Leer 1977).

The model contains a total of five prognostic equations: two momentum equations for the horizontal velocity components, a mass continuity or layer thickness tendency equation and two conservation equations for a pair of thermodynamic variables, such as salt and temperature or salt and density. The model equations, written in (x, y, s) coordinates, where s is an unspecified vertical coordinate, are

$$\frac{\partial \mathbf{v}}{\partial t_s} + \nabla_s \frac{\mathbf{v}^2}{2} + (\zeta + f) \mathbf{k} \times \mathbf{v} + \left(\frac{\partial s}{\partial t} \frac{\partial p}{\partial s} \right) \frac{\partial \mathbf{v}}{\partial p} + \nabla_s M - p \nabla_s \alpha = -g \frac{\partial \tau}{\partial p} + \left(\frac{\partial p}{\partial s} \right)^{-1} \nabla_s \cdot \left(\nu \frac{\partial p}{\partial s} \nabla_s \mathbf{v} \right), \quad (3.1)$$

$$\frac{\partial}{\partial t_s} \left(\frac{\partial p}{\partial s} \right) + \nabla_s \cdot \left(\mathbf{v} \frac{\partial p}{\partial s} \right) + \frac{\partial}{\partial s} \left(\frac{\partial s}{\partial t} \frac{\partial p}{\partial s} \right) = 0, \quad (3.2)$$

$$\frac{\partial}{\partial t_s} \left(\frac{\partial p}{\partial s} \theta \right) + \nabla_s \cdot \left(\mathbf{v} \frac{\partial p}{\partial s} \theta \right) + \frac{\partial}{\partial s} \left(\frac{\partial s}{\partial t} \frac{\partial p}{\partial s} \theta \right) = \nabla_s \cdot \left(\nu \frac{\partial p}{\partial s} \nabla_s \theta \right) + \bar{h}_\theta, \quad (3.3)$$

where $\mathbf{v} = (u, v)$ is the horizontal velocity vector, p is pressure, θ represents any one of the model's thermodynamic variables, $\alpha = 1/\rho$ is the potential specific volume, $\zeta = \partial v/\partial x_s - \partial u/\partial y_s$ is the relative vorticity, $M = gz + p\alpha$ is the Montgomery potential, $gz = \phi$ is the geopotential, f is the Coriolis parameter, \mathbf{k} is the vertical unit vector, ν is a variable eddy viscosity/diffusivity coefficient, and τ is the wind- and/or bottom-drag induced shear stress vector. The variable \bar{h}_θ represents the sum of diabatic source terms, including diapycnal mixing acting on θ . Subscripts show which variable is held constant during partial differentiation. Distances in x, y direction, as well as their time derivatives u and v , respectively, are measured in the projection onto a horizontal plane.

The prognostic equations in the model are time-integrated using a split-explicit treatment of barotropic and baroclinic modes (Bleck and Smith 1990). The split-explicit approach has proven to be advantageous for executing ocean models on massively parallel computers because it does not require solution of an elliptic equation. Isopycnal diffusivity and viscosity values, including the one used for thickness diffusion (interface smoothing), are formulated as $u_d \Delta x$ where Δx is the local horizontal mesh size and u_d is of order 0.01 m s^{-1} . In regions of large shear, isopycnic viscosity is set proportional to the product of mesh-size squared and total deformation (Smagorinsky 1963), the proportionality factor being 0.2.

HYCOM uses the K-Profile Parameterization (KPP) mixed layer model (Large et al. 1994), which is particularly attractive for several reasons. It contains improved parameterizations of physical processes in the mixed layer, including non-local effects. It has also been designed to run with relatively low vertical resolution, an advantage for OGCMs. The KPP model calculates the mixing profile from the surface to the bottom of the water column, and

thus provides an estimate of diapycnal mixing beneath the mixed layer. It provides mixing throughout the water column with an abrupt but smooth transition between the vigorous mixing within the surface boundary layer and the relatively weak diapycnal mixing in the ocean interior. The KPP scheme has primarily been tuned against Large Eddy Simulations (LES) and therefore typically over short time scales (e.g. the diurnal cycle) and in small regions.

3.2.2 Caspian Sea Model

Model Resolution and Constants

The Caspian Sea model used here has a resolution of $1/25^\circ \times 1/25^\circ$, on a Mercator grid. Zonal and meridional array sizes in the model are 204 and 354, respectively. The Mercator grid has square grid cells with a resolution of $(0.04 \times \cos(\text{lat}) \times 111.2 \text{ km})$, i.e., 4.44 km in the meridional direction and 3.37 km at the southern and 3.05 km at the northern ends of the domain in the zonal direction. Average zonal grid resolution is $\approx 3.2 \text{ km}$.

The model has 30 hybrid layers (14 sigma levels – and 16 z -levels). A detailed explanation is provided here on the distribution of the vertical layers in the Caspian Sea model. One advantage of HYCOM is the generalized vertical coordinate. Typically, the model has isopycnal coordinates in the stratified ocean but uses the layered continuity equation to make a dynamically smooth transition to z -levels (fixed-depth coordinates) in the unstratified surface mixed layer and σ -levels (terrain-following coordinates) in shallow water. The optimal coordinate is chosen every time step using a hybrid coordinate generator. Thus, HYCOM automatically generates the lighter isopycnal layers needed for the pycnocline during summer. These become z -levels during winter. The density difference values were chosen so that the layers tend to become thicker with increasing depth, with the lowermost abyssal layer being the thickest.

In general, HYCOM needs fewer vertical coordinate surfaces than, say, a conventional z -level model, because isopycnals are more efficient in represent-

ing the stratified ocean. For example, fewer isopycnals than z -levels are needed to resolve the pycnocline because (1) the isopycnals are Lagrangian coordinates that follow the simulated depth of the chosen isopycnals with computational precision, and (2) isopycnal coordinates avoid the artificially large diapycnal diffusion that occurs in z -level and σ -coordinate models. This allows isopycnal models to maintain a sharp pycnocline without the diffusion that plagues z -level and σ -coordinate models. In contrast, z -level models must resolve the pycnocline by having high vertical resolution at all depths where the pycnocline may occur. The high vertical resolution is also needed to allow lower vertical diffusion coefficients below the mixed layer and thereby decrease the pycnocline diffusion. More z -levels than isopycnals are also needed to resolve the bottom topography, which is represented by the bottom layer thickness in isopycnal models. In the unstratified mixed layer HYCOM uses z -levels (in deep water) and needs the same high vertical resolution as a z -level model.

Constant parameters used in the Caspian Sea model are provided in Table 3.1.

Bottom topography

The bottom topography in the Caspian Sea model (Figure 3.1) was constructed from Russian bathymetry data with a resolution of $1/120^\circ$ (GLOBE project. www.globe.gov). After interpolation to the Caspian Sea model grid, the final topography was smoothed twice with a 9-point smoother to reduce topographic vorticity generation at small scales poorly resolved by the model grid. The Caspian Sea has a flat wide shelf in the northern part as well as its southeastern extremity, and a steep continental slope along the western and southern coasts and a wide shelf with a gentle slope in eastern part of Middle Caspian Sea. A mild continental slope also occurs at the transition between the northern shelf and the middle basin. The middle and southern basin depressions reach maximum depths of 800 and 1000 m respectively. The two deep basins are separated by the Apsheron peninsula and its extension

Table 3.1: Constant parameter values used in the HYCOM Caspian Sea simulations. In the ocean interior, the contribution of background internal wave breaking, shear instability mixing, and double diffusion (both salt fingering and diffusive instability) are parameterized by the KPP model. In the surface boundary layer, the influence of wind-driven mixing, surface buoyancy fluxes, and convective instability are parameterized. The KPP algorithm parameterizes the influence of nonlocal mixing of temperature and salinity, which permits the development of countergradient fluxes.

Value	Description of the constant used in the Caspian Sea model
0.1	Deformation-dependent Laplacian viscosity factor
0.005	Diffusion velocity (m/s) for Laplacian momentum dissipation
0.0067	Diffusion velocity (m/s) for biharmonic momentum dissipation
0.005	diffusion velocity (m/s) for Laplacian temp/saln diffus.
2.2×10^{-3}	Coefficient of quadratic bottom friction
10.0	Thickness of bottom boundary layer (m)
0.02	Minimum density jump across interfaces (kg/m^3)
0.2	Equivalent temperature jump across mixed-layer (degC)
30.0	Reference mixed-layer thickness for SSS relaxation (m)
0.45	KPP: critical bulk richardson number (Ri)
50×10^{-4}	KPP: max viscosity due to shear instability (m^2/s)
50×10^{-4}	KPP: max diffusivity due to shear instability (m^2/s)
1.0×10^{-4}	KPP: background/internal wave viscosity (m^2/s)
1.0×10^{-5}	KPP: background/internal wave diffusivity (m^2/s)
10.0×10^{-4}	KPP: salt fingering diffusivity factor (m^2/s)
1.9	KPP: salt fingering $rp=(\alpha*\Delta T)/(\beta*\Delta S) \rho_{olacak}$
98.96	KPP: value for nonlocal flux term
10.0	KPP: value for nonlocal flux adjustment term
5.0	KPP: value for the turbulent velocity scale

forming the Apsheron sill with a depth of about 150 m and width of about 70 km at its crest (see Figure 3.1).

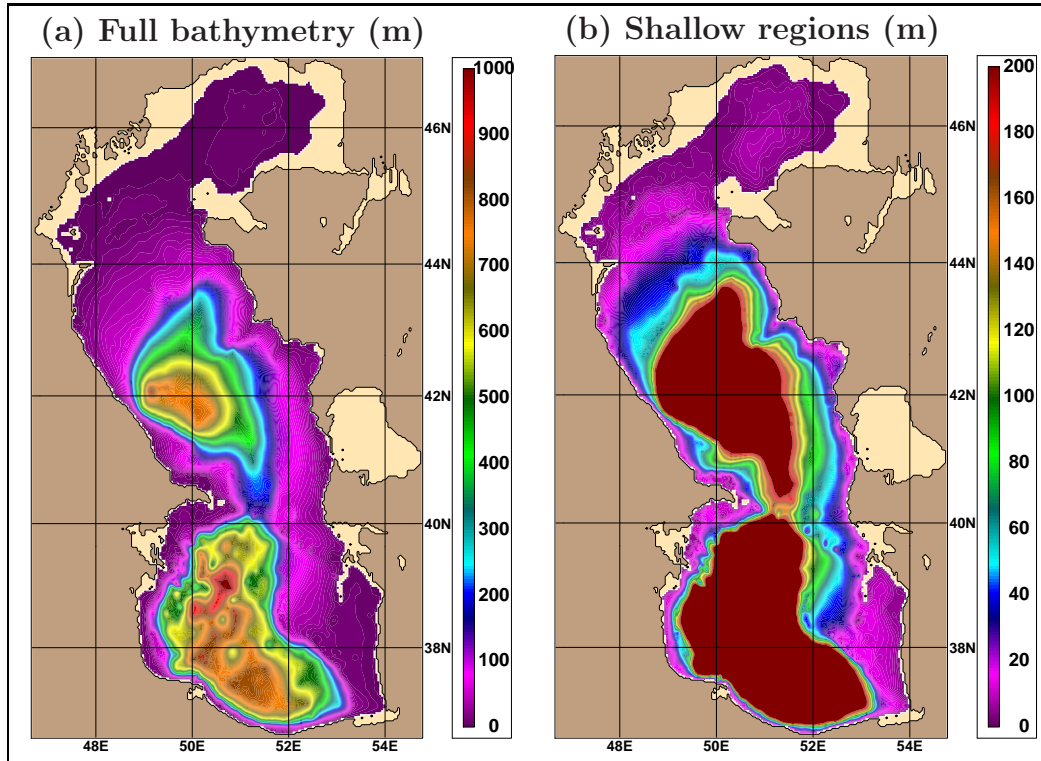


Figure 3.1: The Caspian Sea bathymetry (m) and the model coastline used in the HYCOM simulations. The model land-sea boundary is the 4 m isobath which is shown with light brown in color. The Kara Bogaz Gol is excluded in the model simulations

Temperature and Salinity Initialization

The Caspian Sea simulations suffer from lack of good quality, fine-resolution subsurface temperature and salinity climatologies to be used for model initialization. Although, the $1^\circ \times 1^\circ$ World Ocean Atlas 2005, the well-documented and commonly used subsurface temperature and salinity climatology of Johnson (2006), covers the Caspian Sea region, only 5 standard levels have been des-

ignated in WOA05 for the much of the Caspian Sea. It is therefore not possible to use this data until correcting the bathymetry used in WOAS05 climatology calculation. It was therefore preferred to initialize HYCOM with temperature and salinity data from the Russian climatological data set (Kosarev and Tuzhilkin, 1995). This climatological data set has $0.25^\circ \times 0.2^\circ$ horizontal grid resolution, and insufficient data in the deeper layers. The model was initialized by interpolating the climatology data to the model grid points.

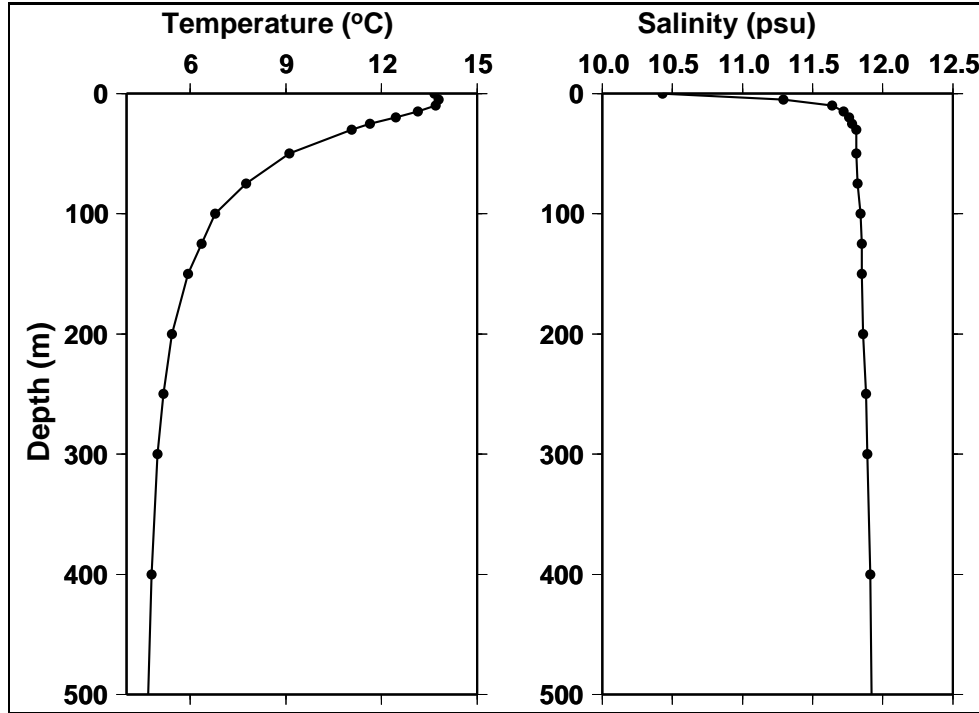


Figure 3.2: Annual mean of basin averaged climatological monthly mean temperature and salinity profiles obtained from Russian data set.

The annual and basin average potential temperature and salinity fields from this data calculated at 19 depth levels ranging from 0 to 800 m are shown in (Figure 3.2). Annual and basin mean surface temperature is warmer, the deeper part of the Sea shows little temperature variation, and has approximately $5^\circ C$. A relatively fresh surface layer of less than 30 m is observed in the salinity

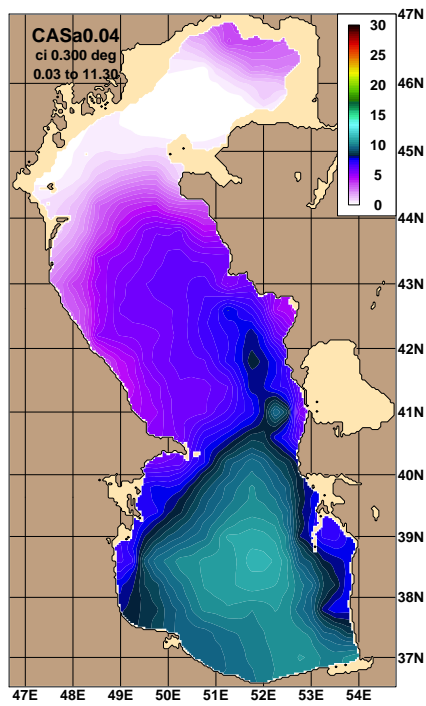
profile, salinity increases from 10.43 psu at the sea surface to 11.95 psu at 800 m. There is a very shallow halocline with a depth of 30-40 m. The deep layer below 200 m are nearly homogeneous.

Colder Sea Surface Temperature along the either side of the Sea is evident from the data obtained from hydrographic observations shown in Figure 3.3 in February. During July, due to the upwelling along the eastern coast of the Caspian Sea, colder temperatures present only along the eastern coast of the MCS. The detailed description of the SST was made in Chapter 2 of this thesis.

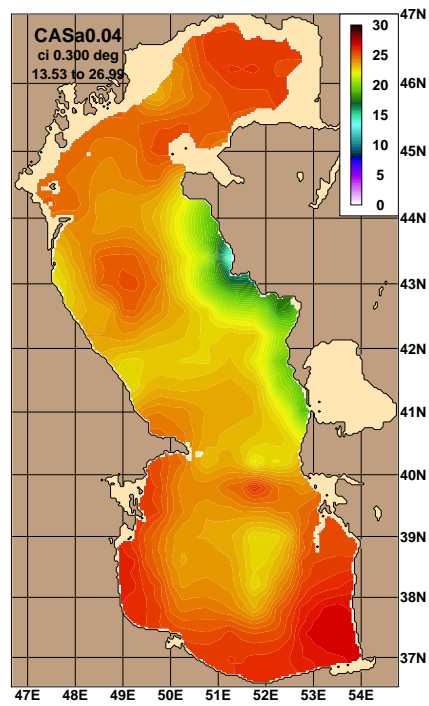
Sea Surface Salinity (SSS) in the Caspian Sea shows strong seasonal and interannual fluctuations. Figure 3.4 shows the climatological SSS based on the hydrographic observations in February and July months. There is marked zonal gradients of salinity in the sea, the lowest salinity is observed in Northern Caspian Sea as result of the Volga river input. Because there are no permanent rivers or other runoff on the eastern coast of the Caspian Sea and because the evaporation is also higher there, the salinity in the eastern part is relatively higher than the west which is easily observed in the Figure 3.4 for February and July months as east/west gradient in salinity. South Caspian Sea also has high rate of evaporation. Waters of the eastern continental shelf of the SCS are more saline due to the high evaporation in that shallow region during the whole year period.

There is continuous stratification in the South Caspian Sea, including the winter months. The stratification in MCS is very strong in summer and weaker in winter due to mixing. Figure 3.5 shows the climatological temperature and salinity section along the $50^{\circ}E$. The data is interpolated to the model grid. The stratification in temperature is obvious in the upper figure. Deeper waters of the MCS has lower temperature compared to the SCS. While the temperature is about $5^{\circ}C$ below the 400 m in the MCS, it is about $7^{\circ}C$ in the SCS. The quality of the salinity data is not clear, but in general lower salinities are observed in the upper and western part of the Sea as shown lower panel of the Figure 3.5.

The mixed layer in the Middle Caspian Sea may reach to depths of 200 m

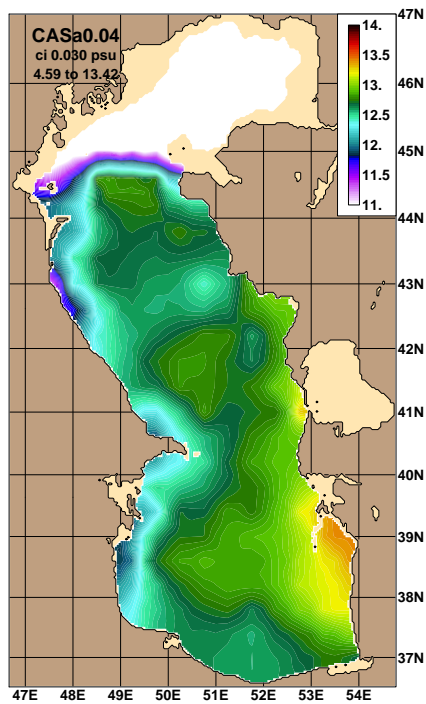


(a) February

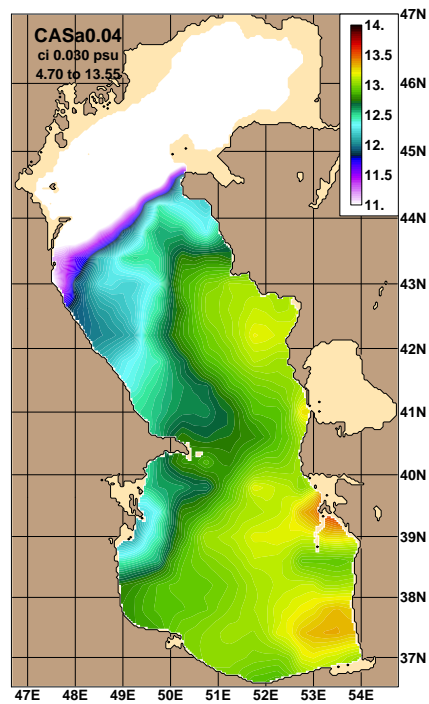


(b) July

Figure 3.3: Climatological SST $^{\circ}\text{C}$ based on hydrographic observations in February and July



(a) February



(b) July

Figure 3.4: Climatological SSS (psu) based on hydrographic observations in February and July

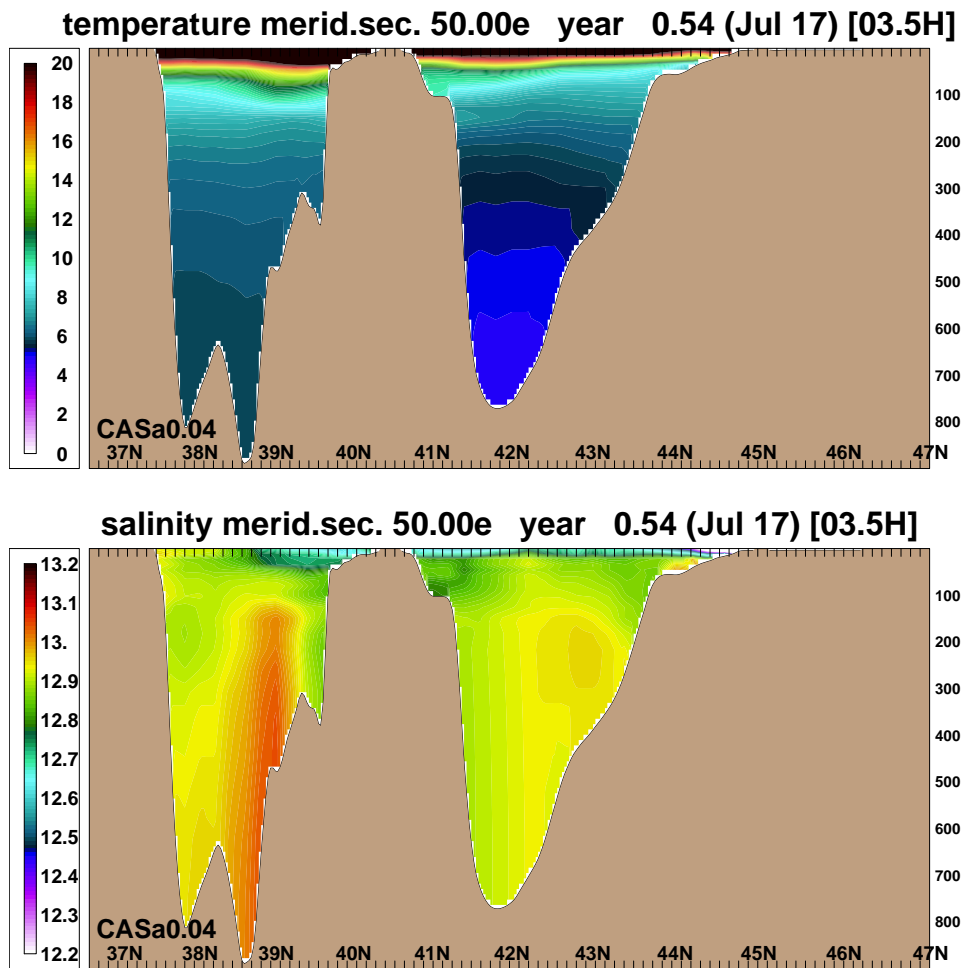


Figure 3.5: Climatological upper: temperature °C, lower: salinity (psu) section based on the hydrographic observations along the 50°E in July.

and deeper in winter months as a result of cooling and convection processes.

Wind and Thermal Forcing

The HYCOM model uses the following time-varying atmospheric forcing fields to impose surface flux boundary conditions: wind stress and thermal forcing (air temperature and mixing ratio at 10 m above the sea surface, net shortwave and net longwave radiation at the sea surface).

For the Caspian Sea model wind/thermal forcing was constructed from 1.125° × 1.125° ECMWF Re-Analysis (ERA) 40 climatology

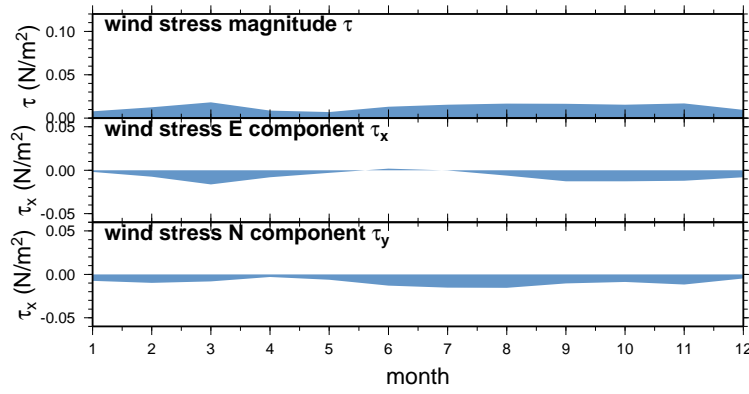


Figure 3.6: Climatological momentum fluxes averaged over the Caspian Sea from ERA-40 Re-Analysis

All model simulations are performed using climatological monthly mean forcing fields. However, a high frequency component is added to the climatological forcing because the mixed layer is sensitive to variations in surface forcings on time scales of a day or less (e.g., Wallcraft et al. 2003; Kara et al. 2003) and because the future goal is to perform simulations forced by high frequency interannual atmospheric fields from operational weather centers. Hybrid wind stress fields are obtained by complementing monthly ECMWF wind stress with ECMWF wind stress anomalies, as briefly described in the following: 6-hourly intra-monthly anomalies from ECMWF are superposed on the climatological monthly mean wind stress interpolated at 6-hourly intervals. The 6-hourly anomalies are obtained from a reference year, selecting the year of September 1994 through September 1995, to are used, represent a typical annual cycle of the ECMWF winds. The wind stresses are then calculated from the 10 m winds using the bulk formulae of Kara et al. (2002).

3.2.2 shows climatological monthly wind stress and wind stress curl fields over the Caspian Sea, obtained from ERA40-Reanalysis data set interpolated to the model grid. The typical wind stress magnitude is 0.02-0.04 N/m^2 . In winter, northeasterly winds are dominant over the Middle and South Caspian Sea. In summer, northerly winds are observed over the whole sea. In the

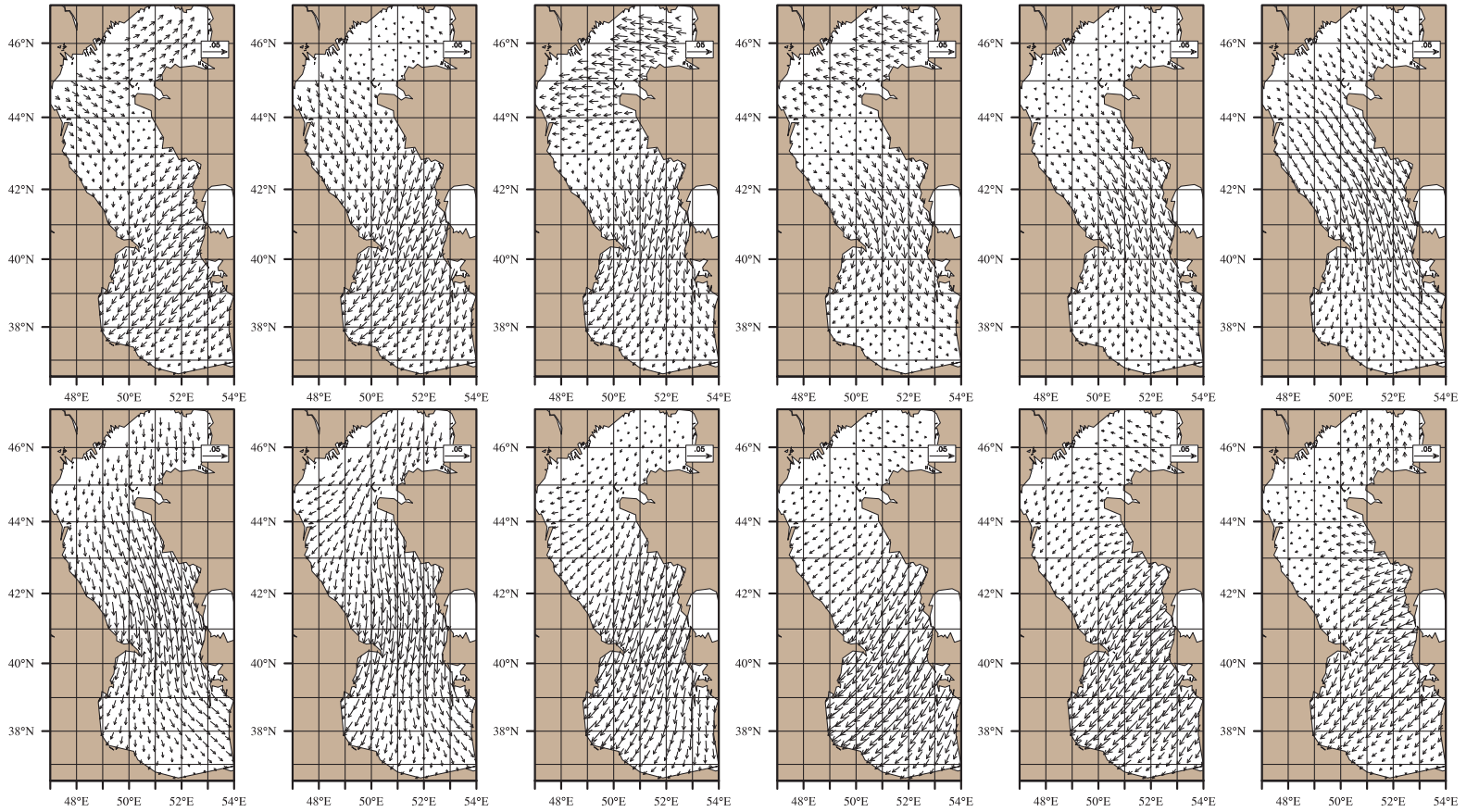


Figure 3.7: Climatological monthly mean wind stress fields (N/m²) over the Caspian Sea from January through December calculated by using ERA-40 Re-Analysis data set and interpolated to the model grid.

Northern Caspian Sea, wind direction is very unstable, changing direction northward in winter to southward in summer.

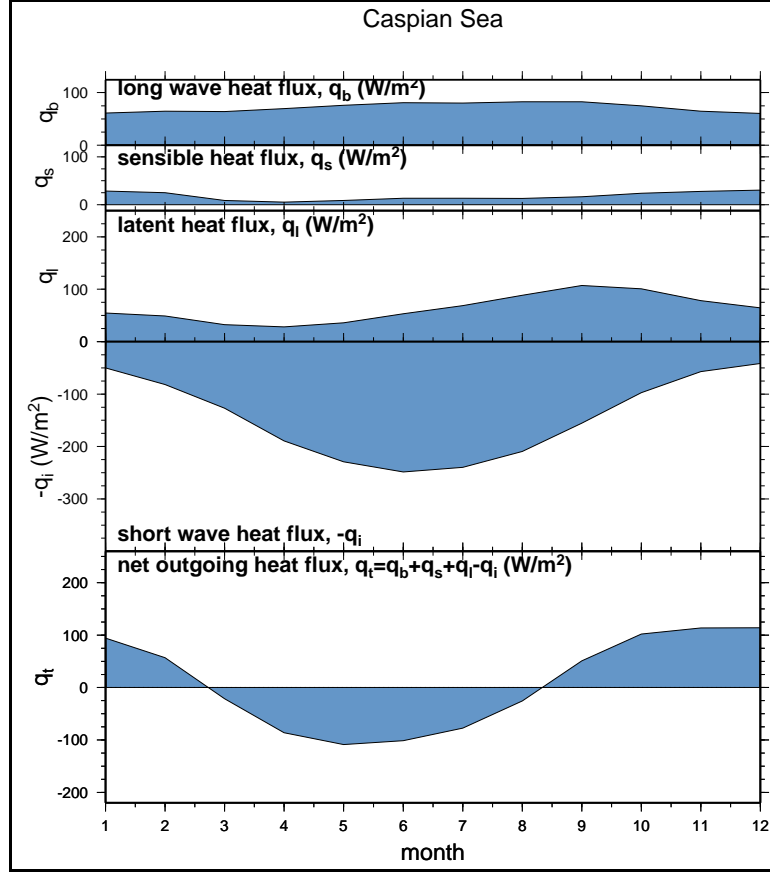


Figure 3.8: Climatological monthly mean surface heat fluxes averaged over the Caspian Sea from ERA-40 Re-Analysis

The net heat flux absorbed by the near-surface waters $Q(z)$, at any depth z , is parameterized by

$$Q_{sol}(z)/Q_{sol}(0) = (1 - \gamma) \exp(-z/0.5) + \gamma \exp(-zk_{PAR}),$$

$$\gamma = \max(0.27, 0.695 - 5.7k_{PAR}),$$

$$Q(z) = Q(0) + [Q_{sol}(0) - Q_{sol}(z)],$$

$$Q(0) = Q_{LW} + Q_L + Q_S,$$

where $Q(0)$ is net heat flux absorbed at the surface, Q_{LW} is the downward net longwave radiation, Q_L is the latent heat flux, and Q_S is the sensible heat flux, in which heat fluxes into the ocean are denoted to be positive. Latent and sensible heat fluxes at the air–sea interface are calculated using bulk formulae that include the effects of dynamic stability (Kara et al., 2002). Both sensible and latent heat fluxes are calculated using model top layer temperature at each model time step. Including air temperature and model SST in the formulations for latent and sensible heat flux automatically provides a physically realistic tendency towards the correct SST. Cloudiness, used in the calculation of radiation fluxes (net shortwave and net longwave fluxes) is provided directly by the ECMWF data.

The wind stress components and magnitude are calculated as follows:

$$\tau_x = \rho_a C_D u (u^2 + v^2)^{1/2}$$

$$\tau_y = \rho_a C_D v (u^2 + v^2)^{1/2}$$

$$\tau = \rho_a C_D (u^2 + v^2)$$

Here density of the air (ρ_a) at the air sea interface is calculated using the ideal gas law formulation ($\rho_a = 100P_a/R_{gas}(T_a + 273.16)$ in kgm^{-3})

Figure 3.8 shows the basin averaged seasonal cycle of the heat flux component. Among the heat flux components for the Caspian Sea the contribution of sensible heat flux to the total heat flux is the smallest, it has a broad minimum from March to September. The latent flux contribution is relatively higher at it has maximum value at September. The seasonal fluctuations of the long-wave radiation heat flux are small. Latent heat flux is maximum in August and minimum in April. As shown in the last panel of the Figure 3.8, total heat flux is negative from March to August (i.e., the ocean waters gain heat from the atmosphere).

Precipitation and Evaporation

Orographic capture of the eastward propagating mid-latitude cyclones generated in the North Atlantic Ocean and eastern Mediterranean are the main source of the precipitation for the Caspian Sea.

3.2.2 shows the climatological monthly precipitation pattern based on the ECMWF data. Precipitation over the Caspian Sea is extremely non-uniform. Maximum precipitation occurs in the southern part of the Sea, associated with mountain effects occurring at the Zagros Mountains. There is increased precipitation north of the Apsheron peninsula. Summer rainfall is very small.

In the Caspian Sea extensive evaporation occurs along east coast of the sea and NCS. There is east-west gradient of evaporation. Evaporation is strongly seasonal: it is low in winter and high in summer, reaching its maximum in September.

River Discharges

The Caspian Sea model treats rivers as a “runoff” addition to the surface precipitation field. The flow is first applied to a single ocean grid point and smoothed over surrounding ocean grid points, yielding a contribution to precipitation in m s^{-1} . This works independently of any other surface salinity forcing. Looking more closely at the largest rivers in a given ocean model domain is important to represent evaporation and precipitation effects properly.

HYCOM reads in monthly mean river discharge values. The monthly mean RivDIS climatology (Vörösmarty et al. 1997; 1998) is preferred for use in HYCOM because it gives river inflow values at the mouth of the river (Table Table 3.2). A total of three major rivers (Volga, Ural, Kura) that bring large amount of freshwater to the Caspian Sea are used as precipitation forcing. The Volga River has the largest discharge with a river flow of $6,365.0 \text{ m}^3 \text{ s}^{-1}$. The peak outflows from these rivers occur from April to July. During November to December the outflow is minimum. In the simulations described here HYCOM does not include the direct Kara-Bogaz Gol outflow.

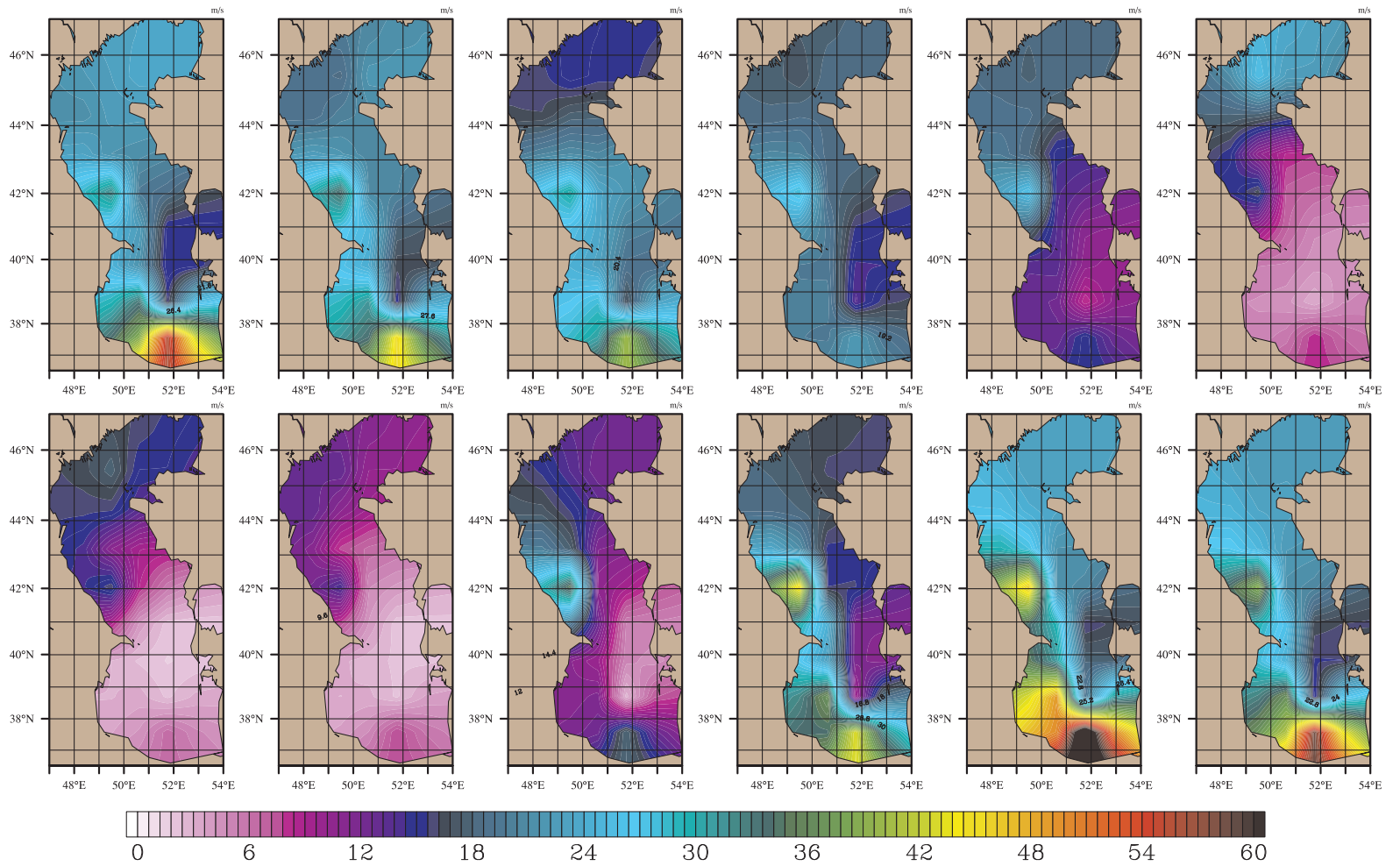


Figure 3.9: Climatological monthly mean precipitation (m/s) fields over the Caspian Sea from January through December calculated by using ERA-40 Re-Analysis data set and interpolated to the model grid.

Table 3.2: Climatological mean flow values obtained from RivDIS (see online at <http://daac.ornl.gov/rivdis/>), for the river discharge into the Caspian Sea.

	Volga (m^3/s)	Kura (m^3/s)	Ural (m^3/s)
Jan	3917.5	467.9	60.9
Feb	3960.2	493.9	56.0
Mar	4032.8	553.0	70.1
Apr	7488.5	813.3	899.5
May	24021.5	1067.2	1377.3
Jun	20075.3	850.8	409.7
Jul	8163.6	451.7	198.5
Aug	5590.6	313.7	131.9
Sep	5036.9	326.7	105.3
Oct	5358.7	387.9	98.4
Nov	5450.0	423.8	90.8
Dec	3948.0	461.0	63.4

Model Simulations

All of the HYCOM simulations presented in this thesis were performed with no assimilation of any oceanic data except initialization from climatology and relaxation to sea surface salinity. The model was run until it reached statistical equilibrium using 6-hourly climatological forcing (hybrid wind for wind stress and interpolated fields for other air-sea surface fluxes) as described earlier. It takes about 8 model years for a simulation to reach equilibrium and nearly annual cycle. After model reached a statistical equilibrium model exhibits no temporal drift.

The simulations were performed using several parallel supercomputers. The model array size is 204x354 and performing a 1-month simulation takes 1-1.5 wall-clock hours using 64 Intel processors. Most of the model run were performed by using the supercomputers of National Center for High Performance Computing Center, Istanbul Technical University (ITU). Detailed in-

Table 3.3: HYCOM simulations performed in this thesis to test the influence of wind stress and river input on circulation pattern and buoyancy fluxes on the surface properties of the sea. The model uses climatological wind and thermal forcing (i.e, air temperature at 10 m, air mixing ratio at 10 m, shortwave and longwave radiation) constructed from European Centre for Medium Range Weather Forecasts (ECMWF) re-analysis product.

Expt.	Description of the experiment
expt 1	30 layer NCOM like HYCOM, sigma-z, KPP, variable kapref, ERA40-sea winds, thermal and precip forcing, initialize from January Russian climatology and No SSS relaxation
expt 2	twin of expt 1 but NO thermal flux and barotropic ocean
expt 3	twin of expt 1 but NO thermal flux and baroclinic ocean
expt 4	twin of expt 1 but no river runoff
expt 5	twin of expt 1 but no river runoff
expt 6	twin of expt 1 but no E-P
expt 7	twin of expt 1 but no river runoff and E-P
expt 8	twin of expt 1 but output data is stored 3 hour interval
expt 9	float experiment

formation about the resources of this center can be found below web page <http://www.uybhm.itu.edu.tr/>. 64 Intel processors were used provided by this center to perform model runs.

3.3 Float Package

HYCOM has been equipped with code designed to deploy and track synthetic floats and drifters, or to seed the model with synthetic moorings, during model run time.

The horizontal and temporal interpolation schemes used to advect the floats

were adapted from the algorithms developed for MICOM (Garraffo et al, 2001a; 2001b). Horizontal interpolation is performed using a sixteen-point grid box surrounding the float. Two-dimensional polynomial interpolation is performed if a sufficient number of good grid points are available, while bilinear interpolation from the four grid points surrounding the float is performed otherwise. Temporal interpolation is performed using a fourth-order Runge-Kutta algorithm.

In HYCOM, three types of floats/drifters are supported based on the specified vertical advection rules. To follow water parcels, the diagnosed vertical velocity field is used to advect three-dimensional Lagrangian floats. Isobaric floats remain at prescribed pressure levels while isopycnic floats remain at the depths of prescribed density surfaces. These latter two float types are included because actual drifters released in the ocean are usually one of these two types. For example, surface drifters can be specified by setting the type to isobaric and setting the initial drifter depth to be within model layer one. The user can also specify that the model be seeded with synthetic moorings, in which case no advection is performed. These moorings can provide high-frequency sampling of the water column at prescribed locations, which can be at the locations of observational moorings to facilitate model-data comparison. Dynamical and thermodynamical water properties are interpolated to the location of each float. Time series of float position and depth, along with the interpolated water properties, are archived for further analysis. If synthetic moorings are specified, velocity components u , v , w are output instead of float position and depth.

The detailed algorithms for the FLOAT package can be found HYCOM web site (<http://oceanmodeling.rsmas.miami.edu/hycom/documentation.html>)

CHAPTER 4

MODEL VALIDATION

In this section, sea surface temperature (SST), sea surface seight (SSH) and sub-surface temperature obtained from a seasonal run of the HYCOM Caspian Sea model are compared with the available observations. Model SST and SSH comparisons are made with seasonally analysed satellite observations which provide extensive spatial coverage of sea surface properties. Sub-surface temperatures are compared with the Russian climatology data set which was used to initialize the model.

4.1 Model comparison with Pathfinder SST

Several statistical metrics were used to intercompare monthly mean SSTs obtained from the climatologically forced HYCOM simulation and to compare them with a satellite-based climatological SST dataset at each model grid points. For evaluation of the model results, monthly mean SSTs were formed from daily fields using the last model year (year 8).

A statistical evaluation was performed by using the climatological NOAA Advanced Very-High-Resolution Radiometer (AVHRR) Ocean Pathfinder global equal-angle SST data (Version 5.0) as reference. Since the spatial resolution of Pathfinder SST is similar to model resolution of $\sim 4km$, the Pathfinder climatology is suitable for the model-data comparisons.

Comparison of the SST values predicted by the model (HYCOM SST) and

those from the climatology (Pathfinder SST) was made using several statistical measures. Pathfinder SST was interpolated to the model grid, and the time series compared using the following statistical relationships between the monthly mean Pathfinder SST (X) and HYCOM SST (Y) at each grid point:

$$ME = \bar{Y} - \bar{X} \quad (4.1)$$

$$rms = \left[\frac{1}{n} \sum_{i=1}^n (Y_i - \bar{X}_i)^2 \right]^{1/2} \quad (4.2)$$

$$R = \frac{1}{n} \sum_{i=1}^n (X_i - \bar{X}) \frac{(Y_i - \bar{Y})}{(\sigma_x \sigma_y)} \quad (4.3)$$

$$SS = R^2 - \underbrace{\left[R - \left(\frac{\sigma_y}{\sigma_x} \right) \right]^2}_{B_{cond}} - \underbrace{\left[\frac{(\bar{Y} - \bar{X})}{\sigma_x} \right]^2}_{B_{uncond}} \quad (4.4)$$

where $n = 12$ for the 12 months of data, ME is the mean error, rms is the root-mean-square difference, R is the correlation coefficient, SS is the skill score, and $\bar{X}(\bar{Y})$ and $\sigma_x(\sigma_y)$ are the mean and standard deviations of the Pathfinder and HYCOM SST values, respectively.

The nondimensional skill score SS in above equation includes conditional and unconditional biases (Murphy 1992). It is used for the model-data comparisons because one needs to examine more than the shape of the seasonal cycle using R (and SS). The nondimensional SS measures the accuracy of SST simulations relative to Pathfinder SST. The conditional bias (B_{cond}) is the bias in standard deviation of the HYCOM SST, while the unconditional bias (B_{uncond}) is the mismatch between the mean HYCOM and Pathfinder SST. The value of R^2 can be considered a measure of "potential" skill, that is, the skill that one can obtain by eliminating bias from the HYCOM SST. Note that the SS is 1.0 for perfect HYCOM SSTs, and positive SS is considered as a successful simulation. The nondimensional SS takes bias into account, something not done by R . Part of the reduction in SS values in comparison to R stems from the squaring of correlation in the SS calculation. Biases are

taken into account in the rms differences, but in some cases the latter can be small when SS and R are poor. This can occur where the amplitude of seasonal cycle is small.

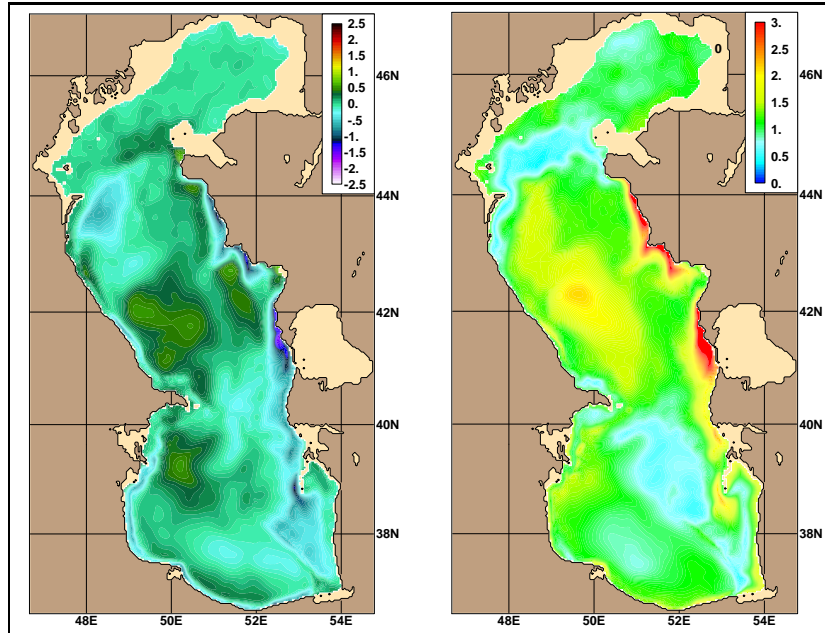


Figure 4.1: Annual mean model SST mean bias ($^{\circ}C$) and RMS difference ($^{\circ}C$) with respect to the satellite-based Pathfinder SST climatology

Annual mean HYCOM SST error and rms SST difference calculated over the seasonal cycle with respect to the Pathfinder climatology are shown in (Figure 4.1). The departure of climatological annual mean HYCOM SST from the Pathfinder SST in Figure 4.1a indicates SST errors of less than $\pm 0.5^{\circ}C$ in the interior of the Caspian Sea, with relatively higher deviation southwest of the MCS and south of the Apsheron peninsula where eddy features are present. Near the eastern continental boundaries, especially in the upwelling region, the error of model estimated SST reaches a value of $-1^{\circ}C$, with the model SST being cooler than the Pathfinder SST. A similar pattern is observed in the rms SST difference statistics: while the rms difference is less than $2^{\circ}C$ over the most part of the sea, it reaches a value of $3^{\circ}C$ in the upwelling region. In

summary, the model has successfully reproduced the observed SST structure in general, with relatively higher SST deviations in dynamically active regions, primarily at the upwelling region.

Monthly mean differences between model generated and Pathfinder SST fields, shown in (Figure 4.2) vary between $-2.5^{\circ}C$ and $+2.5^{\circ}C$. Accordingly the model seems to underestimate the surface temperatures in summer and overestimate it in winter, which may indicate a more active mixing in the model as compared to what may be actually required. In summer, model SST has the highest negative deviation in the upwelling region, which may be because of sharper upwelling features in the model. In contrast, the highest positive mean error in winter months occurs at the center of the anticyclonic eddy in the Middle Caspian Sea, where the mixed layer depth has a maximum value.

With SST measurement accuracy limits of $0.5^{\circ}C$ of best satellite sensors and given the fact that satellite derived temperatures near the coasts are problematic due to contamination by land effects, the level of success in our simulations are understandable. There may be an additional reason for differences near the coast, associated with the application of land-sea mask used in the ERA-40 atmospheric re-analysis data used for specifying surface fluxes (Kara 2007). Increased error near the eastern boundary could also be related with the quality of satellite detection, possibly being influenced by atmospheric conditions of the adjoining deserts.

The skill with which the HYCOM model predicts SST is specifically reflected in the *SS* maps in Figure 4.3, indicating values close to 1 over most of the Caspian Sea, except in the upwelling region. The highest skill *SS* is obtained at the shallow northern part. The minimum *SS* value is 0.46 at the upwelling region, supporting a successful prediction. It is in fact surprising that SST is so well simulated by the model, without any data assimilation.

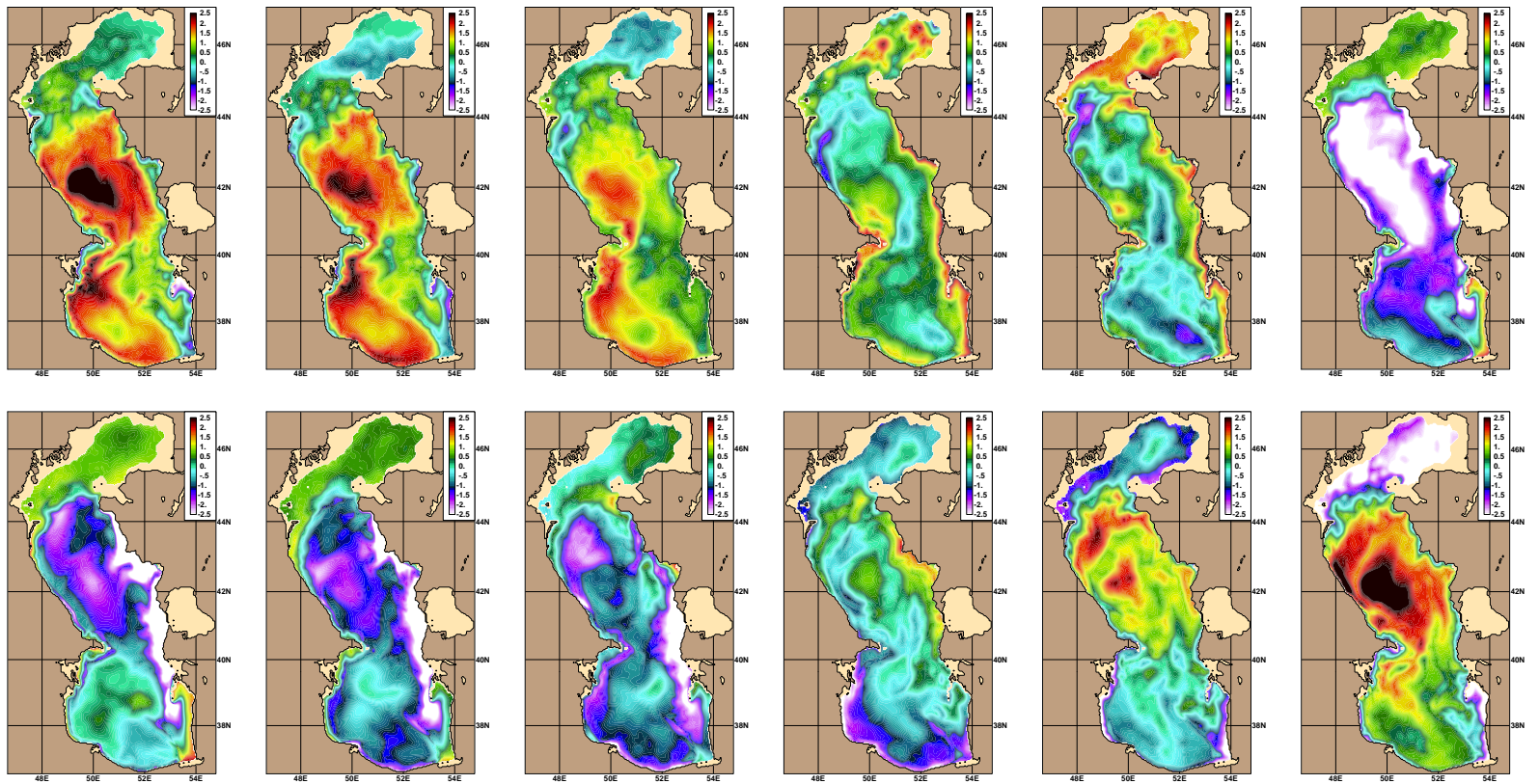


Figure 4.2: Climatological monthly mean model SST Mean Error ($^{\circ}$ C) with respect to the Pathfinder SST climatology which has a resolution of 4km. upper figures: From January June, lower figures: From July to December

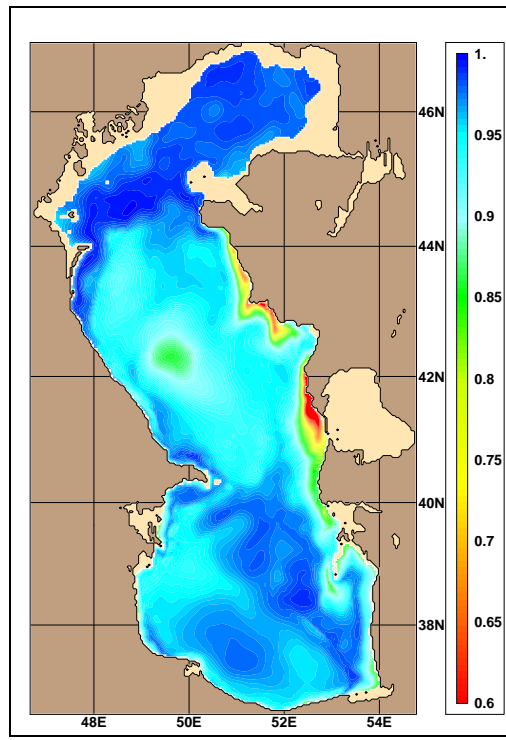


Figure 4.3: Skill score

4.2 Model comparison with satellite derived sea surface height

The model generated sea surface height was compared with the satellite measurements. Since the satellite can only measure the sea level anomaly (SLA), to evaluate the model performance, SLA is calculated first by subtracting the annual mean model sea surface height (SSH) from the monthly mean values of the model SSH. The measurement period for the satellite derived climatological SSH differs from the averaging time period of the ECMWF re-analysis data which were used to force the model. However, the comparisons were made by assuming that the permanent circulation patterns have seasonal variations and do not show strong interannual variations.

Satellite derived SLA in the Caspian Sea shows strong seasonal variability. The basin-wide cyclonic circulation in the MCS and SCS deduced from the

SLA in winter months becomes anticyclonic in summer. Although this summer time circulation pattern can not be clearly inferred from hydrographic data, the satellite derived SLA clearly indicates this anticyclone during the summer and supports the model results. The anticyclonic cell in the MCS reaches its maximum intensity in August, then becomes weaker and finally disappears in October.

Figure 4.4 and Figure 4.5 compare the model based and the satellite derived SLA in the months of January and August respectively. Considering that these two climatological monthly mean fields are based on climatologically different time periods, in general the T/P-J1 SLA and HYCOM SLA are in good agreement.

Figure 4.4 shows the evaluation of SLA in January, please note the different color scale of this two figures. In general model derived SLA has lower values compared to the satellite derived SLA. This bias could be related with the imperfectness of the water budget balance of the model. Another possible reason may be improper representation of the mean sea surface and inverse barometric effect which are subtracted from measured altimetry of the satellite data. There is a basin wide cyclonic circulation in this month, negative SLA values are present over the whole basin. The cyclonic circulation reaches maximum intensity in the center of the MCS evident in both satellite and model derived SLA maps. The only difference between two figures is the SLA over the shallow northern basin. While model derived SLA has positive values over this basin, satellite derived SLA has negative values.

Winter time basin-wide cyclonic circulation type turns to anticyclonic one in summer. The maximum positive values of SLA is observed reaching to 15-20 cm in August. Figure 4.4 shows the model and satellite derived SLA in August. The satellite SLA indicates two anticyclones over the two deep basins of the Caspian Sea. The model SLA also indicates two anticyclonic cells, but the intensity of the anticyclone in the SCS is lower compared to the satellite SLA. There is no detailed information deduced from the hydrographic observations

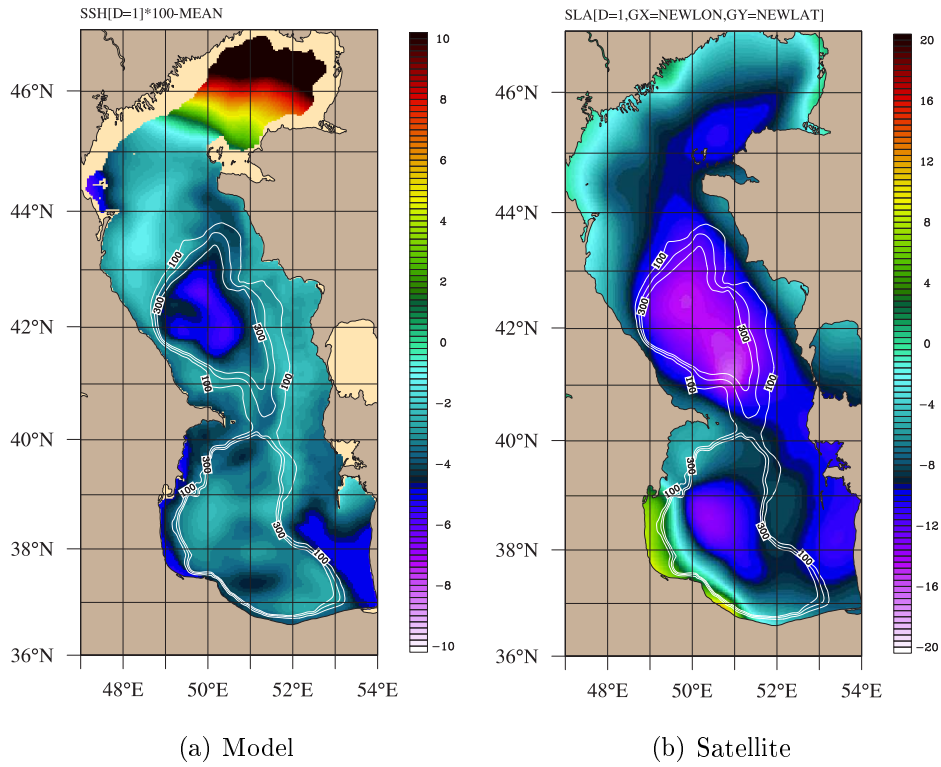


Figure 4.4: Model and satellite based Sea Level Anomaly (SLA) (m) in January. Note the different scale in each figure.

about the existence of the anticyclonic cell in the center of the MCS observed in the summer months. However, the satellite derived SLA shows this anticyclone and it is agree with the model derived SLA.

In other months, model and satellite SLA shows good agreement in structure and location of the cyclonic / anticyclonic gyres, however model derived SLA underestimates SLA values compared to the satellite derived SLA. Given the fact that the averaging period for the construction of the climatology differs from each data set, the model performance is good.

4.3 Comparison to Climatological observations

Model evaluation was also made by comparing the model sub-surface temperature with the climatology of the available sub-surface observations.

Figure 4.6 shows the temperature section along the $51^{\circ}E$ transect for the

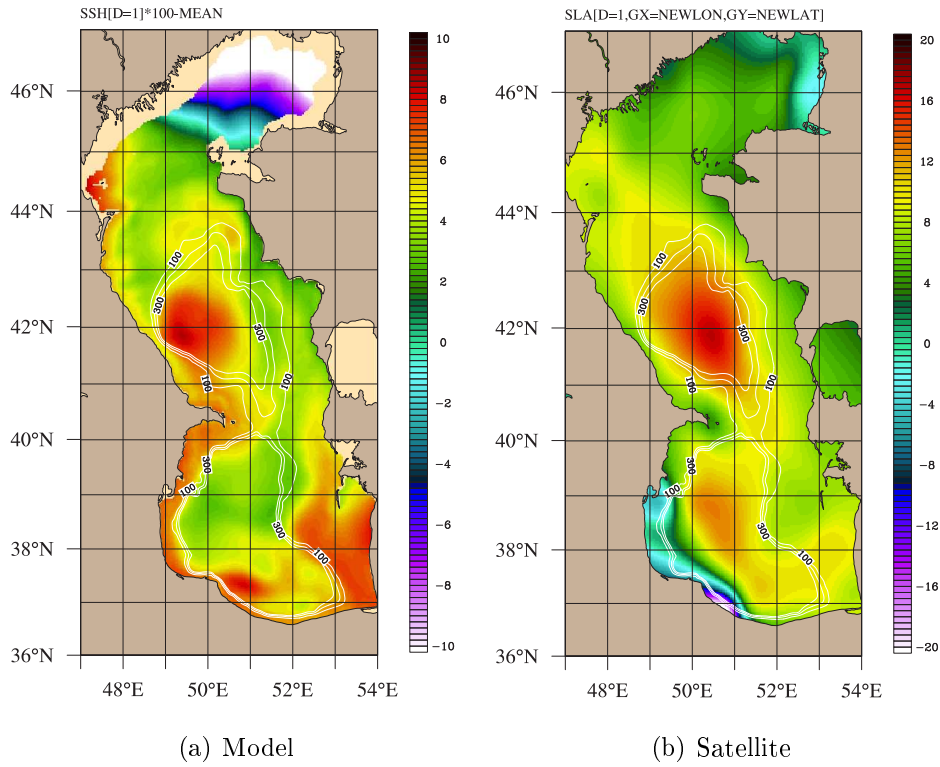


Figure 4.5: Model and satellite based Sea Level Anomaly (SLA) (m) in August. Note the different scale in each figure.

month of August. Upper figures shows the observed temperature, lower figure shows the model derived temperature. Although there is general agreement between the model results and the observations, there are some differences in vertical structure. In both figures, a strong thermocline is seen at about a depth of 30 m. The stratification obtained from the observations and model results differ in the deeper part of both basins, with the model temperatures being higher than the observed values in the 50–25 0m depth interval. The quality of the information contained in the Russian climatological data is not known. On the other hand, if we trust the quality of these observations, the model is seen to successfully reproduce the summer thermocline and with some differences, the sub-surface temperature stratification.

Basin-wide comparison of observed and model sub-surface fields was made by averaging temperature at 0, 10, 50 and 150 m depths. Figure 4.7 shows the model derived temperature and the climatology from observations at these

depths. There is clear agreement between the model (red triangles) and the observations (solid line) near the surface and at thermocline level, while differences of up to $1 - 2^{\circ}\text{C}$ occur at greater depths. The HYCOM generated temperature is closer to the climatology in summer, compared to the other months. Strong agreement between the modelled and observed temperature stated that HYCOM Caspian Sea model is successful to model the thermodynamics adequately.

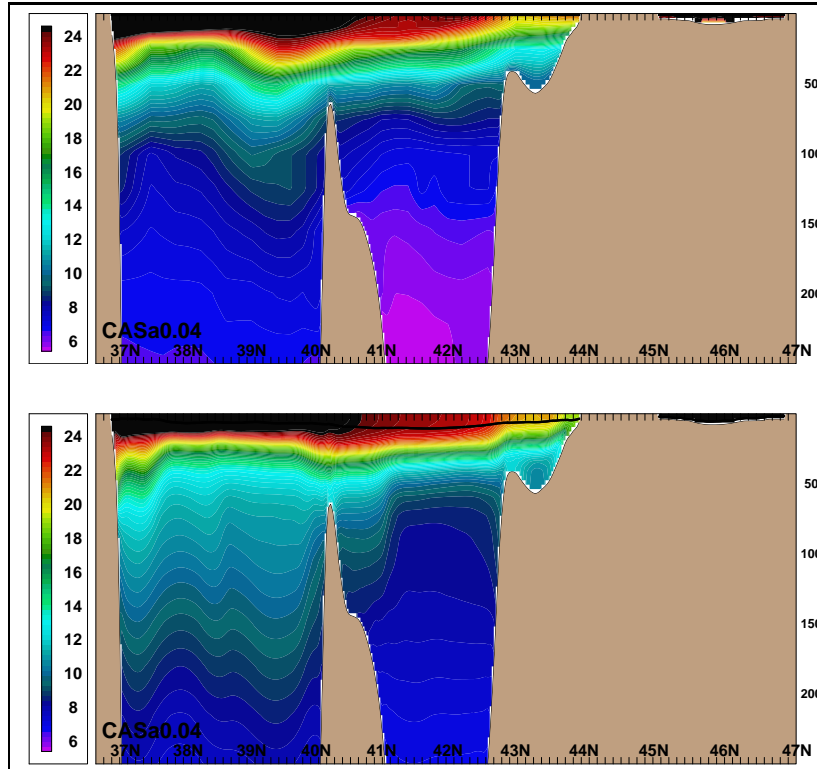


Figure 4.6: Comparison of observed (upper figure) and modelled temperatures $^{\circ}\text{C}$ along the 51°E transect for the month of August.

Salinity comparison is more complex. The quality of the observed salinity data is not clear, especially in the deeper part of the sea. Comparison of the salinity with the model shows a clear difference with increasing towards to the deeper depth. The minor source of the salinity in the Caspian Sea is the

Volga river and evaporation at the sea surface. Although the Volga discharge is known at some accuracy, the calculation of surface water budget is not easy. The possible reason for the variation of the evaporation minus precipitation will be investigated later on this thesis.

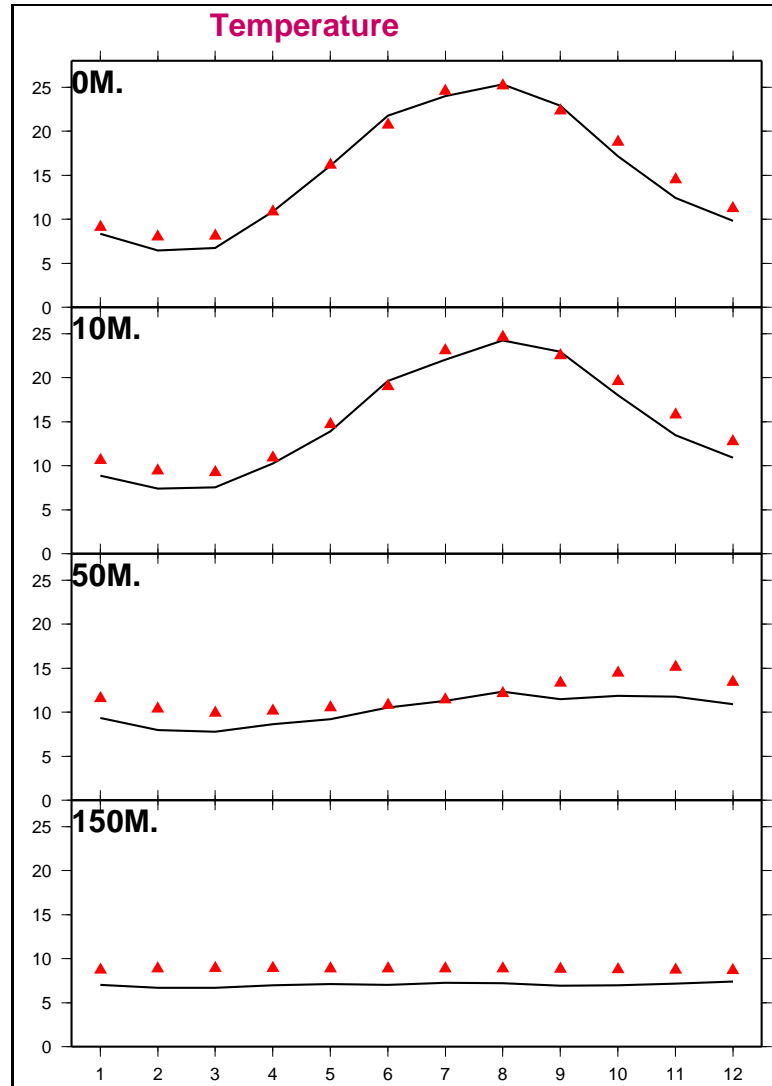


Figure 4.7: Basin averaged model and climatology temperature $^{\circ}C$ at depths of 0, 10, 50, 150 m. Solid lines are climatology from observation, red triangles are model temperature.

CHAPTER 5

ANNUAL MEAN AND SEASONAL ANALYSIS

5.1 Circulation

In this section, seasonal and annual mean circulation are described, based on a seasonal run of the HYCOM Caspian Sea model initialized with monthly climatological hydrographic data and forced with monthly climatological surface fluxes described in Chapter 2.

Figure 5.1 shows the annual mean circulation of the Caspian Sea, where current velocity vectors averaged over depth intervals of 0-30 m, 30-150 m, 150-300 m. While daily variations of the surface currents in the Caspian Sea can be quite strong, annual mean averaged currents are relatively weak, of the order of a few cms^{-1} with maximum speed reaching $7 - 8cms^{-1}$ along the coastal regions. As stated by various authors, the Caspian Sea surface currents are strongly correlated with the wind, which is known to have significant directional variability on a daily basis. As a result, the annually averaged currents have low values.

The circulation in the shallow Northern Caspian Sea is very sensitive to the wind direction and speed. As a result, there are no stable current patterns and the annual mean current magnitudes in this region are very weak. Yet, the annual mean circulation indicates northward mean currents, which varies

considerably from one season to another.

The most striking features of the Caspian Sea circulation are the anticyclonic gyres in the western part of the MCS at $42^{\circ}N$ of the Derbent depression and the cyclonic/anticyclonic paired gyres at $38^{\circ}N$ and $39.5^{\circ}N$ in the deepest part of the SCS. All of these strong circulation cells at the topographic depressions are mostly barotropic features preserving their shape and location from surface to the bottom.

All three cells are persistent throughout the year but their intensity is increased to a maximum in summer, consistent with the seasonal changes in the wind field. Since wind-driven transport is a dominant part of the circulation in large water bodies like the Caspian Sea, the increase in current magnitude is reasonable, since the wind magnitude also increases in summer.

Southward surface currents along either side of the Caspian Sea are observed features which are successfully reproduced by the model. The southward currents along either coast seem to be trapped very near the coast (*depth* $< 20m$). The intensity of the current along the western coast decreases south of $42^{\circ}N$, as part of the current becomes incorporated in the anticyclonic offshore gyre and after recirculating around it, enters the SCS along the 100 m contour on the western side of the Apsheron sill. The southward surface current along the eastern coast of the MCS is also a well known feature of the MCS in the summer. This southward current at the surface changes direction to the north in the deeper levels. This circulation pattern suggests the existence of a basin-wide cyclonic circulation in the MCS. However, the persistent feature identified as the Derbent anticyclone in the western part of the basin is located inside the described cyclonic cell.

Throughout the year, a continuous southward flow is evident over the full water depth offshore of the Apsheron peninsula at the western side of the Apsheron sill. The current velocities are greater at the surface and decrease towards to bottom. This southward current is an observed feature of the Caspian Sea circulation (Kosarev and Yablonskaya, 1994). While southward

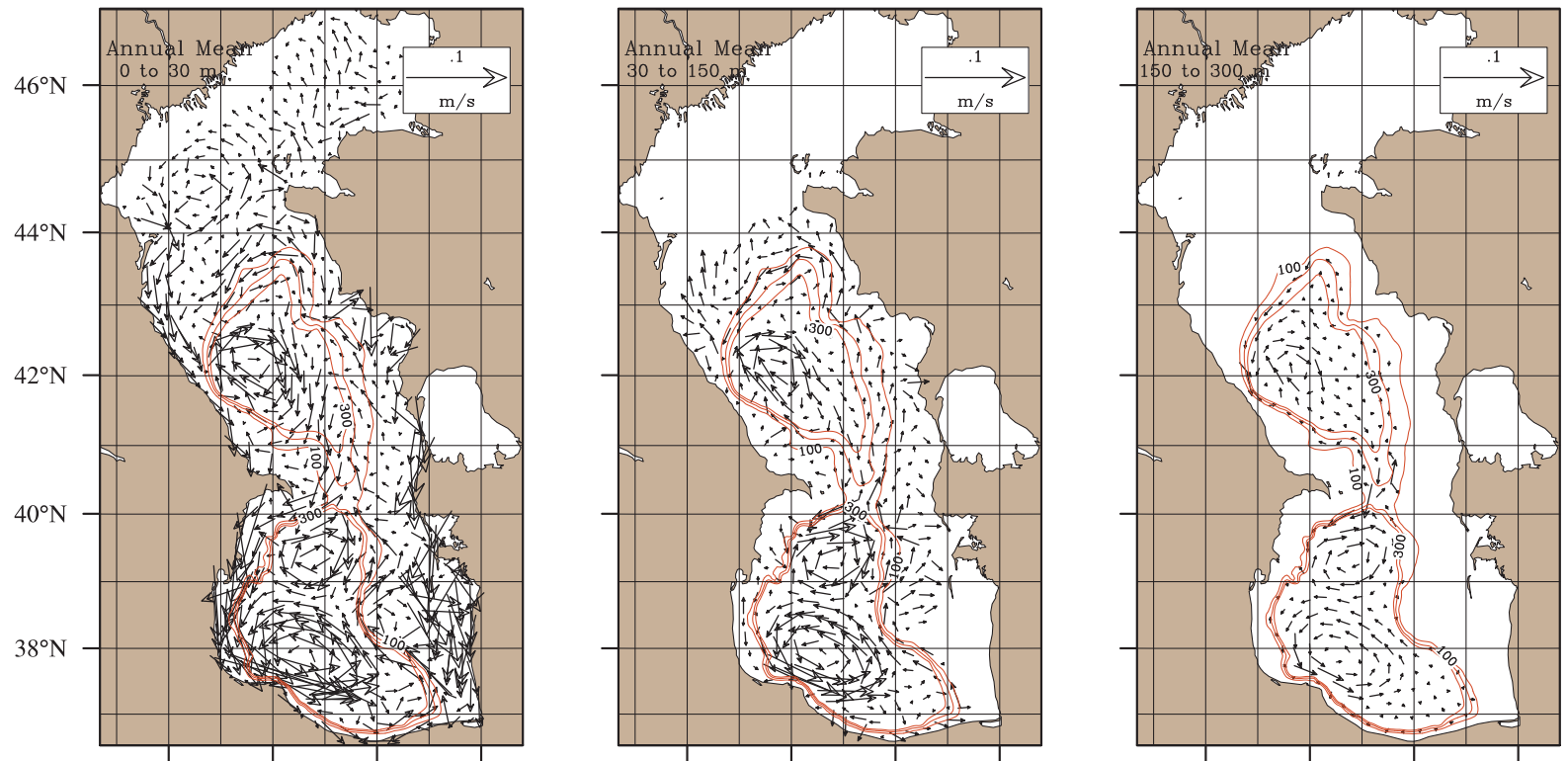


Figure 5.1: Model-derived annual mean currents (cms^{-1}) from control run averaged over depth intervals of 0-30 m, 30-150 m and 150-300 m. Red lines shows the 100, 200, 300 m bathymetry contours.

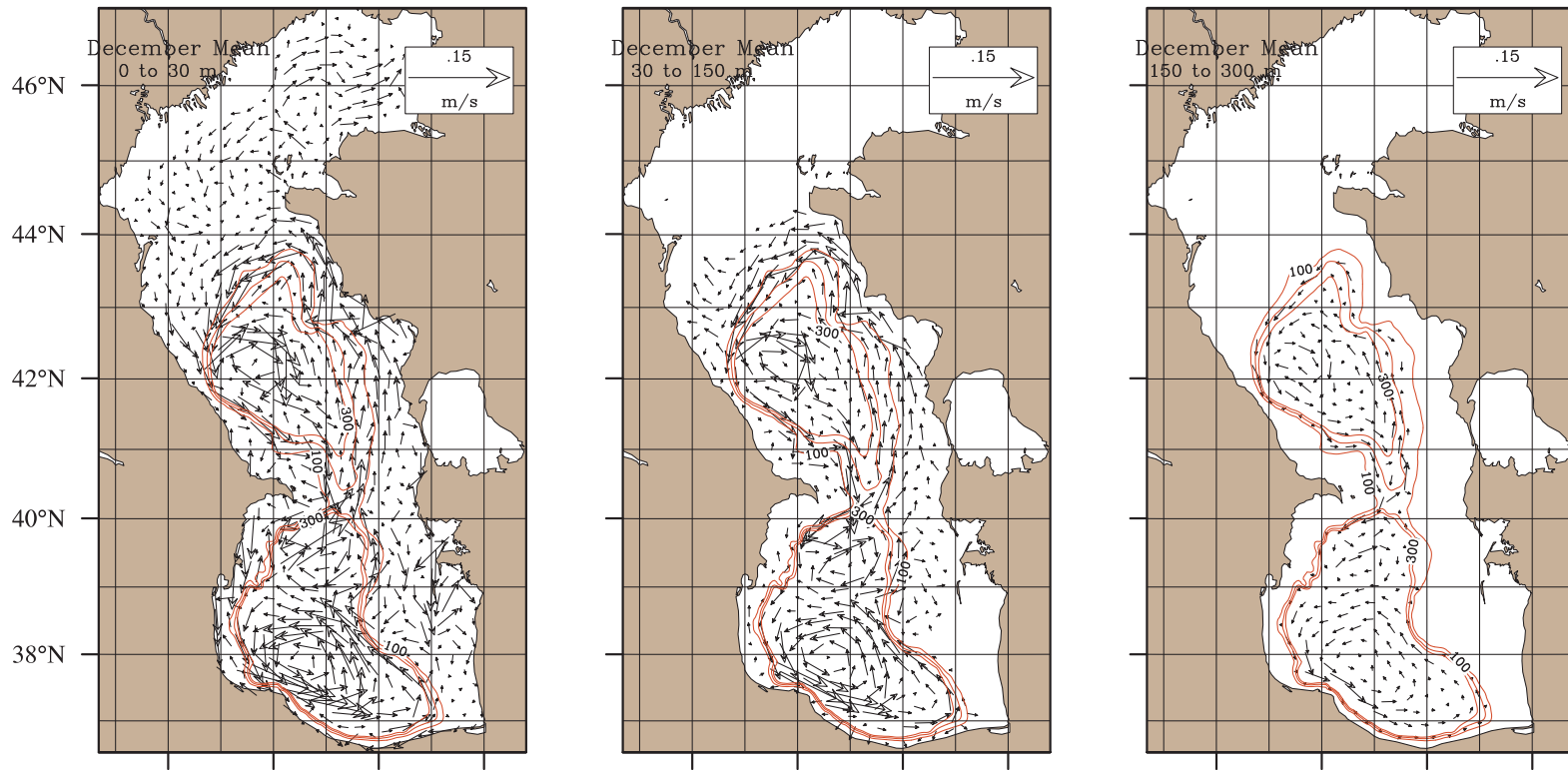


Figure 5.2: Model derived monthly circulation from control run averaged over the 0 to 30m, 30 to 150m and 150 to 300m for December

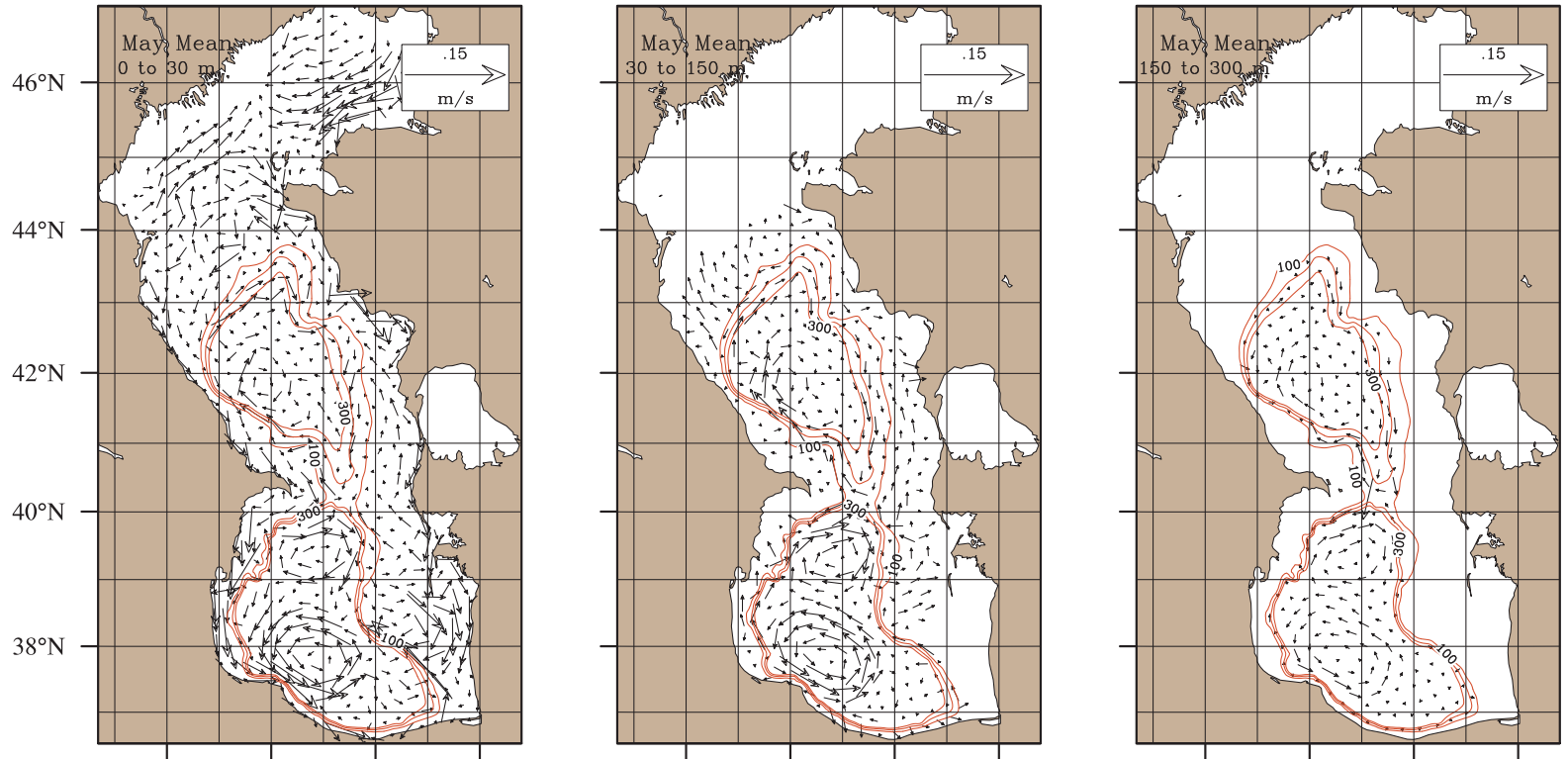


Figure 5.3: Model derived monthly circulation from control run averaged over the 0 to 30m, 30 to 150m and 150 to 300m for May

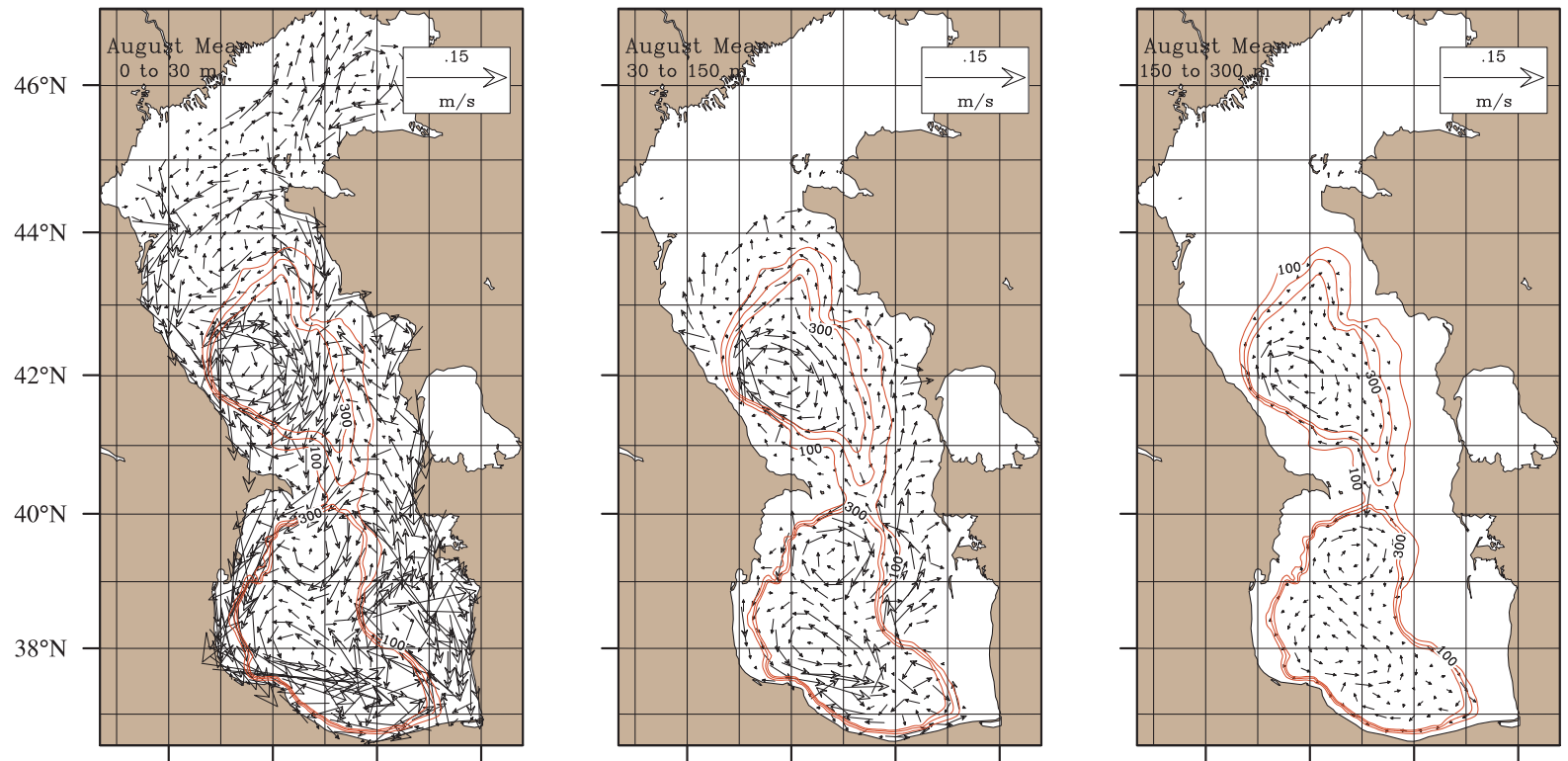


Figure 5.4: Model derived monthly circulation from control run averaged over the 0 to 30m, 30 to 150m and 150 to 300m for August

currents are evident at the western side of the sill, a northward current occurs on its eastern side, transporting warm water of the southern basin to the north. This northward current is also evident from satellite SST data, as a vein of warm water originating from the SCS flowing towards the MCS at the eastern coast. Sill topography appears to be an important factor controlling the exchange between the two basins, which in turn is tied to the structure of the seasonal circulation in the adjacent basins.

In the South Caspian Sea, a persistent dipole pattern and a basin-wide cyclonic circulation trapped in 100-300 m bathymetry contour are observed. The cyclonic shallow circulation encircles the inner basin dipole pattern. Of the dipole structure, the cyclonic cell is located in the southwestern part of the basin, while the anticyclonic cell is located to its north. The anticyclonic cell, identified as the 'Kura anticyclone' by Trukhchev *et al.*, (1995) and Tuzhilkin *et al.* (1997), has first been described by Lednev (1943). These authors have also found the cyclonic cell in the southeastern part of the SCS. This dipole pattern is a permanent feature of the SCS, evident during the whole year, with a mainly barotropic structure extending from the surface to the bottom. The southward currents originating from the MCS pass the sill offshore of the Apsheron peninsula, progressing in the form of a coastal jet along the western coast of the SCS. This coastal current reaches its maximum intensity when it becomes concentrated along the inner part of the shelf along the western SCS. The coastal jet follows the shallow bathymetry to turn clockwise around the SCS along the 100-300 m bathymetric contours, finally arriving at the eastern side of the Apsheron sill. Outside of the shallow cyclonic circulation and in the shallow, wide shelf area at the very eastern limits of the SCS, strong southerly currents are observed.

The circulation at the surface, at intermediate depth below the mixed layer and at depth are schematized in Figure 5.5 based on the annual model circulation maps presented earlier in Figure 5.1. The figures were constructed by eliminating the currents that have windspeed values greater than 2.5 cm/s for

the surface, 1 cm/s for the intermediate depth, 0.3 cm/s for the deep part.

The surface circulation (Figure 5.5(a)) consists of narrow jet-like coastal currents very near the coast, flowing south along the entire western and eastern coasts and originating in the north. Part of these currents escaping the near-coastal veins, especially near headlands and in proximity to other strong circulations are incorporated in these other elements of circulation. In this way, the coastal jets and the anticyclonic / cyclonic gyres in the individual basins are interconnected by thin streams of currents which follow the coast and the continental slopes. In a number of cases a strong current following a stream is diverted by a nearby feature and turns opposite to its first orientation; for example at the headland along the northeast coast, along the western coast in the proximity of the anticyclonic gyre of the NCS, at the southern coast and on the eastern sides of the dipoles in the SCS.

The intermediate circulation, Figure 5.5(b), is much simpler, and consists of the anticyclone in the NCS and the cyclone/anticyclone pair in the SCS, and a south to north current along the main eastern basin topographic slope (which is about mid-basin in the SCS and closer to the eastern coast in the NCS). This northward current then connects to the cyclonic / anticyclonic cells weighted in the western side of the basin.

The deep circulation, Figure 5.5(c), consists only of the anticyclonic cell in the NCS and the cyclonic / anticyclonic pair in the SCS, without and appreciable slope current joining them.

Overall, the three major cells of circulation and shelf currents displayed in Figure 5.5 appear to have significant barotropic components. To explore further the barotropic currents of the Caspian Sea, vertical average currents calculated on a monthly basis are shown in 5.1. The winter circulation appears relatively simpler, with the currents basically encircling the middle and southern depressions of the Caspian Sea, following major topographic slopes. This may be a result of the decrease in vertical stratification in winter. At the centers of the depressions again the barotropic signals of the anticyclonic

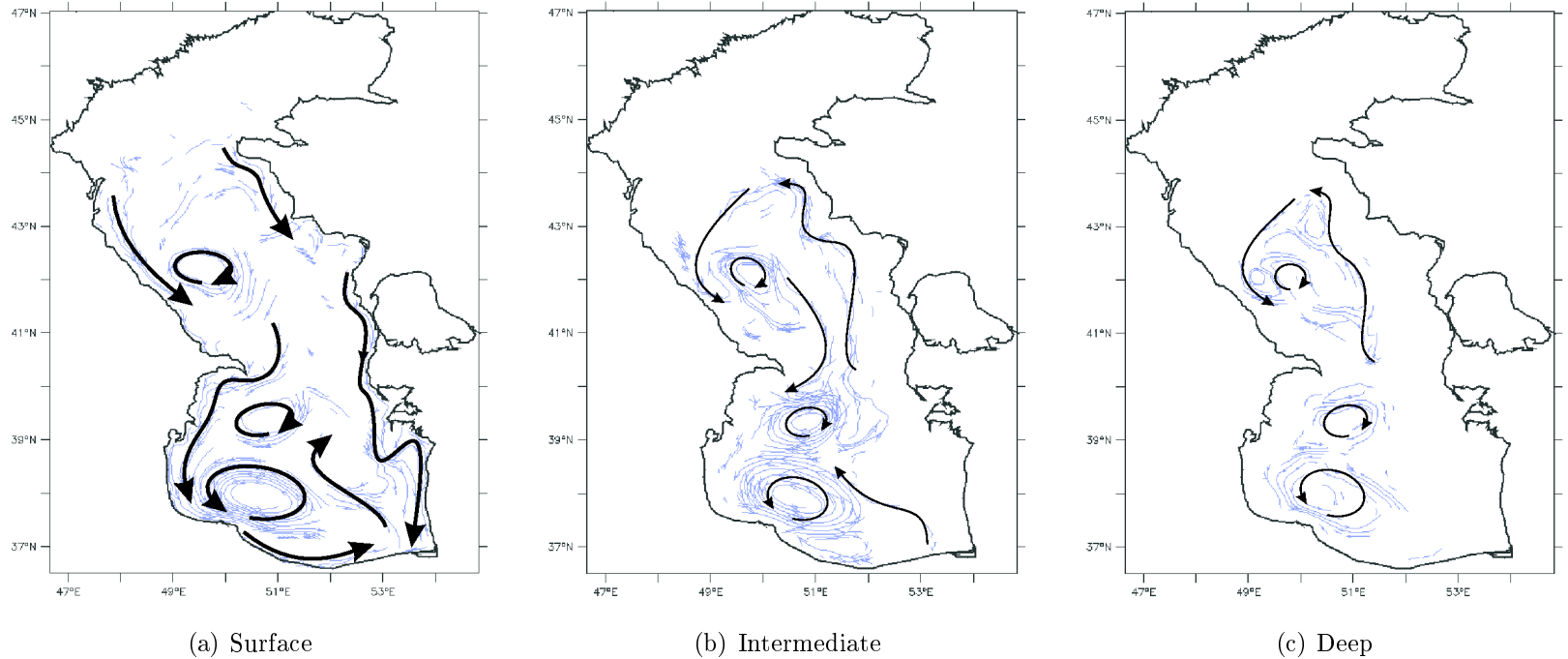


Figure 5.5: Schematic representation of annual mean circulation of the Caspian Sea for the depth ranges (a) Surface (0-10 m), (b) Intermediate (50-100 m) (c) Deep (200-1000 m).

eddy in the NCS and the cyclone / anticyclone pair in the SCS survive, although their intensities are much reduced in the barotropic circulation is much reduced because their signatures are mainly concentrated near the surface.

In the spring, the barotropic circulation breaks up into a set of cyclonic and anticyclonic cells in the deep basins, but a much wider cell of circulation exists in the shallower parts, completing a cyclonic cell and connecting to the deep basin circulations through a number of escape points.

Monthly mean circulation averaged over depth intervals of 0-30 m, 30-150 m, 150-300 m, are plotted in the Figure 5.2, Figure 5.3 and Figure 5.4. The Caspian Sea currents are more energetic during the summer and autumn, while the winter is relatively calm, and the spring is a transition season. A cyclonic surface circulation dominates the Caspian Sea from December to March, when the wind blows from the east and north-east directions. The circulation of the MCS becomes anticyclonic at the beginning of June, when strong north, north-west winds prevail.

In the MCS, the currents are relatively weak in most part of the basin except the jet currents near the coasts and within the anticyclonic cell detected earlier in the middle of the basin. From October to January, a basin-wide cyclonic cell is evident. The northward current flowing along the SCS enters the MCS at the eastern coast of the Apsheron sill, following the 100-300 m bathymetry contours. After reaching the northernmost part of the basin, this jet turns to the west and follows the western coast with increased velocity. The Derbent anticyclone shows some seasonality: it is weakened in winter and almost diminished in April but becomes stronger in June. The northward flow along the eastern coast of the MCS, transporting warm water originating from the SCS is evident in autumn to winter months. (In summer, this flow is diminished because of the strong Ekman circulation connected with the upwelling.

In the SCS, the dipole pattern detected in the annual mean circulation is more stable compared to the circulation patterns in the other two basins. This feature is confirmed by the earlier results of Peeters et al. (2000), who showed

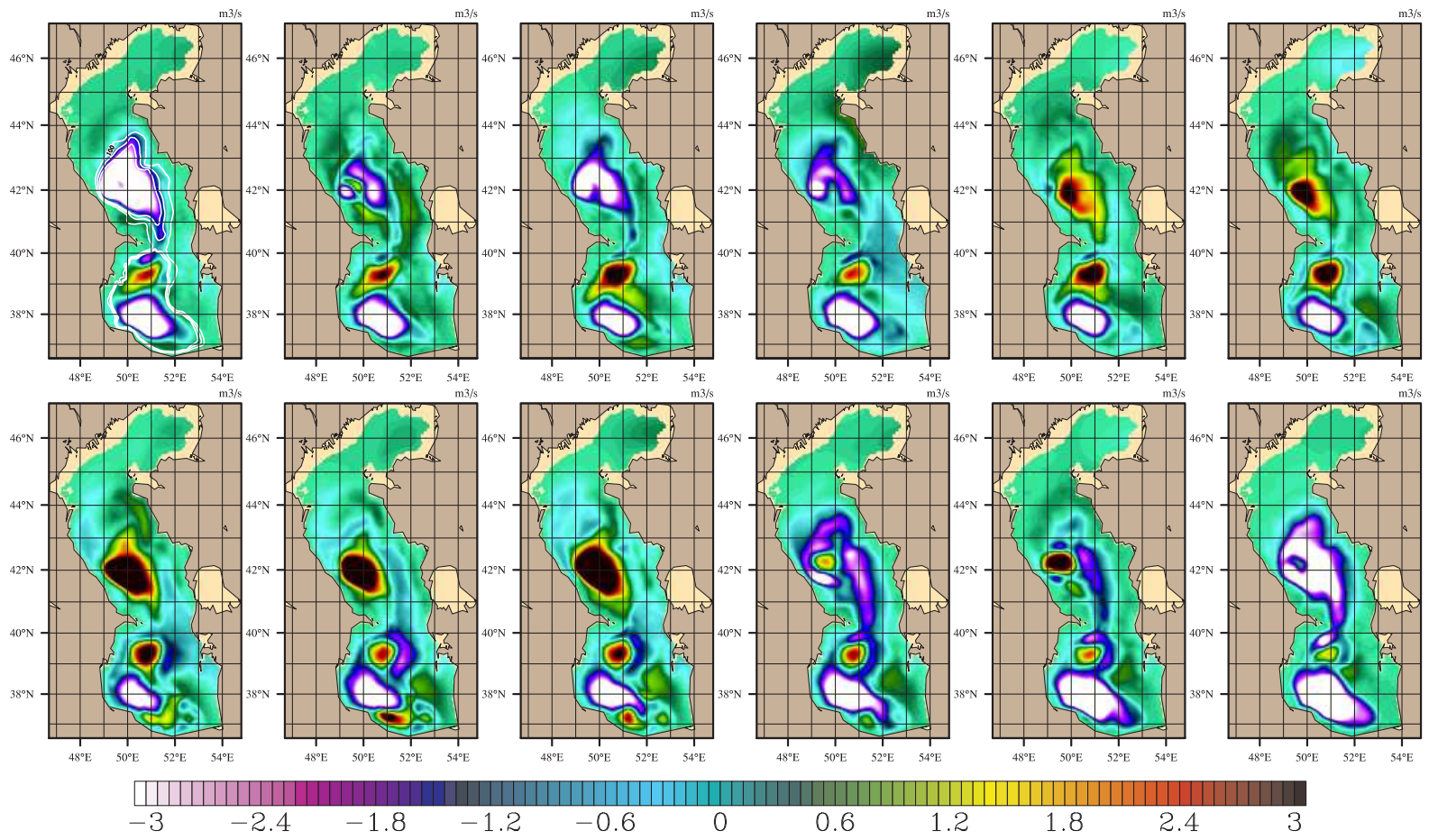


Figure 5.6: Climatological monthly mean barotropic stream function (m^3/s) over the Caspian Sea from January through December

the enhanced stability of the SCS basin relative to the MCB, based on Brunt Vaisala frequency calculations of deep CTD casts.

Northward annual mean current velocity at four different sections are shown in Figure 5.7. These sections are selected at the center of the MCS, across the Apsheron sill, along $38^{\circ}E$ and along $39.5^{\circ}E$. Southward coastal currents are observed to flow along both the western and the eastern coasts of the MCS, as shown in Figure 5.7a. The current appears trapped very near the coast, where velocities exceeding 2 m/s are encountered. Just below the surface on either side of the basin, counter currents are found to flow north. On the eastern side, the northward current has maximum intensity trapped along the coast, with a maximum value reached at depths of 50-100 m. Figure 5.7 b shows the northward velocity component along the Apsheron peninsula, where two current cores in opposite directions, are detected. While the southward currents are concentrated along the western coast with a maximum value centered around 70 m depth, opposing northward currents are evident along the eastern coast.

The northward current at the $38^{\circ}E$ latitude section (Figure 5.7 c), along the western coast of the SCS is a branch of the anticyclonic cell flowing towards the Apsheron peninsula. The southward current on the western side and the northward current along the eastern side at the $39.5^{\circ}E$ latitude section (Figure 5.7 d) are associated with the cyclonic cell at this latitude.

5.2 Temperature

The most challenging task for modelling of enclosed-seas like Caspian Sea is to properly represent the annual thermal cycle, since the thermal regime changes from an entirely thermally mixed one in winter, to a strongly stratified one in summer (Beletsky and Schwab 2001, who detected the same sequence in the case of lake Michigan). Our simulations with the HYCOM Caspian Sea model were able to reproduce the following main features of the Caspian Sea thermal

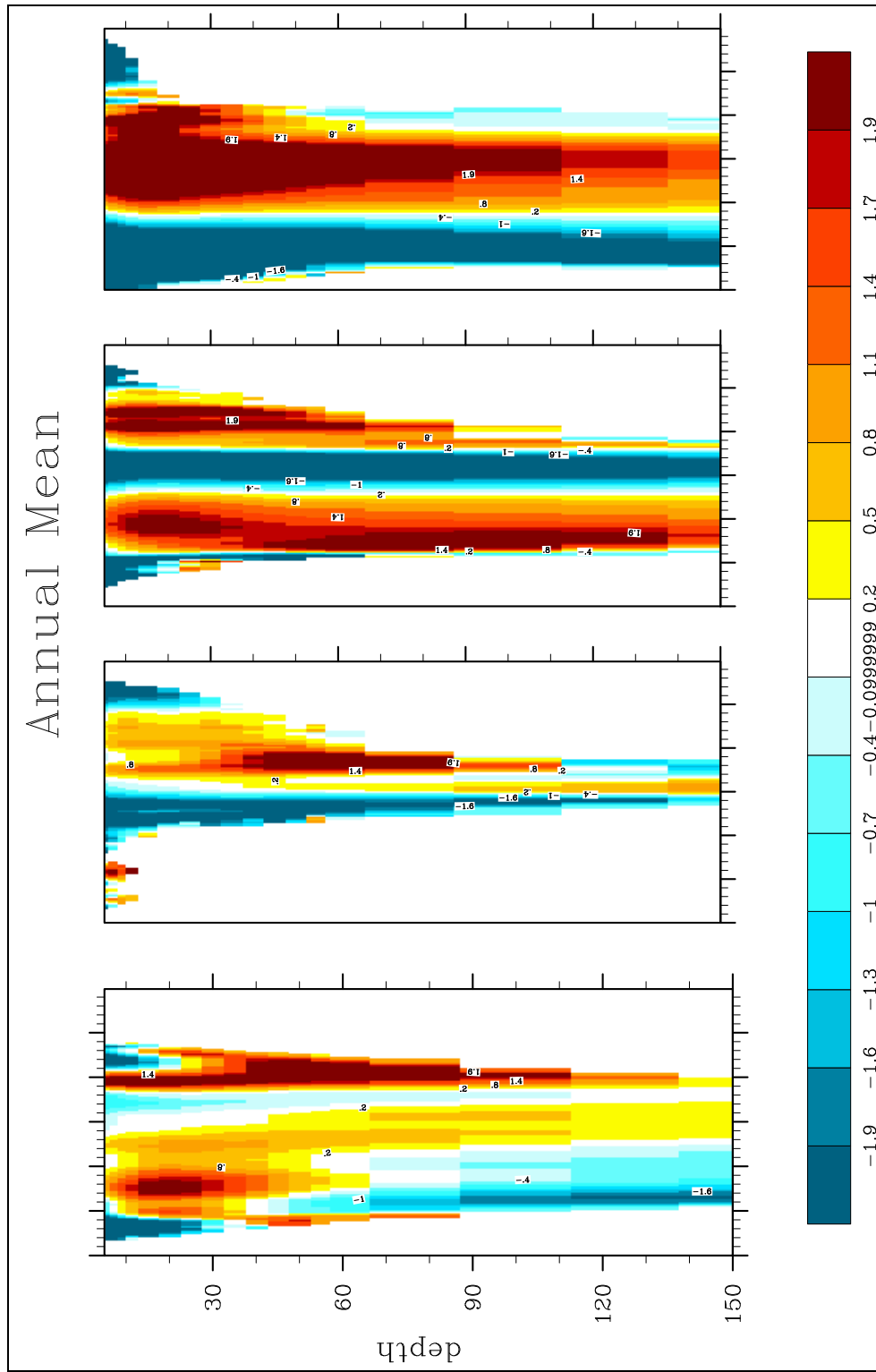


Figure 5.7: Vertical cross-section of the annual mean alongshore currents along (m/s^{-1}) the (a) center of the MCS, (b) Apsheron peninsula (c) $38^{\circ}E$ and (d) $39.5^{\circ}E$.

structure.

Figure 5.8 shows the temperature cross sections along $50^{\circ}E$ in different months of the year. In this figure, the black line shows the base of the mixed layer. (The MLD is the shallowest depth at which the density change with respect to the surface is the equivalent of $0.2^{\circ}C.$, Kara et. al 2000). Throughout the year there are considerable differences in mixed layer depth (MLD) between the two deep basins of the Caspian Sea. While the MLD in MCS is about 100 m in winter, it only reaches to 20 m in the SCS. The most striking feature of the temperature stratification is the sharp contrast between the vertical gradients and the relative levels of temperature in the MCS and SCS basins, which results from the difference in mixing and the effect of the Apsheron sill separating the two basins.

In the beginning of January, the upper 100 m of the two basins are well mixed, with the mixed layer existing till the end of April. In winter months, the sharp thermal fronts limiting continental shelf areas are evident, indicating effective shelf mixing and cooling processes leading to dense water formation (Figure 5.29).

Since the density in the Caspian Sea is largely determined by temperature (in the absence of a strong salinity stratification), the temperature contrasts between basins reflect pressure gradients developing as a result of density differences. The largest temperature differences at sill level develop in late winter and early spring when differential mixing and cooling occurs in the two basins. As a result, the dense water in the MCS is expected to flow south across the Apsheron sill to the SCS. The weakness of thermal stratification in the SCS during the following periods appears partly to be a result of the sill overflow and ensuing thermocline level injections of dense water from the MCS into the SCS. Temperature isolines of colder water on the Apsheron sill area connected to those at thermocline level of the SCS provides limited evidence in this direction.

Starting in April, the surface layer of the SCS begins to warm more rapidly

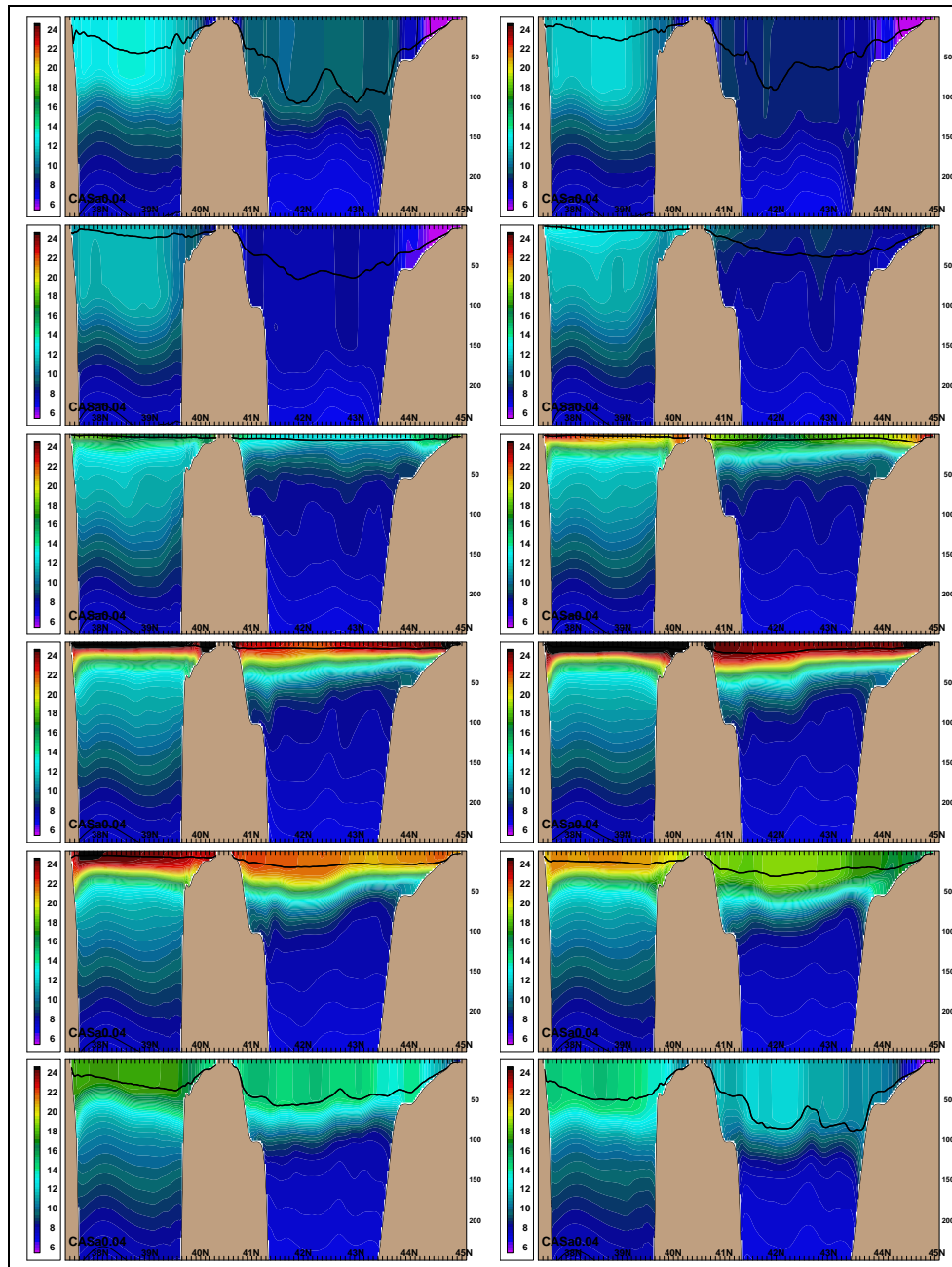


Figure 5.8: Model derived monthly mean temperature at $50^{\circ}E$ from January through December.

compared to the MCS, resulting in a clear latitudinal gradient of temperature, extending deeper to the differing thermocline depths in the two basins, with higher temperatures in the the SCS. By the end of the spring, stratification begins to develop and the Sea is strongly stratified in summer except in the shallow NCS.

A well-developed thermocline generally persists throughout the summer when the mixed layer depth typically decreases to about 15 m. As the stratification develops in either the MCS and the SCS basins the the level of the thermocline becomes distinctly different between the basins. the MCS both has a larger density and a stronger stratification at thermocline level in the MCS as compared to the SCS. While the 11 °C temperature is occurs at about 50 m depth in MCS in July, it soccurs at a depth of about 130 m in the SCS. .

The most distinguishing feature of the model derived SST is the clear inertial frequency oscillations shown in Animation 1 provided in addendum. This movie shows all the belligerent features of the Caspian Sea circulation acting in harmony: upwelling along the eastern coast, the intrusion of warm water from the SCS to the MCS along the eastern coast, and cold water along the western coast of the MCS were succesfully reproduced by the model.

Besides local influence on temperature, there are also large scale climatic influences on SST variability which is also important. These effects of large scale climate patterns on the SST variability are discussed in the Large scale control chapter of this thesis.

5.3 Mesoscale Circulations

It is important to characterize the nature of the Caspian Sea mesoscale variability to determine its role in exchange processes and general circulation. The Caspian Sea general circulation is dominated by large cyclonic anticyclonic gyres over the middle and southern basins, and by wind-driven and buoyancy-driven coastal boundary currents. These circulation elements form

jets and fronts that become unstable and shed eddies. The eddies may play a pre-conditioning role in wintertime deep convection. The wind-driven and buoyancy-driven coastal currents and undercurrents are important transport mechanisms, as well as probable sources of mesoscale variability. (e.g. Rachev and Stanev 1997 for the case in Black Sea)

Differently from the monthly mean circulation pattern, the snapshots of surface variables like SST, SSH and SSS are dominated by eddies and give quite different view of the circulation pattern. While mean fields are dominated by the anticyclone in the MCS and the anticyclone/cyclone pair in the MCS connected through various coastal jets, the snapshots are dominated by several eddies, with scales on the order of the 30-100 km. The movie of the circulation (Animation 2 in addendum) reveals numerous small and medium scale eddies generated/dissipated over the upwelling region, along the coastal boundaries and in dense water formation sites.

Figure 5.9 shows model eddy kinetic energy (EKE) at the first level of the model. In January, EKE is concentrated in the vicinity of the eastern coast and the northern continental slope which are believed to be the main sites where dense waters form. Compared to the SCS, the MCS is more active and EKE has its maximum value in the shallow NCS. Eddy kinetic energy in the Caspian Sea has pronounced seasonal cycle. EKE reaches a maximum during the summer season due to increased energy conversions of the stratified regime, and minimum levels of EKE are found during winter and spring when the water column is more uniform in the deep mixed layer. While maximum EKE is observed along the eastern and western coasts of the MCS, no significant levels of EKE can be observed in the southern Caspian Sea. However, in summer high values of EKE are also observed in the SCS where cyclonic/anticyclonic paired gyres are located.

Figure 5.10 shows the eddy kinetic energy along the $50^{\circ}E$ transect in January and August. The most distinguishing feature of this figure is the high level of EKE in the MCS as compared to the SCS, and the significant increases

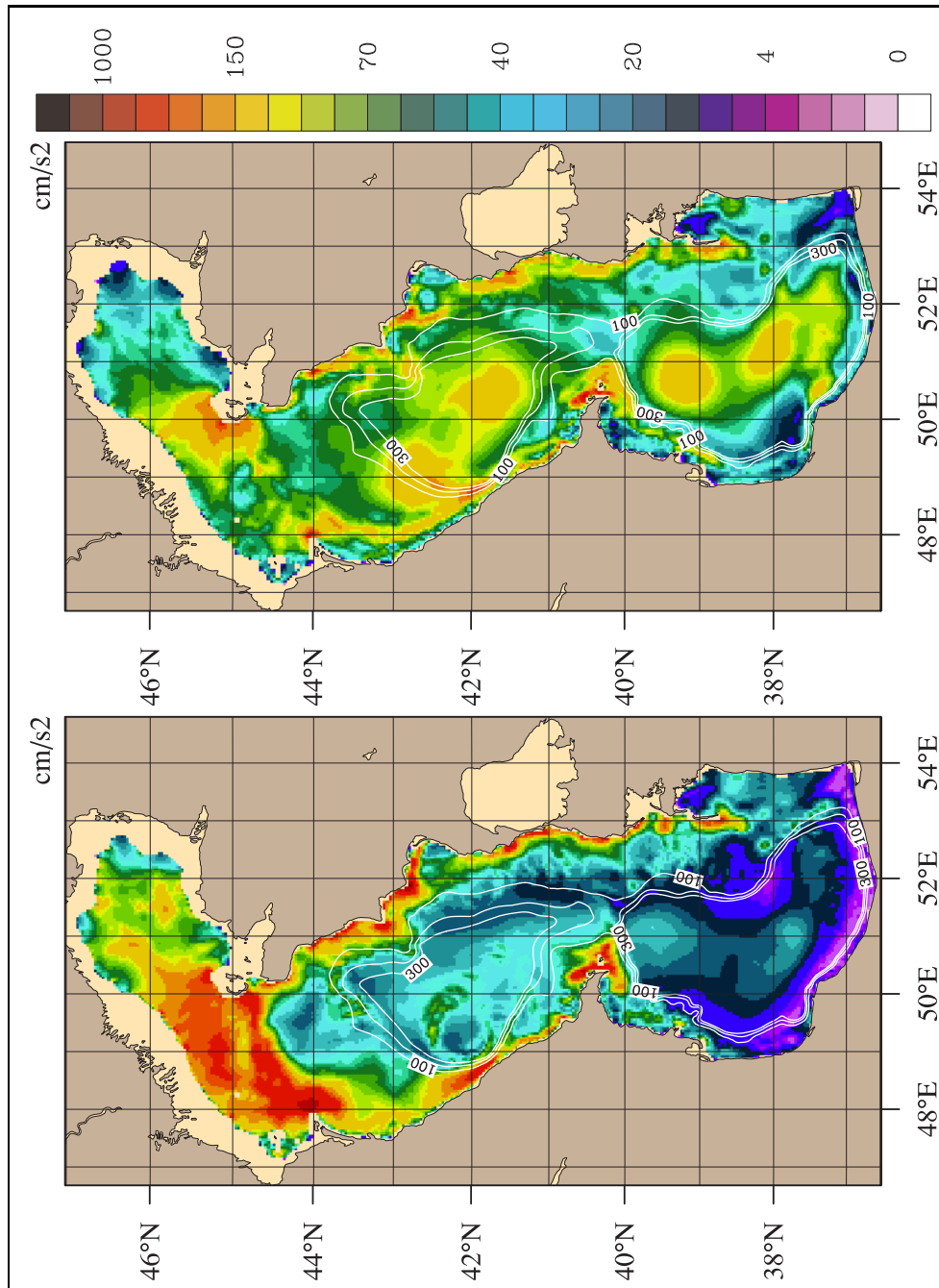


Figure 5.9: Model derived eddy kinetic energy (cm^2/s^2) map at first model level during (a) January and (b) August. The white contours are the bathymetric contours from 100 m to 300 m with 100 m interval.

of EKE in the surface layers in the summer season associated with developing stratification. In winter, high EKE regions occur exactly in areas where dense water is formed. In January there is almost no eddy kinetic energy in the southern basin indicating the extremely stable nature of the circulation in the SCS.

5.3.1 Mesoscale Features in the Northern and Middle Caspian Sea

Figure 5.11 shows currents averaged over depth interval of 0-30 m in the MCS in July. An outstanding feature of the July circulation is the southward/southwestward current along the north-eastern part, near the eastern coast of the MCS. This coastal jet current starts forming in June. The currents increase in intensity in July and continue to intensify in August (ref to earlier Figure!!). This flow completely disappears in winter, replaced by a northward current in the same area associated with the basin cyclonic circulation. This coastal jet carries the fresher, and as it will be shown below, also high chlorophyll water of the NCS towards the MCS along its eastern coast.

The headland, just north of the $43^{\circ}N$ on the eastern coast, is the place where the flow separates from the coast and also divides into two branches: while one branch turns to the north and follows the 100-300 m depth topographic slope, the other flows west towards the interior of the sea. Later, in September, the branch that flows into the interior of the sea increases in intensity and pumps relatively fresh water originating from the coastal part of the NCS into the central part of the MCS.

Figure 5.12 shows the model derived Sea Surface Salinity (SSS) for the model days 210, 212, 213, 214, 215, 221. Above mentioned coastal jet is also present in this figure, identified with less saline water trapped near the eastern coast of the MCS. The current carries the fresher and colder water of the NCS southwestwards to the interior of the MCS. Another distinguishing feature detected from SSS field is the mushroom like pattern present along

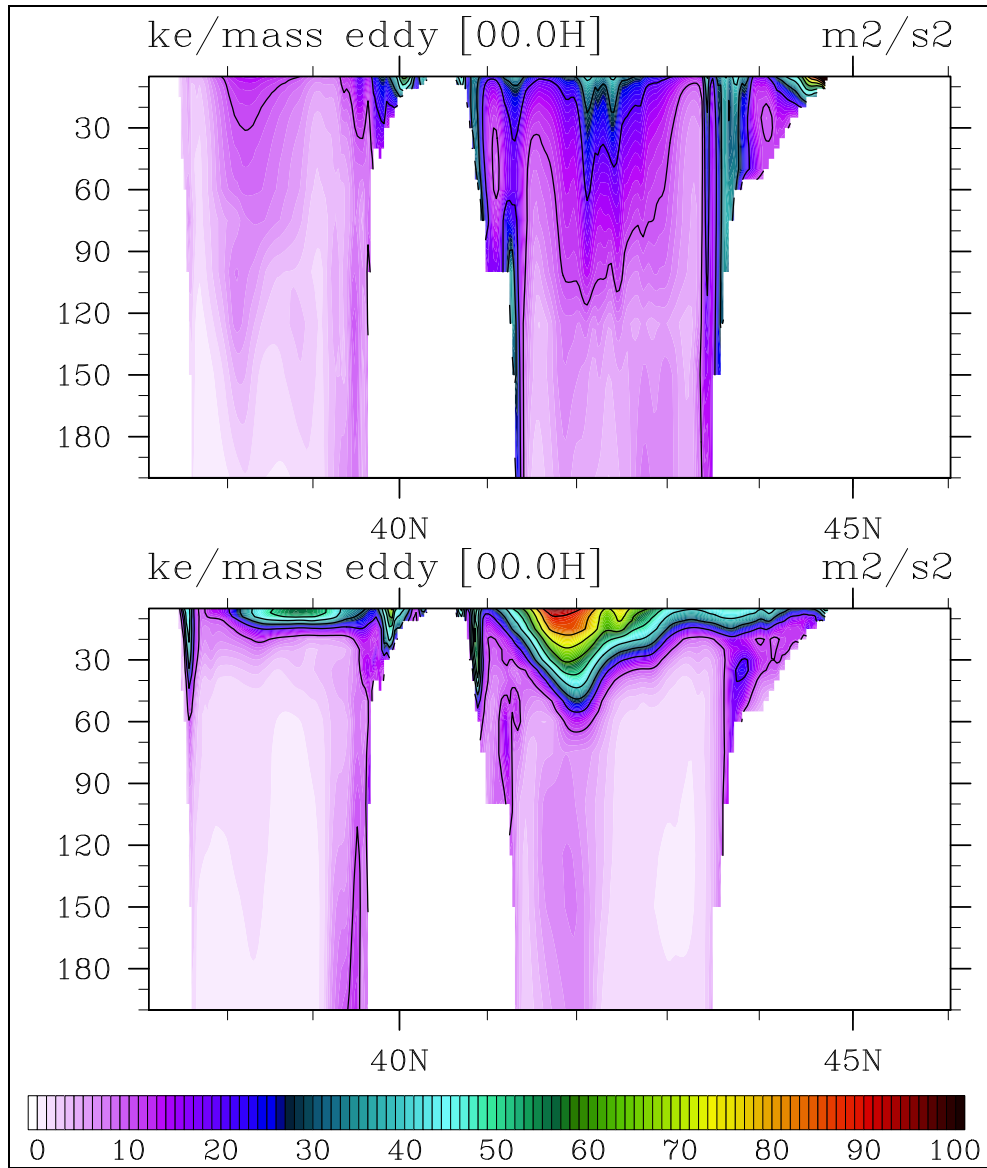


Figure 5.10: Eddy Kinetic energy (m^2/s^2) along the $50^\circ E$ transect in January and August

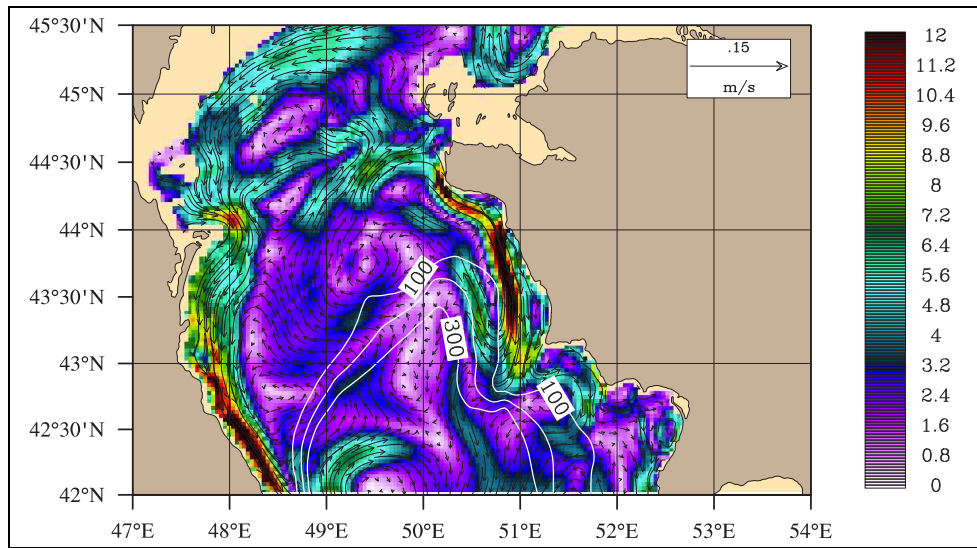


Figure 5.11: Model derived current in July over the MCS. The southward flow along the north-eastern coast of the MCS is evident in this figure.

the western coast of the Sea between $42^{\circ}N$ and $43^{\circ}N$ latitude. This filament is related with the anticyclonic cell exist here. The western branch of the anticyclonic cell pumps the coastal waters of the MCS to the interior of the Sea.

Different than above mechanism there is another filament which is evident in Figure 5.12. The reason for that mushroom like pattern is the meeting of northward flows with southward flows along the western coast near the $42^{\circ}N$. Figure 5.12 shows the chlorophyll concentration and model derived SSS. In these two figures, It is evident that

Some mesoscale structure of the Caspian Sea can also be deduced from the satellite measured chlorophyll concentration. Circulation features of the Caspian Sea was investigated by analysing the chlorophyll concentration. Phytoplankton is both a passive tracer transported by water circulation and an active biomass growing under favorable conditions (light, nutrients, etc.). These two processes should be consired when interpreting the circulation characteristics inferred from the chlorophyll maps. For the circulation patterns disscussed here, it is assumed that biology is controlled by the circulation patterns.

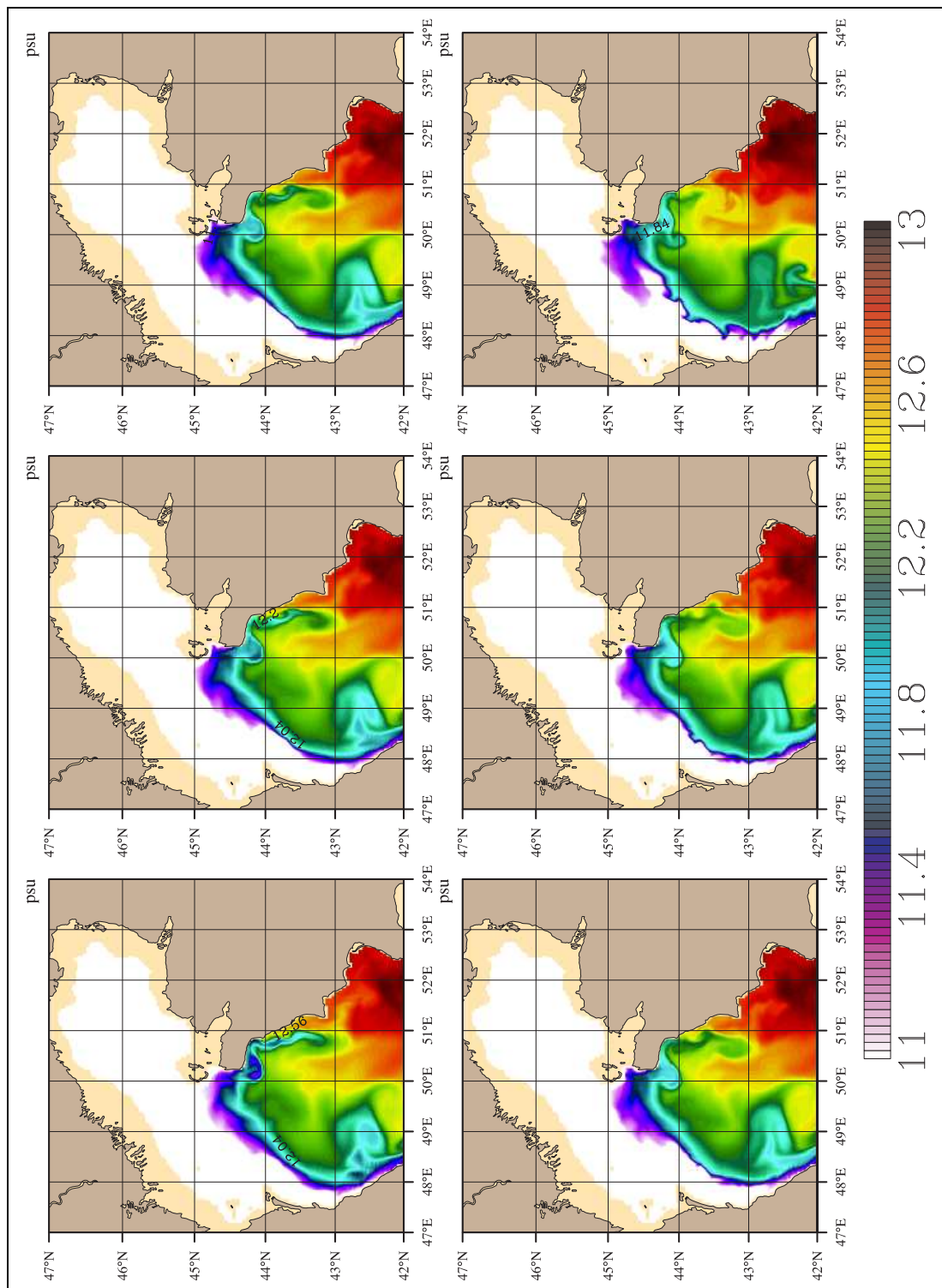


Figure 5.12: Sea Surface Salinity (SSS) for a series of model days 210, 212, 213, 214, 215, 221.

Analysis of chlorophyll data show that the existence of southward flow along the western coast of the Caspian Sea. In July and August, there is relatively high chlorophyll concentration trapped very near the coast with sometimes blocked near the $42^{\circ}N$ and do not penetrate to the south. However, beginning with the September the high chlorophyll along the western coast of the Sea become more thicker and cover the whole coast.

The southward coastal jet over the north-eastern part of the MCS in July to October period was also evident in chlorophyll data. Figure 5.13 provide a sequence of chlorophyll concentration during July-August 2004. Beginning with the 27 July 2004, Figure 5.13 a, there seems to be movement of water toward to the south. The relatively high chlorophyll concentration in the interior of the MCS is the results of pumping of high chlorophyll data by this mechanism in the period 1-17 July 2004 (not shown). After two days, 29 July 2004, high chlorophyll concentration is evident a little bit south, the intrusion of high chlorophyll is continue in the next day (30 July 2004). During the 1-2 August 2004 (Figure 5.13 d,e) the currents flows to the south and interior of the sea. Finally the jet detect in 8 August 2004.

Above mentioned southward current is also observed in other years. For example Figure 5.14 shows a series of chlorophyll maps during June-July 2005 period. The minor difference in the struture of the southward coastal current between this year and 2004 is that the current in 2005 is more close to the coast than 2004. Similar structures as explained for 2004 and 2005 years is also evident for other years. It can be concluded that this feature is a permanent structure of the general circulation of the Caspian Sea.

5.3.2 Mesoscale Features in the Southern Caspian Sea

Figure 5.15 shows six particular snapshots of daily circulation pattern of the SCS from January to June (at particular days 15, 45, 75, 105, 135, 165). Figure 5.15 a, describing the conditions during day 15 of the model day, reveals one big cyclonic gyre which is located southwestern part of the SCS. A small

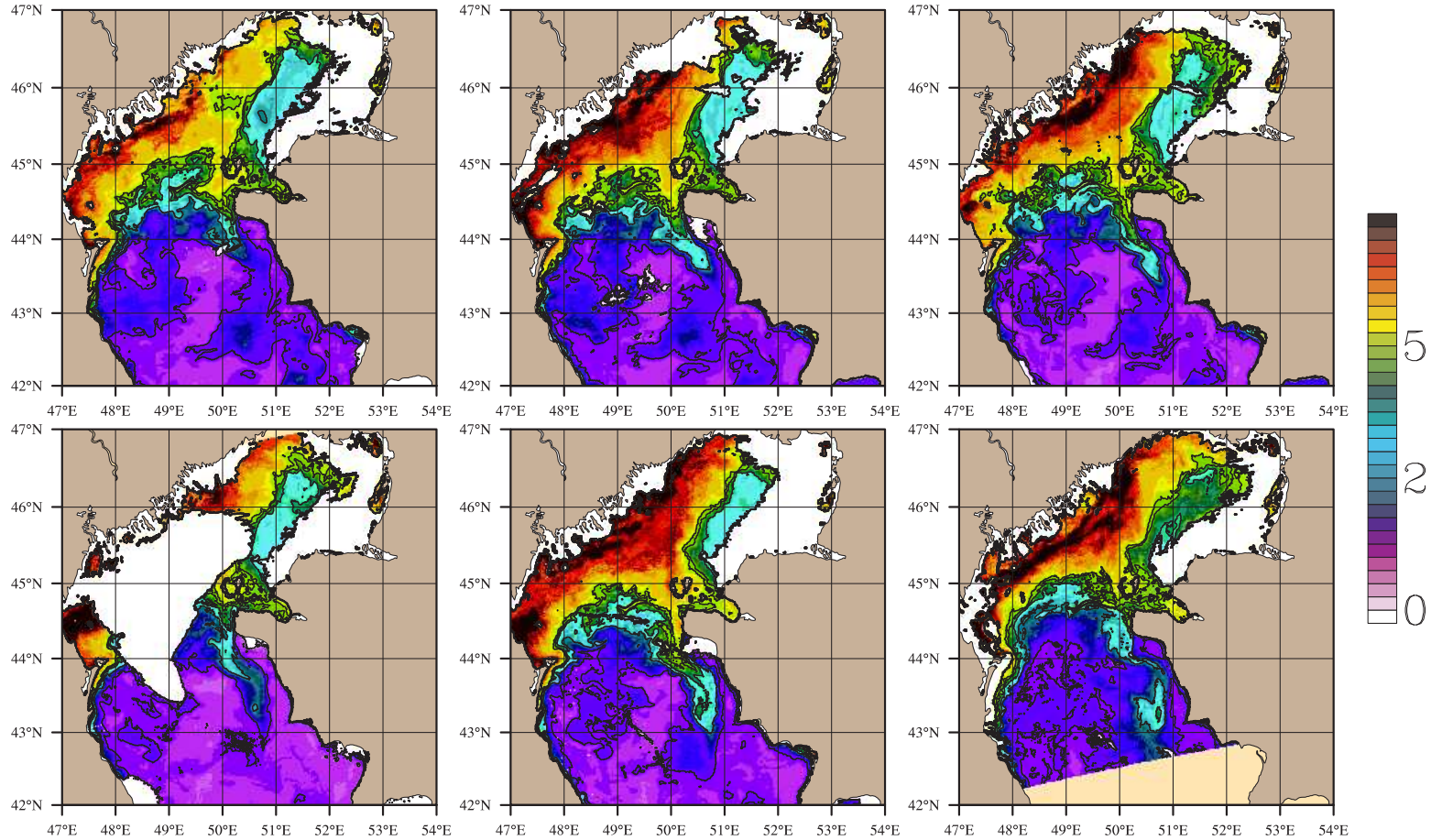


Figure 5.13: Sequence of chlorophyll concentration (in mgm^{-3}) on 27,29,30 July and 1,2,8 August of the year 2004. The chlorophyll concentration contours are plotted with different colours and intervals for a better visualization of structure.

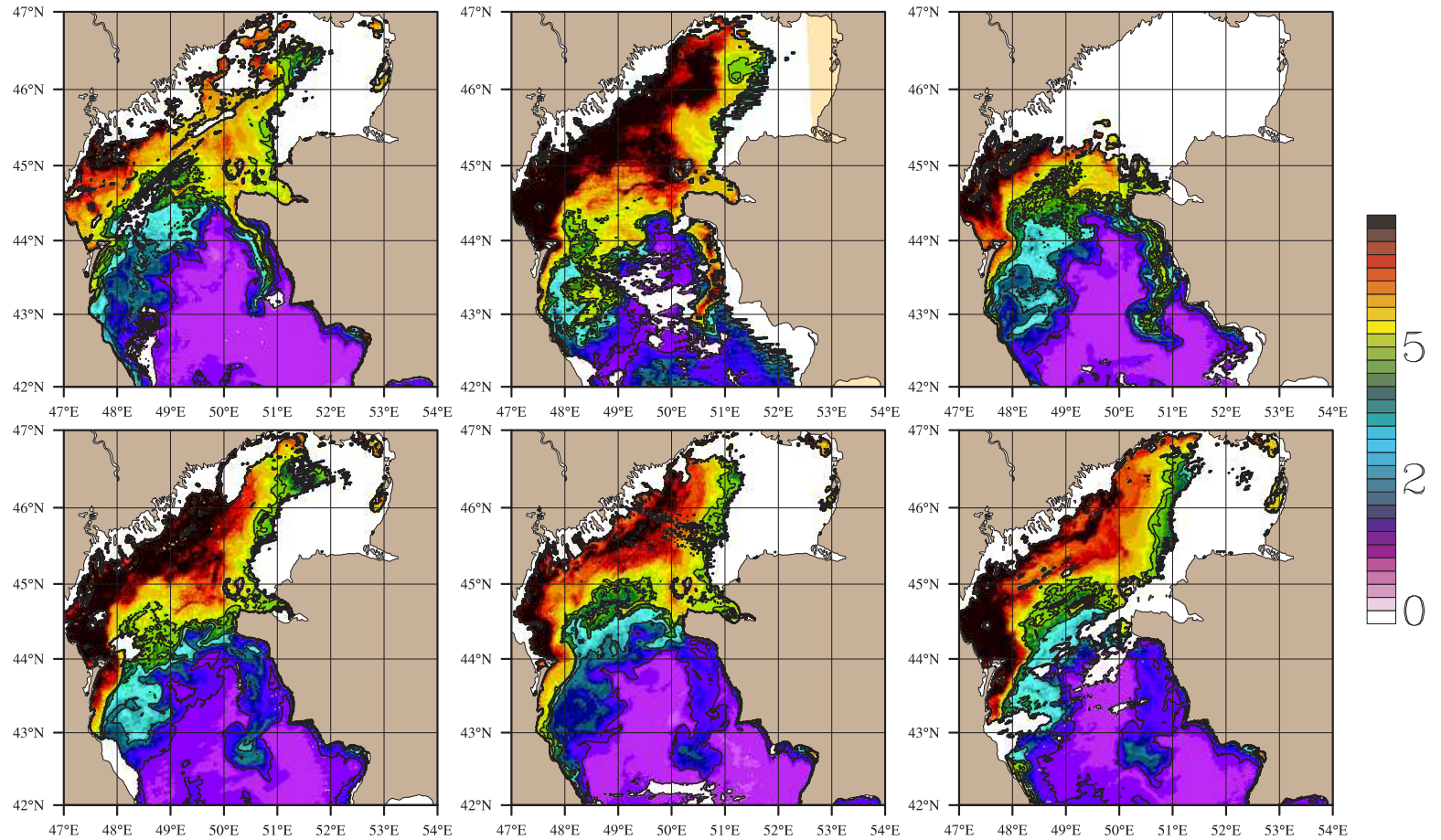


Figure 5.14: Sequence of chlorophyll concentration (in $mg\ m^{-3}$) 29 June and 1,4,7,8,9 July of the year 2005. The chlorophyll concentration contours are plotted with different colours and intervals for a better visualization of structure.

anticyclonic cell presents just above of this cyclonic gyre. There is a coastal jet along the southern coast of the SCS. Besides these organized structure, there are numerous number of small eddies located in the shallow eastern shelf of the basin, which is evident in day 45 Figure 5.15. The cyclone is the persistent structure of this basin in winter months. It is seen almost all the winter maps. There is always southward current along the each coast of the SCS. In June, a basin-wide cyclonic circulation begins to develop.

Figure 5.16 shows the snapshots of daily flow field from July to December at particular days (195, 225, 255, 285, 315, 345). The basin-wide cyclonic coastal jet which is already present in June becomes more intense in July shown in Figure 5.16 a. This coastal jet appears to follow the 100-300 m bathymery contour. This jet seems to be similar to the Rim current in the Black Sea. While this strong Rim current in the SCS blocks the exchange of properties between the coastal zone and inner sea while jet like instabilities, mesoscale eddies, filament mushroom-like structure play important role in shelf-slope water interactions. The blocking of water and material by this jet is easily seen in the chl-a concentration data detected by satellite. High chl-a concentration is observed along the south western and southernmost coast of the SCS without any intrusion to the interior of the Sea. The circulation map in day 225, Figure 5.16 b, reveals the similar pattern as day 195 but the magnitude of this current is more intense in this day. In Figure 5.16 b, a small anticyclonic vortex near the $51^{\circ}E$ also begins to form. It then grow gradually in day 255 by expanding toward the east. In this day the currents along the Iran coast is more stronger, this coastal current is also evident from drifter observations and successfully reproduced in the HYCOM Caspian Sea model. Figure 5.16 d shows the evolution of this anticyclone. In this figure, day 285, the anticyclone is more stronger. However, the strong coastal current along southernmost part disintegrates into smaller anticyclone and this anticyclone grows gradually in day 315. A jet is also present transporting the southeastern coastal waters of the Caspian Sea to the interior of the sea. This jet is also evident from the satellite

derived SST as a filaments associated with large offshore protrusion of the jet towards the interior of the SCS basin. This pumping mechanism exists until the end of December. The anticyclone near the $51^{\circ}E$ dissipates all together in day 345 as the circulation system begins to switch to its winter regime. The circulation in the SCS is more clearly defined and intense in summer than in winter. In winter, eddy activity is more pronounced mostly located boundary between the shelf water and slope water.

A series of chlorophyll data (18, 19, 20, 21, 22, 26 August of the year 2006) were shown in the Figure 5.17. This figure reveals important circulation features of the SCS. The coastal jet along the south western part of the basin is most easily detected feature of the circulation structure. This jet divided into cyclonic and anticyclonic gyres due to the structure of the coast or depending on the intensity of the coastal current. There seems to be a permanent anticyclonic gyre at $51^{\circ}E$ and cyclonic gyre just north-west of this anticyclone. The intensity and location of this gyres changes from day to day. Flow structure after the $51^{\circ}E$ determined by the intensity of the anticyclone and changes from year to year. When this anticyclone is weaker, the jet follows the southern coast and turns to north following the 100 m bathymetry contour. If this anticyclone become stronger the jet do not follow the coast.

Another important mesoscale activity occurs over the south-eastern part of the Caspian Sea. In this region, the wide continental shelf occupies the eastern coast with a shelf break depth of 100 m. The broad shelf terminates abruptly (the depth suddenly increases from 100 m to about 500 m) to the west. There are very important physical processes (cross-frontal exchange, eddies, shelfbreak fronts, etc.) take place at the shelfbreak which divides the shelf and slope water. These physical processes extensively studied by various authors at Middle Atlantic Bight off the east coast of the United States (Beardlesy et al., 1985, Gawarkiewicz 1991), the southern coast off Brazil (ref??).

In winter, there are numerous eddies associated with the shelf-slope water interactions. Figure 5.18 shows a snapshot of model derived SST at model day

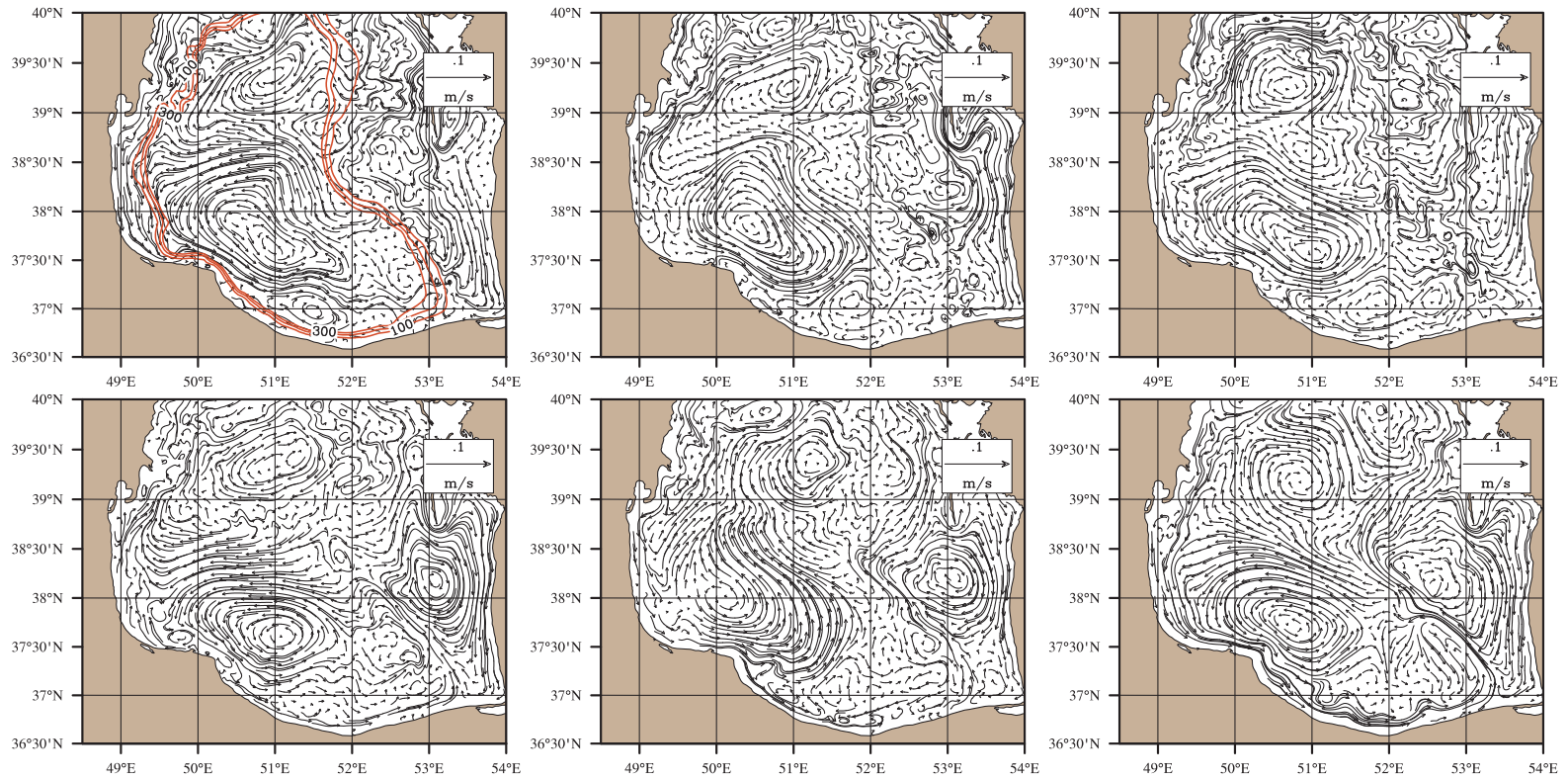


Figure 5.15: The evolution of the flow field in the SCS during (a) 15 (b) 45 (c) 75 (d) 105 (e) 135 (f) 165 days of the model days overlain on current magnitude

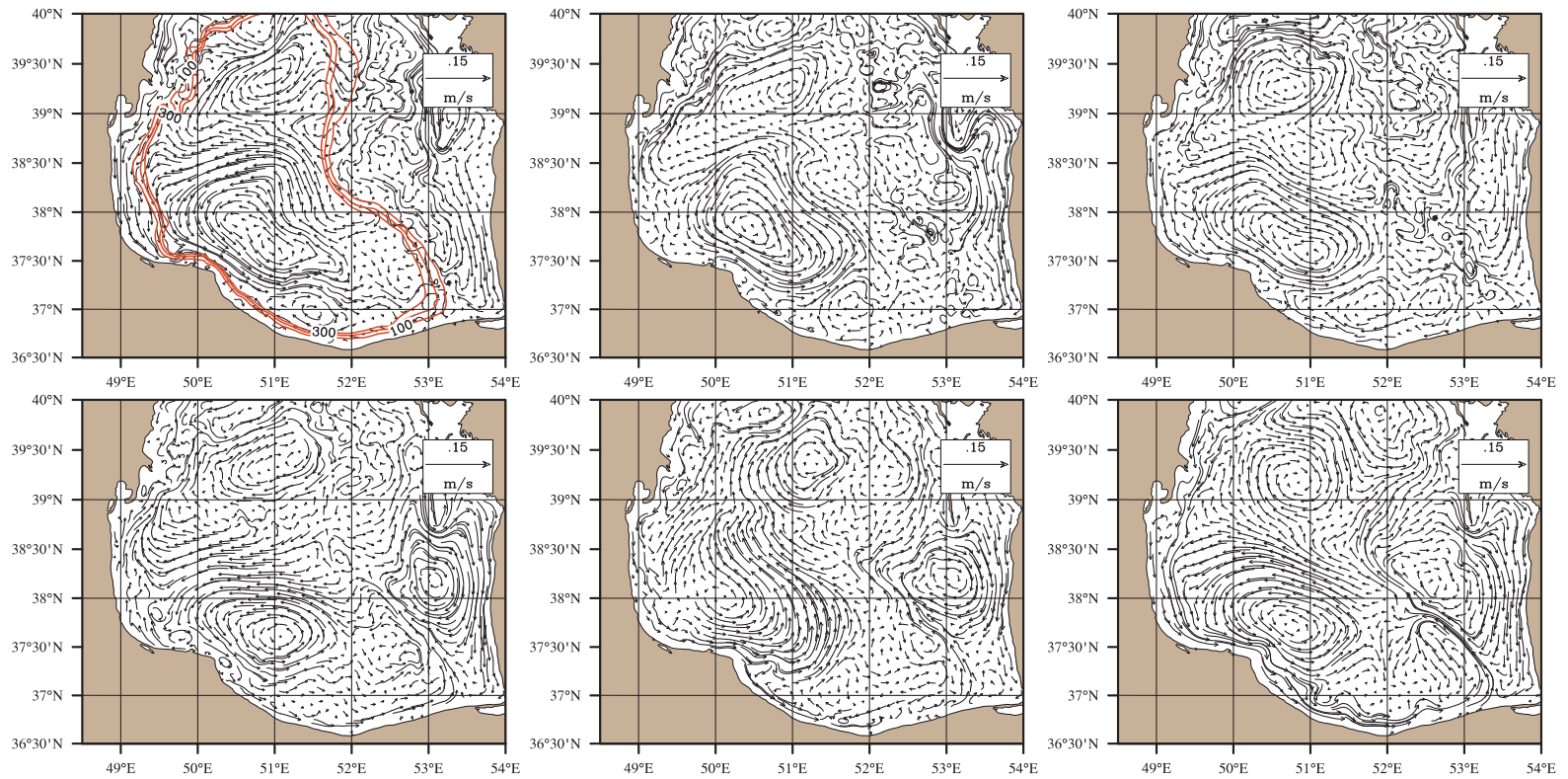


Figure 5.16: The evolution of the flow field in the SCS during (a) 195 (b) 225 (c) 255 (d) 285 (e) 315 (f) 345 days of the model days overlain on current magnitude

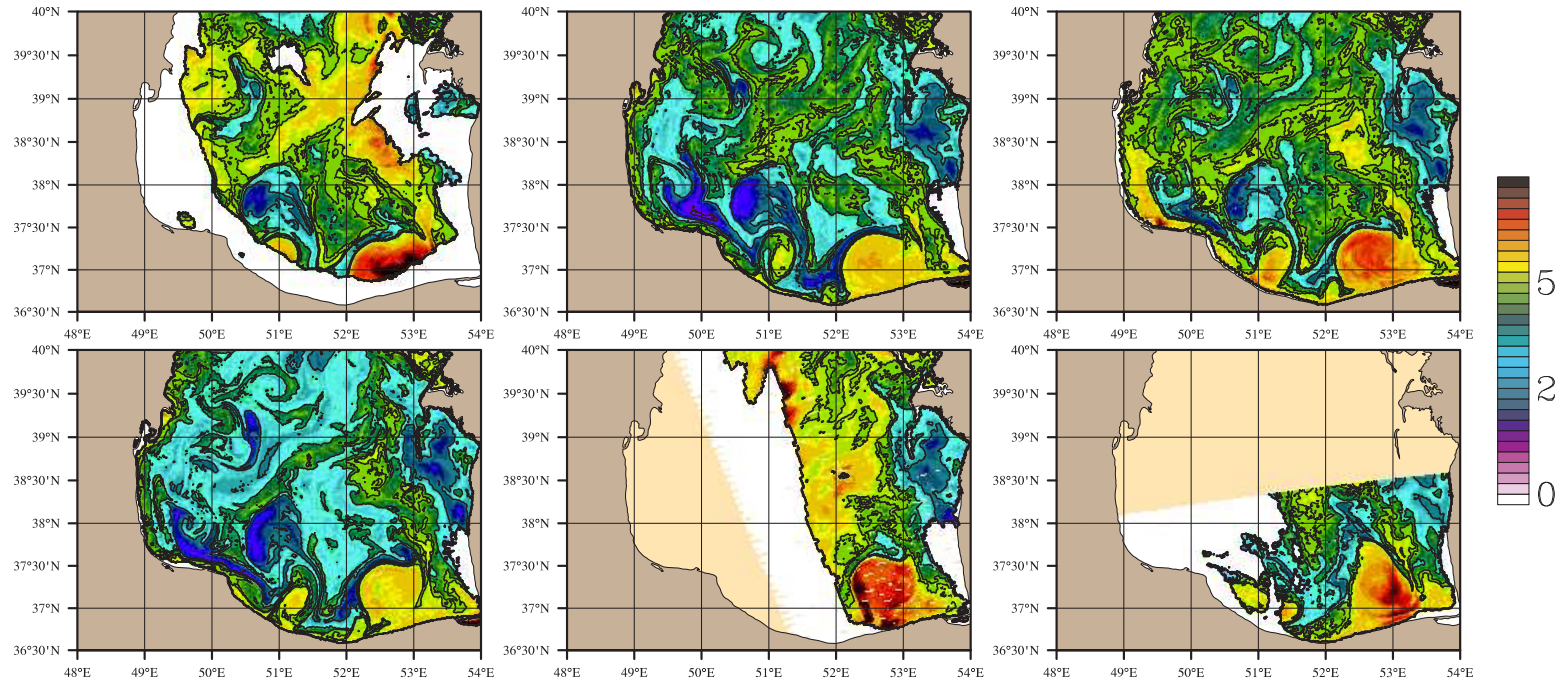


Figure 5.17: Sequence of chlorophyll concentration (in mgm^{-3}) on 18,19,20,21,22,26 August of the year 2006. The chlorophyll concentration contours are plotted with different colours and intervals for a better visualization of structure.

70. The eddies along the shelfbreak is clearly seen in this figure.

The south-eastern shallow corner of the South Caspian Sea is a suitable place to investigate the behaviour of the coastal flow due to topographic variations. In this region bathymetry seems to play important role in the structure of the coastal jet. There are numerical and modelling studies related with this subject. Sanson et al., 2005 studied by means of laboratory experiments and numerical simulations and describe the effect of topography on a barotropic coastal current. They concluded that when the flow goes from deep to shallow water, a part of or even the whole current might be forced to move along the contours of the topography, away from the coast. The situation in the SCS is similar to this study, the coastal flow come from the west (from deeper part) to shelf and move along the contours of the 100 m bathymetry. (Figure?? surface currents at day 222 and bathymetry)

Some information about the flow structure of the Caspian Sea can be also deduced from the deployed drifters in the Caspian Sea. Three drifters, two in the MCS and one in the SCS, were deployed in the Caspian Sea during beginning of November 2006, and they operated approximately three months providing the location, temperature and barometric pressure on their courses.

The most striking feature of the Caspian Sea dynamics based on the drifters are the inertial oscillation and strong variability of the currents. One of the drifters in the MCS was deployed at $41.8^{\circ}N, 50.2^{\circ}E$ and the other at the offshore of the Apsheron Peninsula. This two drifters shows cyclonic motion. First drifter, Figure 5.19 move northward and turn to west near 41.8 , and then flows southward as a coastal jet along the western coast of the MCS. After trapping the coast it moves faster and it reaches to the Apsheron peninsula in almost 10 days. The speed of the drifters along the western coast is nearly 20-25 cm/s. The drifter moves west and east in 6 days across the Apsheron sill and then move northward.

Other drifter which is shown in Figure 5.20, begin to move to north from the offshore of the Apsheron sill. This drifter also shows cyclonic circulation

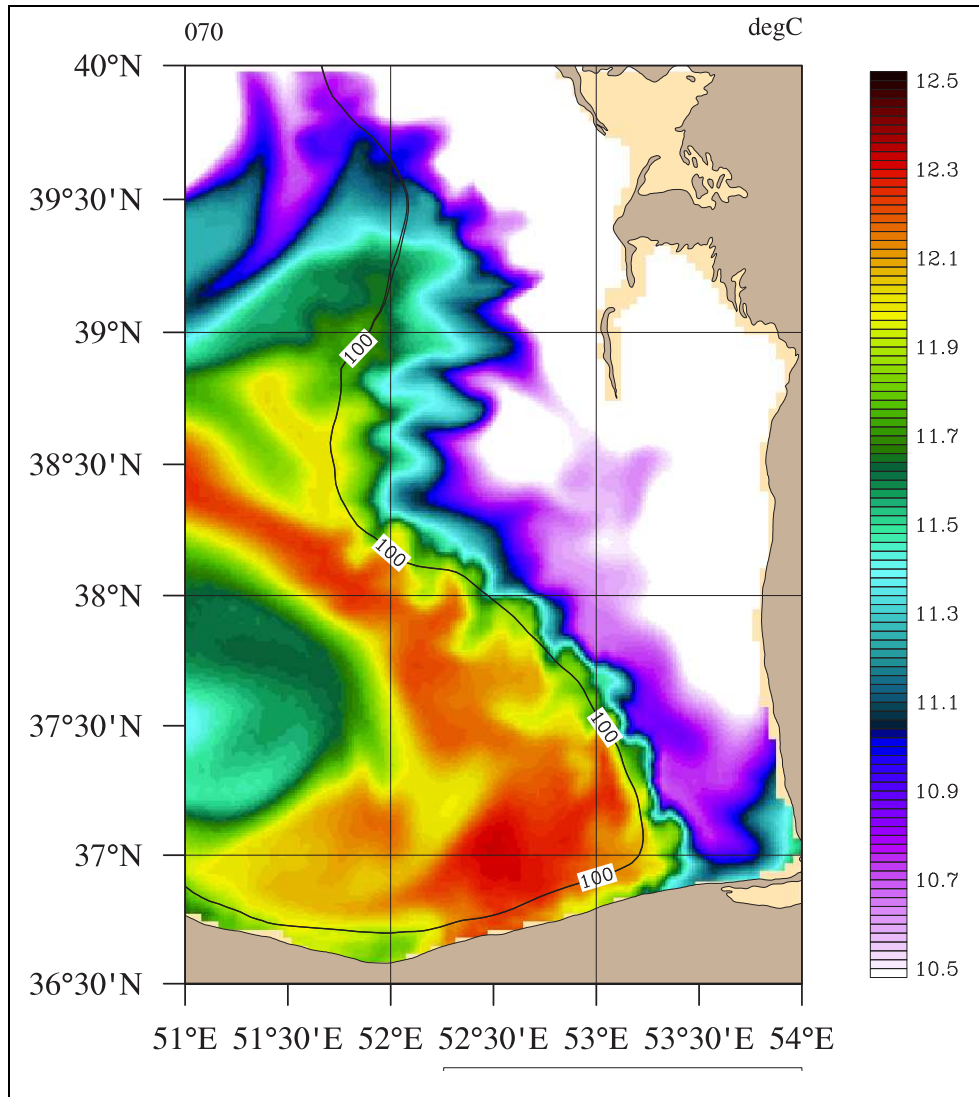


Figure 5.18: Snapshot of model derived SST ($^{\circ}C$) at model day of 70, the black line shows the 100 m bathymetry contour. The strong temperature gradient is evident at the shelfbreak separating the shelf water from the slope inner water. The unstable motions, meanders along the black line are also evident in this figure.

similar to the other drifter. In this two drifter, the inertial oscillation is evident.

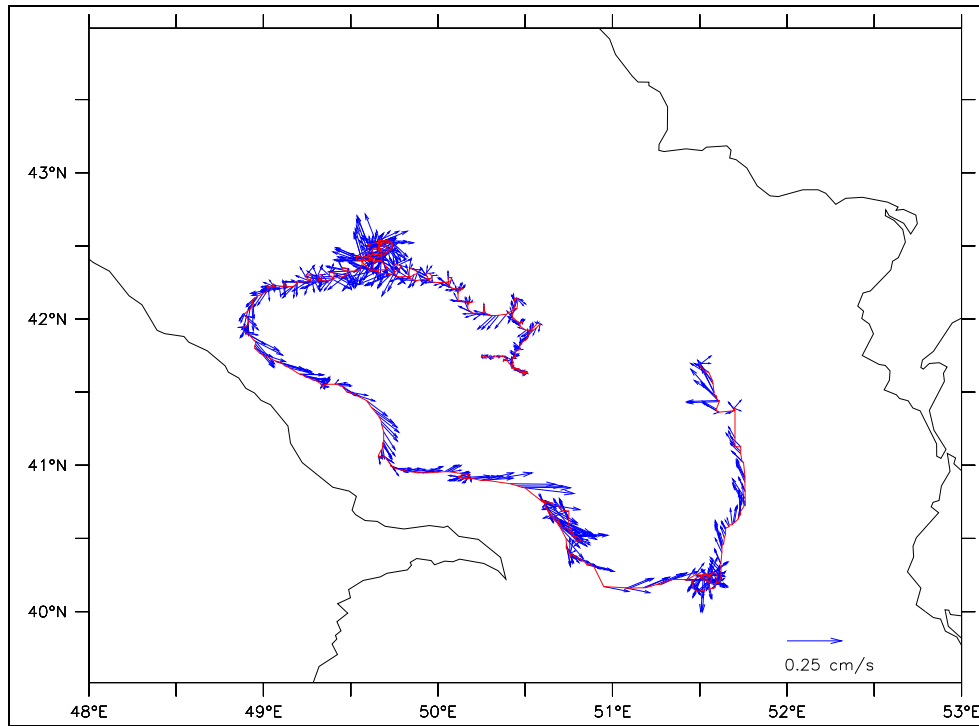


Figure 5.19: The trajectory arising from September 2007 deployment. Dot indicate the deployment site.

There is only one drifter in the SCS Figure 5.21, it moves southward after drifting west of its deployment place in 6 days, then turn to southward. The drifter flows into a anticyclonic cell. Interestingly, after reaching the end of the anticyclone, the drifter showed almost no displacement of 15 days at the southeastern coast of the basin, around $50.8^{\circ}E$, $37.8^{\circ}N$. The small currents and almost no displacement can be related with the calm wind regime which suspected to be one of the reasons of the cyanobacterial bloom in this basin. In contrast, when the drifter flows along the southern coast of the basin, it reaches maximum velocity like $35cm/s$. This coastal jet is also reproduced in the model. It seems that the wind is not a principal cause of formation of jet along the southern coast. The configuration of a coast, morphology of a bottom is more important than wind. Another distinguishing circulation feature detected

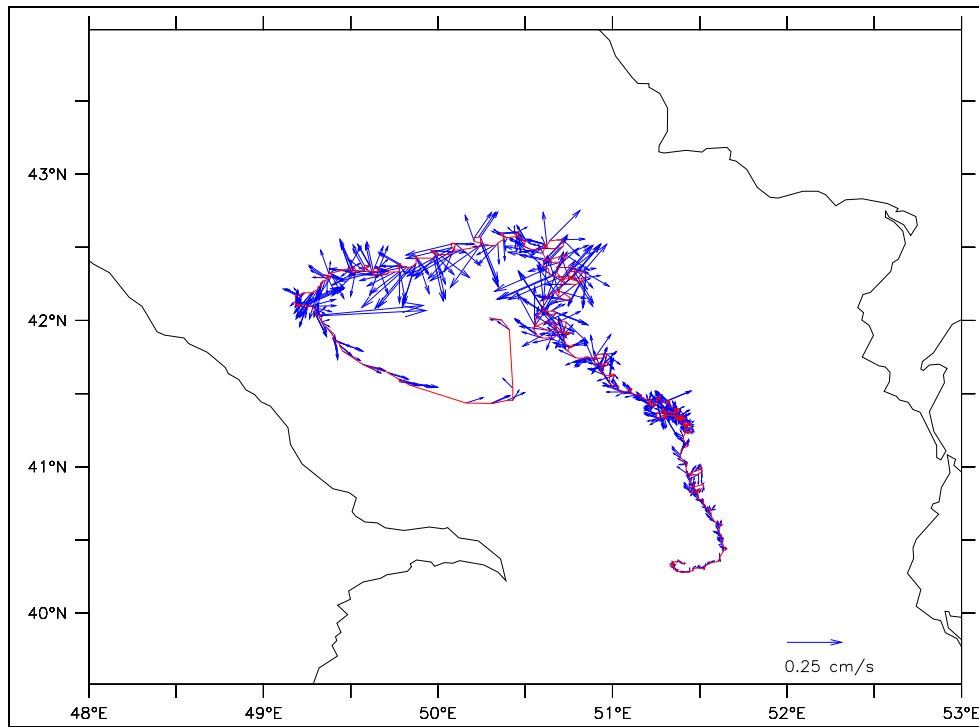


Figure 5.20: The trajectory arising from September 2007 deployment. Dot indicate the deployment site.

by drifters trajectories is the strong variation of current directions. Although the drifter passes the same location, at the southernmost of the anticyclonic gyre, two times with nearly one month interval. In the first pass (28 October) it turned to the north and flows into the anticyclonic gyre, but in second pass (23, November) it turned to the south and followed the southern coast as a coastal jet. This is the result of the strong variation in direction of surface currents. The drifter shows a strange movement at the eastern part of its path just below the $38^{\circ}N$, the direction of the drifter change abruptly to the south when it was moving to the north. It can be suspected that the reason of this strong turning is wind, however it is interesting that the drifter followed the same path which it has followed before returning. The topographic effect could play a possible role in this abrupt change in direction, while the drifter move along the shelfbreak and follow the topography as a coastal current, drifter changed direction at a place where there is a headland.

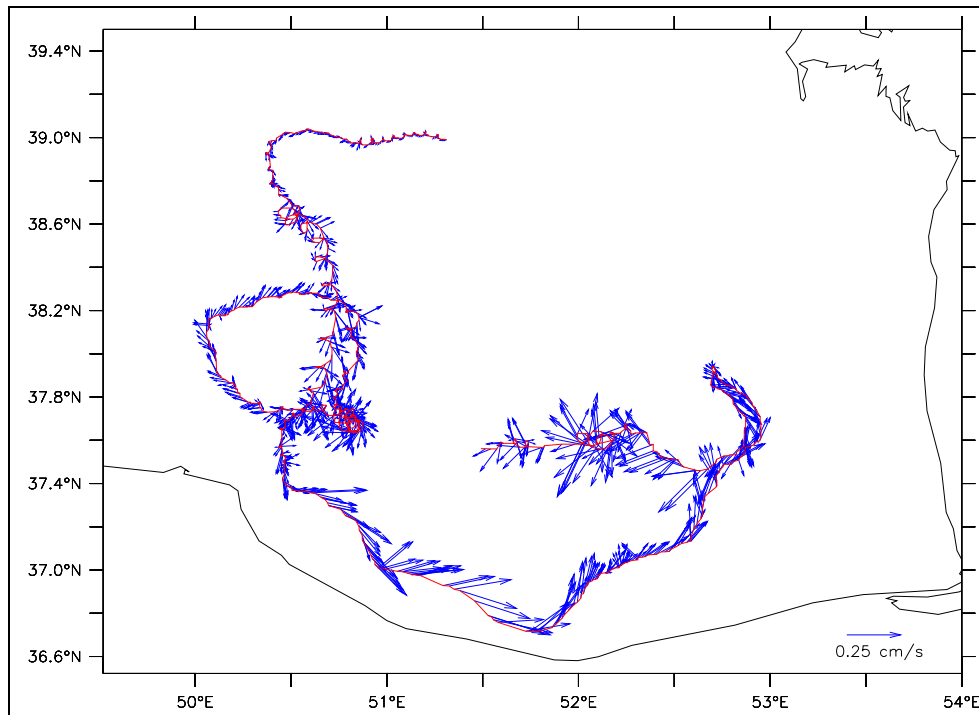


Figure 5.21: The trajectory arising from September 2007 deployment. Dot indicate the deployment site.

5.3.3 High Frequency Variability

In above sections, the annual, season and monthly mean characteristics of the Caspian Sea dynamics was investigated by using model, satellite and drifter results. In this section the high frequency variability of the Caspian Sea is investigated. HYCOM Caspian Sea model output was stored by 3 hour interval and the spectra of the current component was computed.

The current data near the coastal stations of the Caspian Sea were investigated by various authors (Kosarev and Tsiganov 1972, Bondarenko and Kosarev 1990). Based on the spectral analysis of the long-term observations, they have found that at most of the stations four energy maxima emerge at periods of several days and approximately 24, 17 and 12 hours. Although the exact values of such maxima at different stations are not the same. Typical synoptical changeability of the winds period has a variation of five days, the 24 hour maximum was probably due to warming and cooling of the sea. Iner-

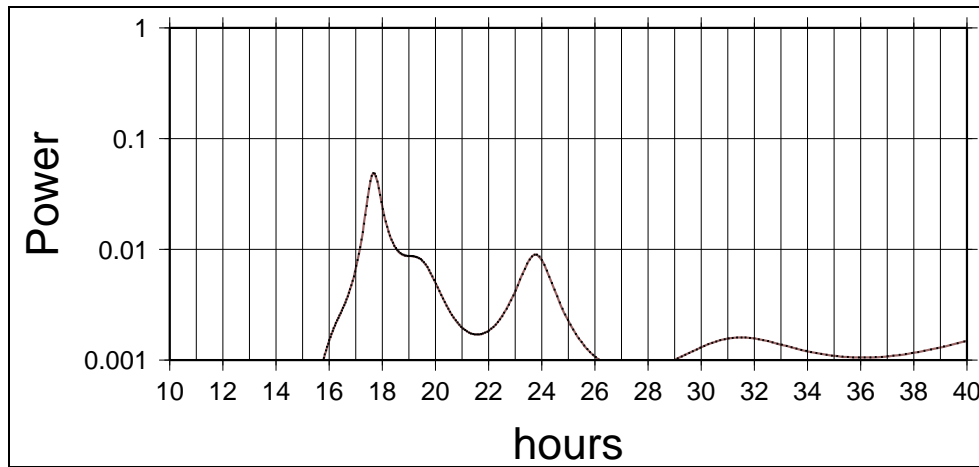


Figure 5.22: Spectra of u component of current at 5 m, at $52^{\circ}E$, $42^{\circ}N$, this point was chosen since there is an observational spectra near this location, offshore of the Apsheron peninsula.

tial fluctuations of the currents has the spectral density maximum for 17 hour period. The quasi inertial variation is about 19 hours, 12 hours is semi-diurnal tidal and nine hour corresponds to the seiche period.

Figure 5.22 shows the spectra of the model eastward velocity at the station $52^{\circ}E$, $42^{\circ}N$. The peak shown in the figure corresponds to the inertial fluctuations of the currents, approximately 17 hours. Other peak, just left of the main peak, has a period of 24 hour related with the daily variations. Although there are clear peaks as shown above, the spectrum covers the broad band of frequency.

5.4 Upwelling

Figure 5.23 shows snapshots of model SST at days 200, 215, 230, 245 and 260 of the model annual cycle, at the upwelling region along the eastern coast of the Caspian Sea. Mesoscale dynamic features such as cold filaments, single and mushroom shaped dipole eddies, squirts are often evident in the SST patterns throughout the whole model year. The upwelling at times covers the entire eastern coast, while at other times (e.g. day 245), it almost vanishes. Irregularities along the coast, such as headlands and changes in orientation or slope of the complex topography affect the structure of the upwelled waters (Pringle, 2002). Filaments of upwelled cold water reach the interior of the basin following the generally westward Ekman drift currents at the surface. Upwelling features in the model simulated SST are consistent with satellite observations based on the Pathfinder SST data set reviewed in previous chapters.

The reason of coastal upwelling along the eastern coast of the Sea is the prevailing, upwelling-favorable, northerly wind in summer and autumn. Inhomogeneity of the wind field also effects the formation site and timing of the upwelled water. To detect the timing and spatial extent of the upwelling events, Howmoeller plots of temperature are generated in Figure 5.24. This figure plots the longitudinal variation of SST averaged over 40° - 42° N latitude (x axis) as a function of time(y axis). The upwelling in this figure is marked by the lower temperatures occuring near the eastern coast, at around 53° E longitude throughout the upwelling period from June to October. While the interior of the sea has an average temperature of $8 - 9^{\circ}\text{C}$ in winter, it warms up very rapidly in the spring and reaches a maximum temperature of $23 - 24^{\circ}\text{C}$ in August. The appearance of lower temperatures along western coast at around 49.5° N in winter is not related with upwellling; it is a result of the advection of cold surface water from the Northern Caspian Sea. Similar feautures are observed in the surface density (not shown). In the Caspian Sea, persistent northerly winds tilt the pycnocline so that it becomes shallower towards the east, finally reaching the surface and forming a density front (outcropping)

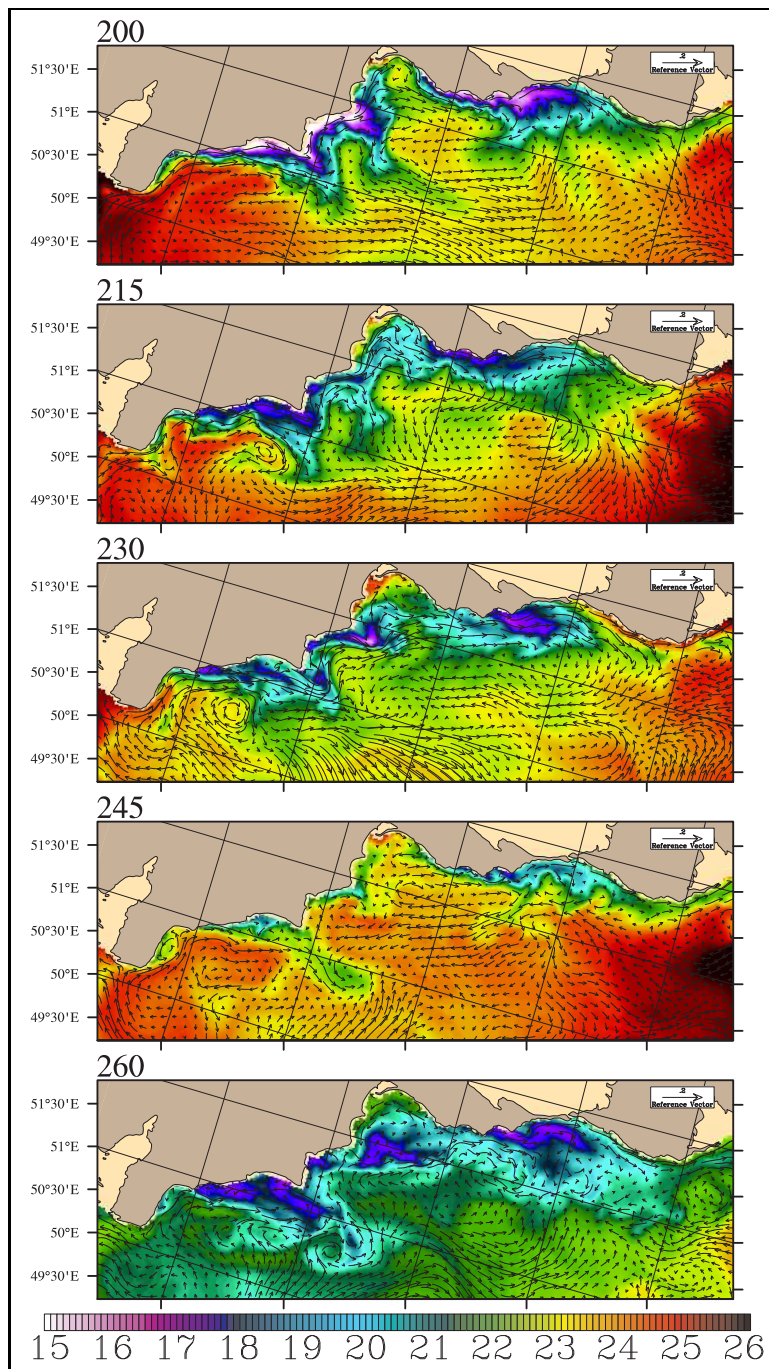


Figure 5.23: Snapshot of the model SST ($^{\circ}\text{C}$) of the 8th model year. The model days are shown at upper left side of the each figure.

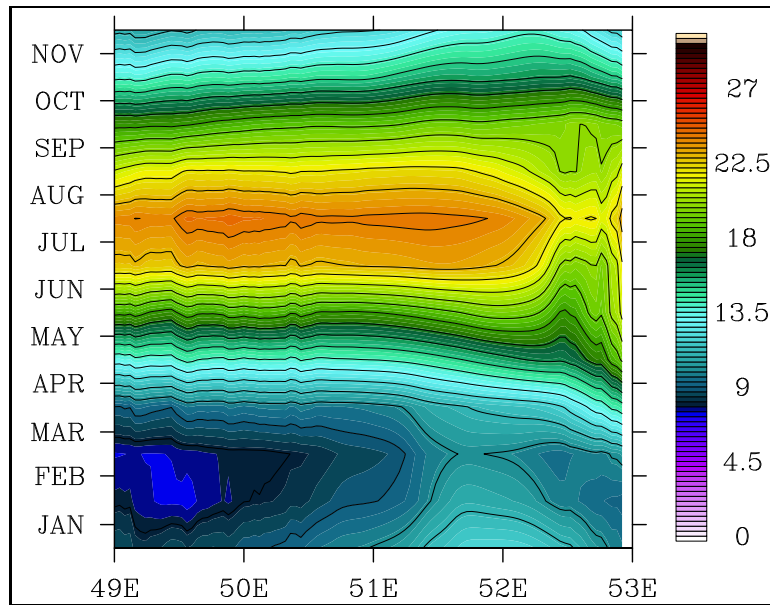


Figure 5.24: Howmoeller plots of sea surface temperature ($^{\circ}\text{C}$) averaged over $40^{\circ} - 42^{\circ}\text{N}$. X axis is the longitude and y axis is time.

near the eastern coast. This front is then displaced offshore under suitable wind conditions, resulting in "full upwelling" (Csanady 1977) which brings cold water from the depths of the basin to the surface.

Figure 5.25 shows north-south current distribution in the upwelling region averaged between $41^{\circ} - 44^{\circ}\text{N}$ latitude for the month of August. A southward jet with a maximum speed of 20 cm/s occurs in the shallow coastal region confined shoreward of the 30 m isobath along the eastern coast. Offshore from this shallow current, northward currents are observed, extending from the surface to a depth of 100 m , with relatively weak magnitude on the order of $2 - 3 \text{ cm/s}$. This subsurface coastal current is trapped by the topographic slope and masked at the surface by the predominant effects of the Ekman upwelling system currents driven by winds. This coastal circulation pattern (i.e the counter currents) has similarities to those observed in other upwelling systems such as the California current system in the western part of the America, and the Vietnam coastal jet in the South China Sea. The northward surface current transports warm water from the Southern Caspian Sea, detected as a vein of

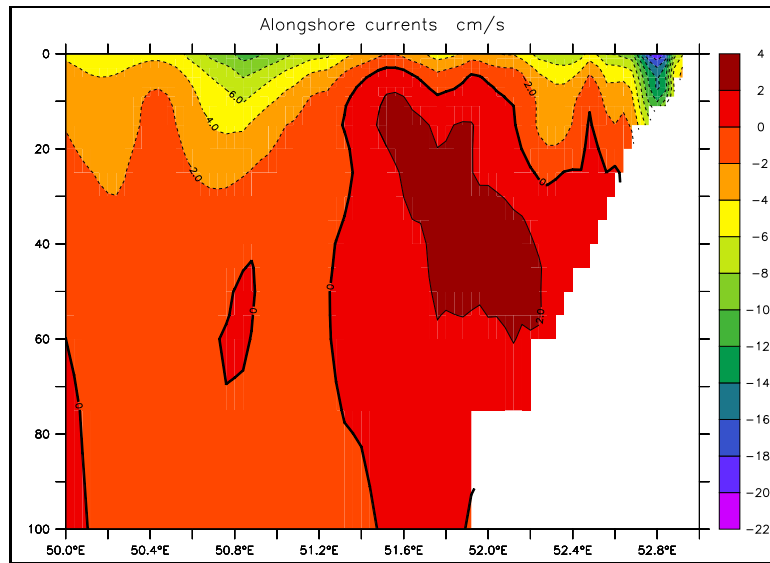


Figure 5.25: August alongshore currents (north-south) in the upwelling region averaged over 41° - 44° N. Positive (negative) means toward to north (south).

warm water in satellite images described in Chapter 2. Further offshore of the northward flowing jet, there are southward flowing surface currents once again near 50.8° E with a maximum speed of 10 cm/s, below this the subsurface currents are very weak and mostly north direction.

The southward coastal jet (alongshore flow parallel to the wind) is the result of the across-shore pressure gradient which is a typical feature of an upwelling system. The seasonal variation of the northward flow can be deduced from the daily v-velocity fields. Figure 5.26 shows the v-velocity, salinity and density evolution during the model annual cycle at the station 51° E, 43.4° N (inside the upwelling region, very near the coast). Beginning with the June, southward flows (negative and blue region after day 150) is observed and this flow carry less salty water of the NCS, as it is evident in the salinity time series. This southward current is very consistent and exists nearly 90 days until end of the August. The time of the decrease in the salinity and density coincide with the southward flowing jet. While the fresher northern water is transported by this southward current, the northward currents (positive red) transport the saltier water of the southern Caspian to the north.

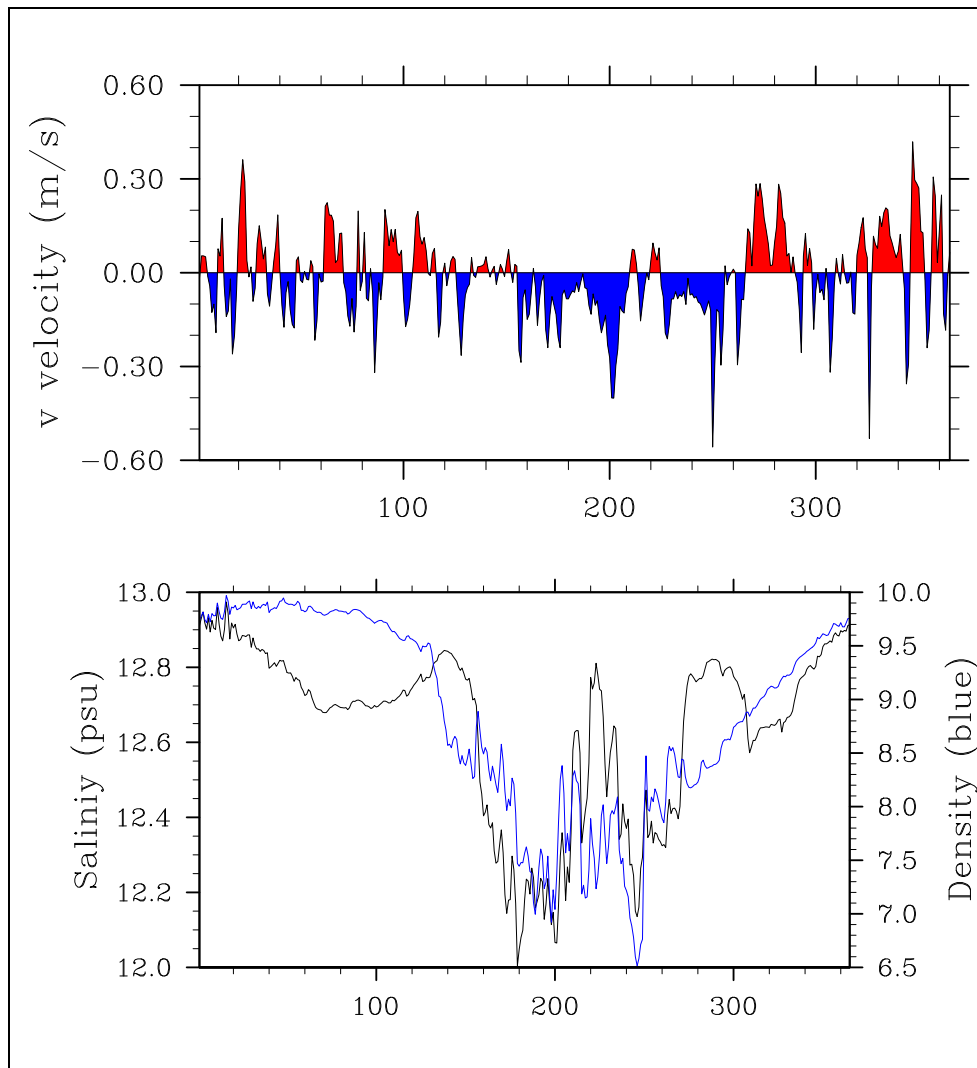


Figure 5.26: (a) V-velocity (m/s), (b) salinity (psu) and density evolution during the model annual cycle at 5 m at the station $51^{\circ}E$, $43.4^{\circ}N$. X axis is model annual cycle (366 days).

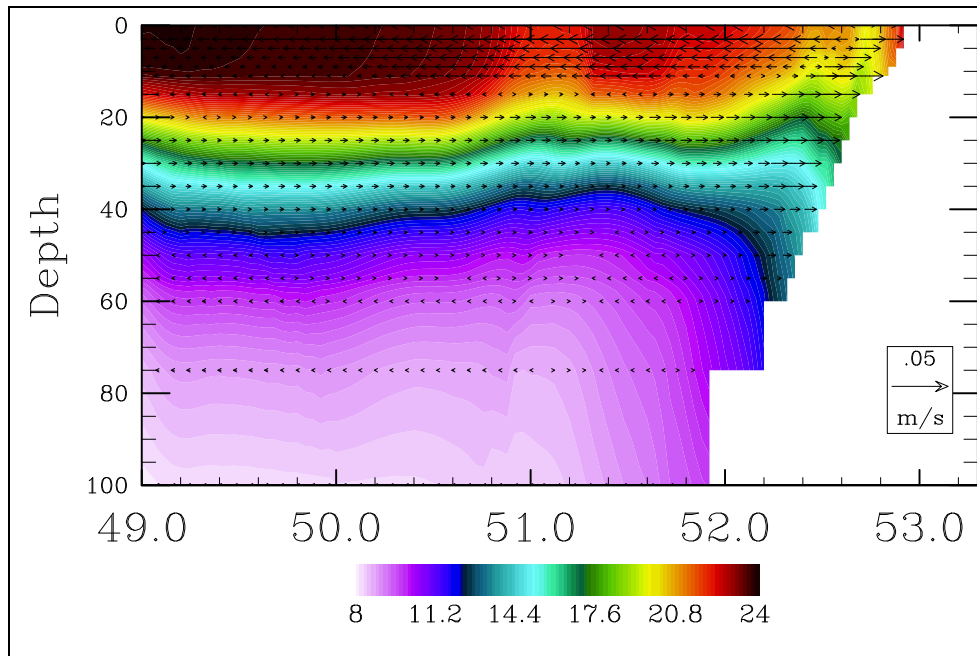


Figure 5.27: August temperature and cross-shore (east-west) currents in the upwelling region averaged over 41° - 44° N

In Figure 5.27, a cross-section of temperature and cross-shore currents for the month of August, averaged over 41° - 44° N latitude coinciding with the upwelling region, are presented. The signature of upwelling is clearly seen from temperature isolines rising to the surface near the coast. Offshore of the upwelling, westward (offshore) Ekman currents are observed in the shallow (20 m) surface boundary layer, with maximum speed of 3 cm/s. The westward transport of cold upwelled water very near the coast manifested by cold filaments in the satellite images creates offshore transport and mixing with the ambient waters. There is strong stratification in August, with temperature decreasing dramatically from 22°C at the surface to 9°C at 100 m depth.

Positive vertical velocities averaged over the whole depth in August (not shown) are present near the eastern coast of the MCS, showing the patches of upward motion feeding the upwelling system. The upwelling occurs very near the coast, however the circulation system, the shape of the coast and the bottom topography transport the cold upwelled waters away from the coast.

For example, the cold water can be found offshore of the headland located near the north of the $43^{\circ}N$, showing the effect of headland. The space and time variation of the upwelling along the eastern coast will be investigated in the "Float" section of this thesis.

Figure 5.28 shows the time and zonal dependence of wind-stress curl averaged over the upwelling region, based on the ECMWF ERA-40 dataset. In addition to direct Ekman upwelling effects resulting from the orientation of winds near a coast, wind stress curl can also contribute to upwelling or downwelling (Gill, 1982, O'Neill 2005). It is observed that the wind stress curl near the eastern coast has strong seasonal variability with a positive maxima near the coast in summer and negative values offshore. The wind stress curl diminishes in autumn. The timing and spatial extent of the upwelling seems to be associated with the stronger positive wind stress curl over the region of interest during the upwelling season. The positive wind stress curl reaches its maximum value in July, suggesting that the seasonal variation of upwelling is related to positive wind stress curl acting over the upwelling region in summer.

There are many factors affecting coastal upwelling, including heat fluxes, wind stress and currents. The affect of heat fluxes on upwelling properties have been investigated by conducting an additional experiment. In this experiment, all heat fluxes are switched off and the model is only forced by the wind stress. Interestingly there was no upwelling generated along the eastern coast of the Sea in this experiment, which strongly suggests that the heat fluxes were critically important for the upwelling.

5.5 Dense Water Formation

In this section, possible dense water formation sites and mechanisms in the Caspian Sea are investigated. Comparison with other observations in regional seas are also made.

Although the shallow Northern Caspian Sea is a good candidate for dense

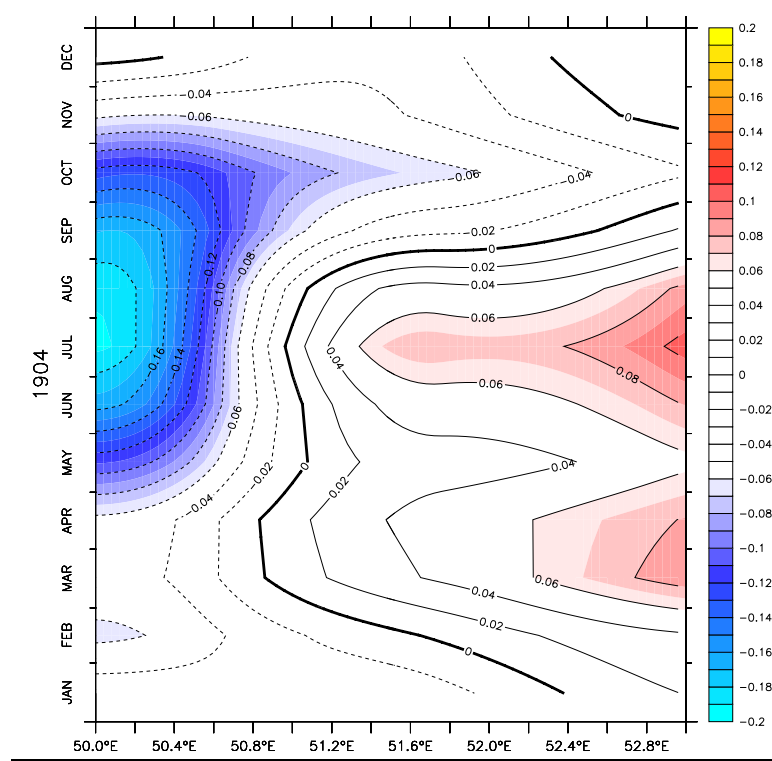


Figure 5.28: ECMWF wind-stress curl averaged over $41^{\circ} - 44^{\circ}\text{N}$

formation, examination of the density maps (not shown) from the climatological hydro data do not provide direct evidence for deep water formation in this shallow basin. On the other hand, climatological observations indicate a cold water mass with high density at around 44° latitude near the eastern coast. As mentioned in earlier sections, there is reason to expect dense water formation in this area, where currents coming from the south along the eastern coast can meet sea ice or cold water, and consequently sink to the deeper parts of the Middle Caspian Sea.

Similar dense water formation processes are known to take place in the Adriatic and Aegean Seas. Dense water formation in the northern basin of the Adriatic Sea was investigated by numerous authors. The combined effect of (1) surface heat fluxes and vertical mixing, (2) surface water fluxes (E-P) and water discharges, and (3) LIW inflow and advection towards the northern Adriatic are believed to be the major driving mechanisms of the dense water formation in this sea (Vilibic and Supic 2005). The dense water formed in the

northern basin flows southwards along the Italian continental shelf / slope at depths of 50-150m (Vilibic 2004, Vilibic and Supic 2005) and finally contributes to deep waters by being separated from the coast near the Gargano peninsula. Northern shallow shelf of the Aegean Sea is also known to be a dense water formation site, driven by wind and thermal fluxes.

Similar to the Adriatic and Aegean Sea, dense water is formed along the eastern coast of the MCS and the shallow north-eastern part of the basin. A vein of dense underflow is transported southward and reaches the interior of the MCS following local topography. It is characterized respectively by salinity and density ranges of 12.7-12.8 and 9.8-9.9. HYCOM Caspian Sea model allowed to identify the evolutionary characteristics of this underflow.

Figure 5.29 shows the density section at $50^{\circ}E$. The most distinguishing feature of the density section is the clear evidence of the dense water formation over the northern part of the MCS. The well mixed water in the shallow northern basin nearly at $44^{\circ}N$ attains a high value of density in January. One month later, this dense flow starts to sink to about 200m depth. The dense water originally generated at 40-50 m depth in the shelf zone continues to sink until April. In summer, a highly stratified water column is observed, and sinking motions cease. Interestingly, high salinity water is observed during the course of the year in the continental shelf region near the dense water formation site, but salinity alone does not account for sinking during the warmer part of the year in the presence of strong density stratification.

Another important feature inferred from this figure is the difference in density of the deep waters of the SCS and the MCS. The dense water of the SCS appears to derive from the MCS, where water of the same density generally occurs at shallower depths. The denser water formed in the MCS overflows the Apsheron sill, contributing to the deeper waters of the SCS.

To identify the dense water formation site and its temporal variability, monthly density sections along the $49^{\circ}E$, $49.5^{\circ}E$, $50^{\circ}E$ were plotted (not shown). From these maps it has become obvious that dense water forma-

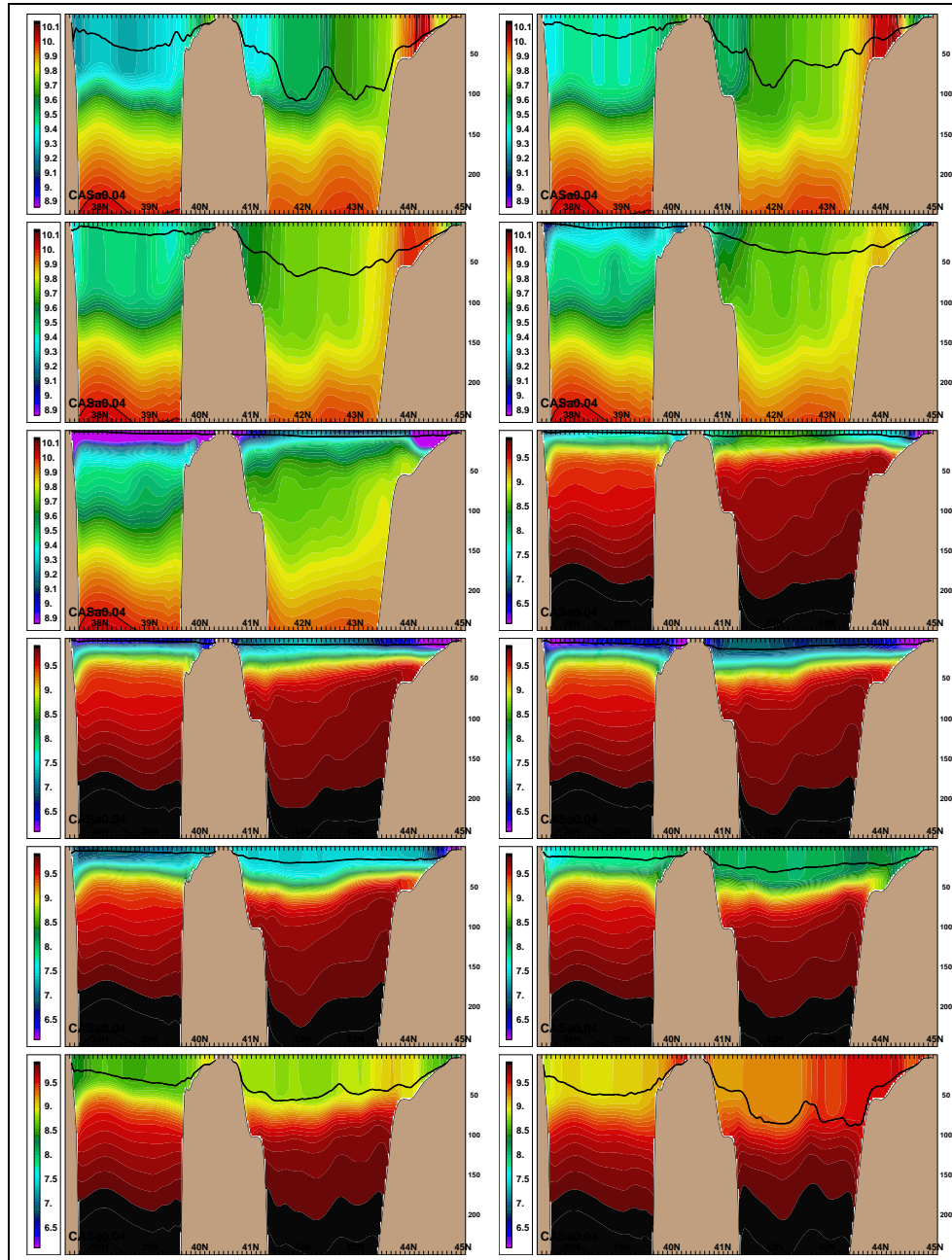


Figure 5.29: Model derived monthly density(σ) section at $50^{\circ}E$ from January through December.

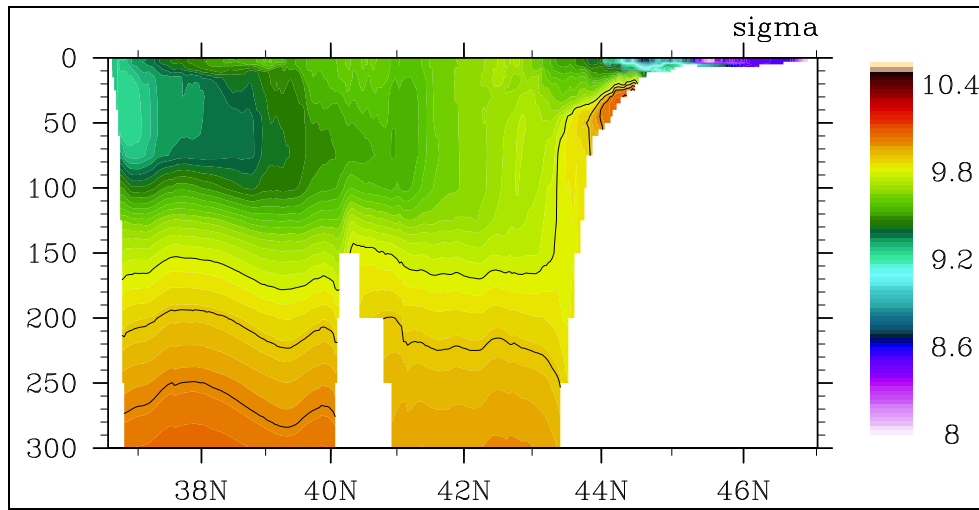


Figure 5.30: Density (sigma) section along the $49.5^{\circ}E$ in February.

tion site was localized between $49.5^{\circ}E$ and $50^{\circ}E$. Figure 5.30 shows one of these figures, the density section along the $49.5^{\circ}E$ in February, demonstrating the high density at 50 m depth over the shelf near $44.5^{\circ}N$ latitude. The generation of dense water and its sinking to a depth of 200 m along this section can be observed from Animation 3 provided in addendum.

As dense bottom currents flow down the continental slope and into the sea interior, they entrain mass from less dense ambient water, thus becoming more buoyant. The properties of the interior ocean water masses that result from dense water formation is partly determined by this entrainment. (Papadakis et al2003). Along the way to join the ocean interior, dense water overflows the bottom topography. Figure 5.31 shows the evolution of bottom layer density at the dense water formation site. Beginning with January, day 20, dense water is evident along the eastern coast of the sea, trapped towards the coast. The density of waters along the eastern coast gradually increase by day 40 and begin to move to the interior of the sea. From day 60 to day 80, dense water flows down the continental slope and starts to fill the interior of the sea. Beginning with April, the bottom density starts to decrease, signalling the end of dense water generation along the eastern coast.

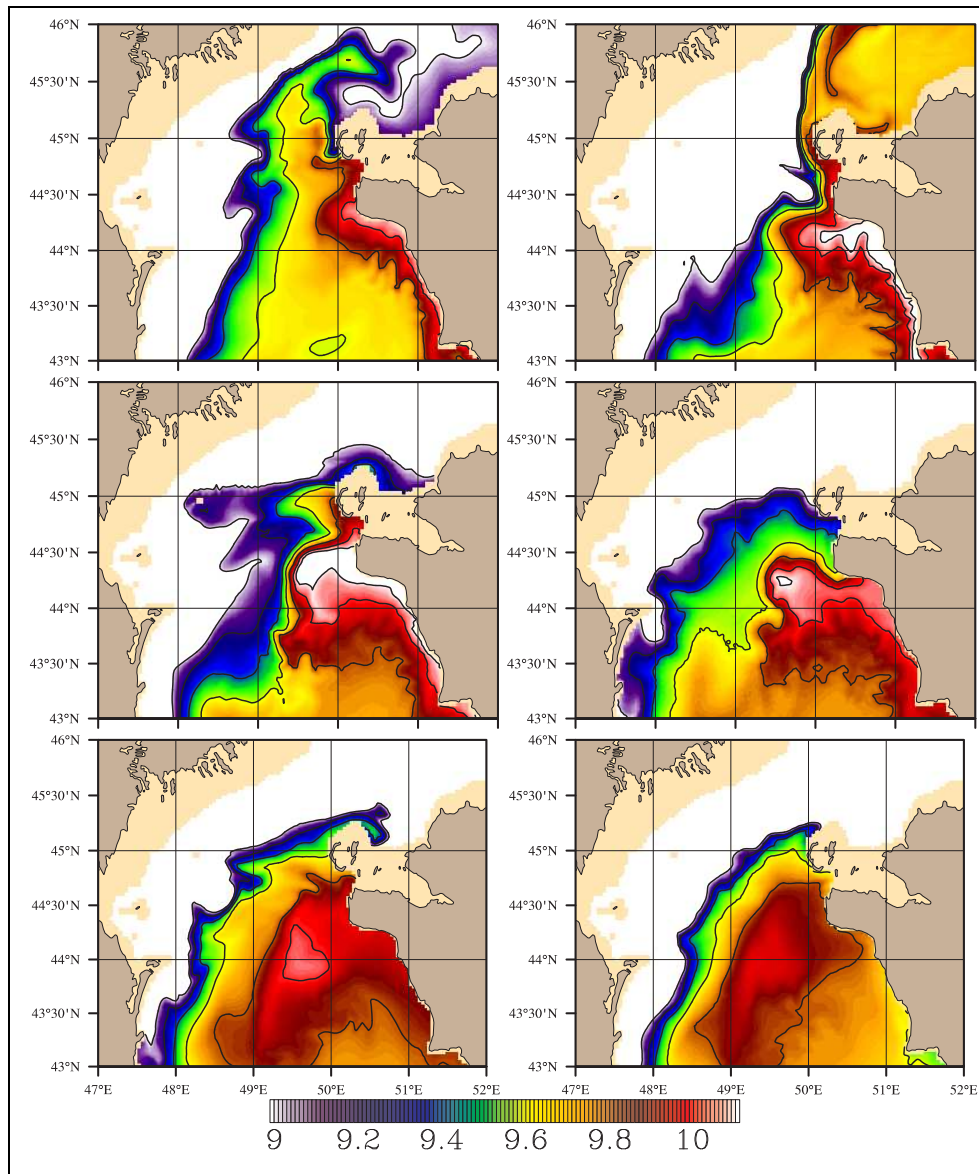


Figure 5.31: Density of deepest depth at model days 2, 20, 40, 60, 80, 100.
white areas shows the density less than 9

The effect of momentum and heat/salt fluxes at the sea surface is transmitted to the ocean by the surface mixed layer, where relatively uniform properties are generated by turbulent convection / mixing processes driven by cooling and wind stirring. The distribution of mixed-layer depth (MLD) generated by the model provides information on mixing processes and interesting features can often be found in maps of MLD. MLD is a diagnostic quantity calculated by detecting a specified density difference with respect to the surface along the vertical density profile. In our case, the MLD is defined to be the shallowest depth at which the density change with respect to the surface is the equivalent to that given by a temperature change of $0.2^{\circ}C$. (Kara et. al 2000)

Figure 5.32 shows the MLD for the Caspian Sea. The winter convection reaches about 120–150 m in the Middle Caspian Basin from December to April. The white areas show places where the mixed layer reaches to the bottom. In the Caspian Sea there are three types of convective mixing: polar, subpolar and subtropical (Zubov, 1947). Most of the basin experiences subpolar type of convection as a result of cooling of the surface waters in winter, this type of convection is evident along the eastern coast of the Middle and South Caspian Basins. A different type, called subtropical convection, occurs in the eastern part of the Southern Caspian Sea from August to October, as a result of the increase in salinity of the surface waters resulting from intensive evaporation in summer.

In summer there is strong stratification in Middle and Southern Caspian Sea with the thermocline located nearly at 50 m depth, clearly shown by the stratification in the meridional cross section at $51^{\circ}E$. In winter and early spring months (i.e December to March), temperature in the the Middle and Southern Caspian Sea corresponds to well mixed conditions, and in April the shallower part of the basin warms up first, with temperature increasing in the surface layer. Temperature stratification develops from April to September, and later surface cooling and convection starts to develop the surface mixed layer.

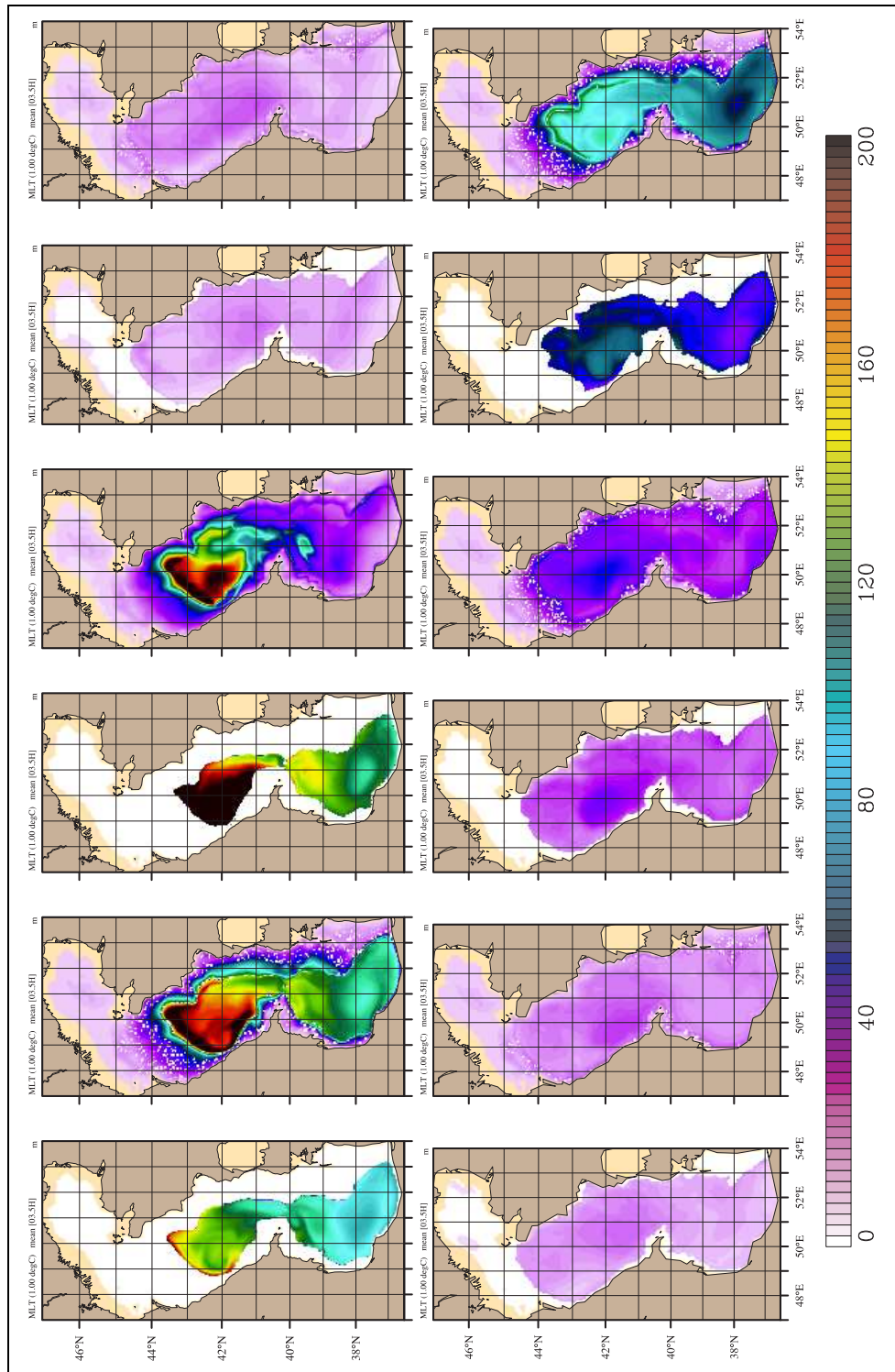


Figure 5.32: Mixed layer depth (m) of the control run from January to December

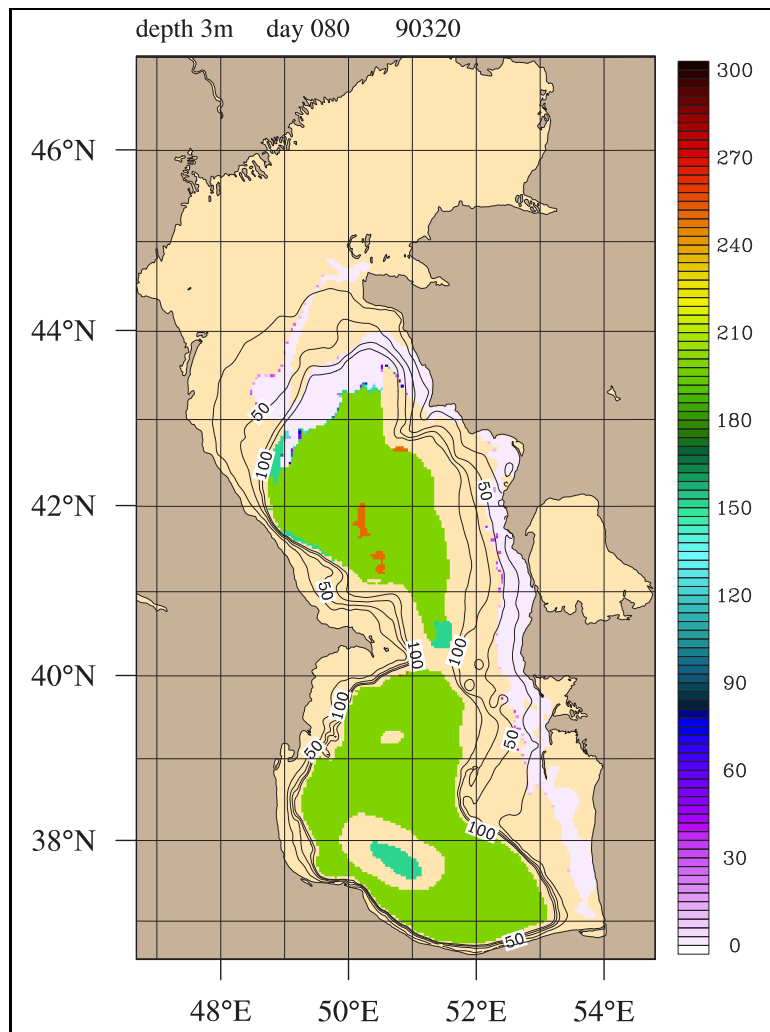


Figure 5.33: Depth of 9.8 density at the model day 80

In the previous section, the dense water was found to have a characteristic density of 9.8. Figure 5.33 shows the depth of 9.8 density on model day 80, revealing important features of the dense water process and its effect on the general circulation in the Caspian Sea. The most striking feature is that dense water is formed along whole shallow shelf zones of the eastern coast of the sea. There is no connection between the formed dense water and interior of the sea except in the northern end. The dense water formed along the eastern coast moves to the north and sinks there.

5.5.1 Effect of Freshwater and E-P on MLD

The effect of river runoff and the net water balance at the surface (evaporation minus precipitation: E-P) on the mixing and surface water properties of the Caspian Sea is investigated by conducting a series of experiments in this section. Rivers like Volga and Ural are the major sources of freshwater in the Caspian Sea. Freshwater affects the surface properties of the sea through changes it creates in the absorption of heat leading to changes in SST, and changes in the surface mixing properties. For example, in the Adriatic Sea, it has been argued that the dense water formation depends on the freshwater budget, which is linked to sea level change (Bethoux and Gentili 1994). Besides local atmospheric events, the change in dense water formation in the Mediterranean Sea may be a response to the preconditioning of surface water by the change in freshwater inputs (Bethoux and Gentili 1999).

Although some evidence has been found on the effect of Caspian Sea Level on the buoyancy of the sea and consequently on the vertical stratification, there is no detailed study investigating the effects of riverine input on the mixing properties of the Caspian Sea.

The rising of the Caspian Sea level is related with the increase in riverine inflow to the Caspian Sea from the Volga River. Peeters et al. (2000) have suggested that the decrease in buoyancy of the surface water following the rise in water level has affected the mixing of the sea. Such mixing has occurred in 1976, according to some evidence stating strong mixing in entire Middle Caspian Sea during the period. Since there is few data in winter, the proposed mechanism has not been proved yet.

To test this idea, a couple of sensitivity tests was conducted. Table 5.1 summarizes the test runs in detail. Expt 01 is the control run described earlier. Expt 02 is the same as Expt 01 but there is no relaxation of sea surface salinity in this run. Expt 03 is the twin of Expt 02 but no net surface flux due to Evaporation minus Precipitation (E-P) has been specified. Expt 04 is the twin of Expt 02 but there are no rivers. Expt 05 is the twin of Expt 02 but no E-P

and no rivers are specified.

Table 5.1: HYCOM simulations to test riverine input.

Expt	Description of the experiment
01	30 layer NCOM like HYCOM, sigma-z, KPP, variable kapref, ERA40-sea winds, thermal and precip forcing, initialize from January Russian climatology and No SSS relaxation
02	twin of 02 but NO E-P
03	twin of 02 but NO rivers
04	twin of 02 but NO E-P and NO rivers

Figure 5.34 shows plots of surface variables along the $50^{\circ}E$ transect in March. There is no significant change in SST and net heat flux in this month for all the experiments, because the salinity in the Caspian Sea is already low, and therefore freshening does not significantly influence heat absorbance. In the no river case (i.e.Expt 03), the salinity is much higher compared to standard run (Expt 01) as expected, the difference being significantly higher in the northern part. Mixed Layer depth (MLD) changes substantially between experiments stating the importance of freshwater flux to the mixing properties of the Sea. In the no river case, Expt 03, the MLD is deeper than the standard run (Exp 01). The MLD reaches a depth of about 200 m. in Expt 01, but in Expt 03, it deepens to more than 300 m. The difference is much higher in the Middle Caspian Sea compared to South Caspian Sea, since the freshwater from the Volga river has major influence in this part of the sea. Because the surface water budget of the Caspian Sea is positive (i.e. evaporation is greater than precipitation), surface salinity is lower in Expt 02, when E-P flux is nulled, compared to the standard run. When the E-P flux is added, the mixed layer depth (MLD) is increased.

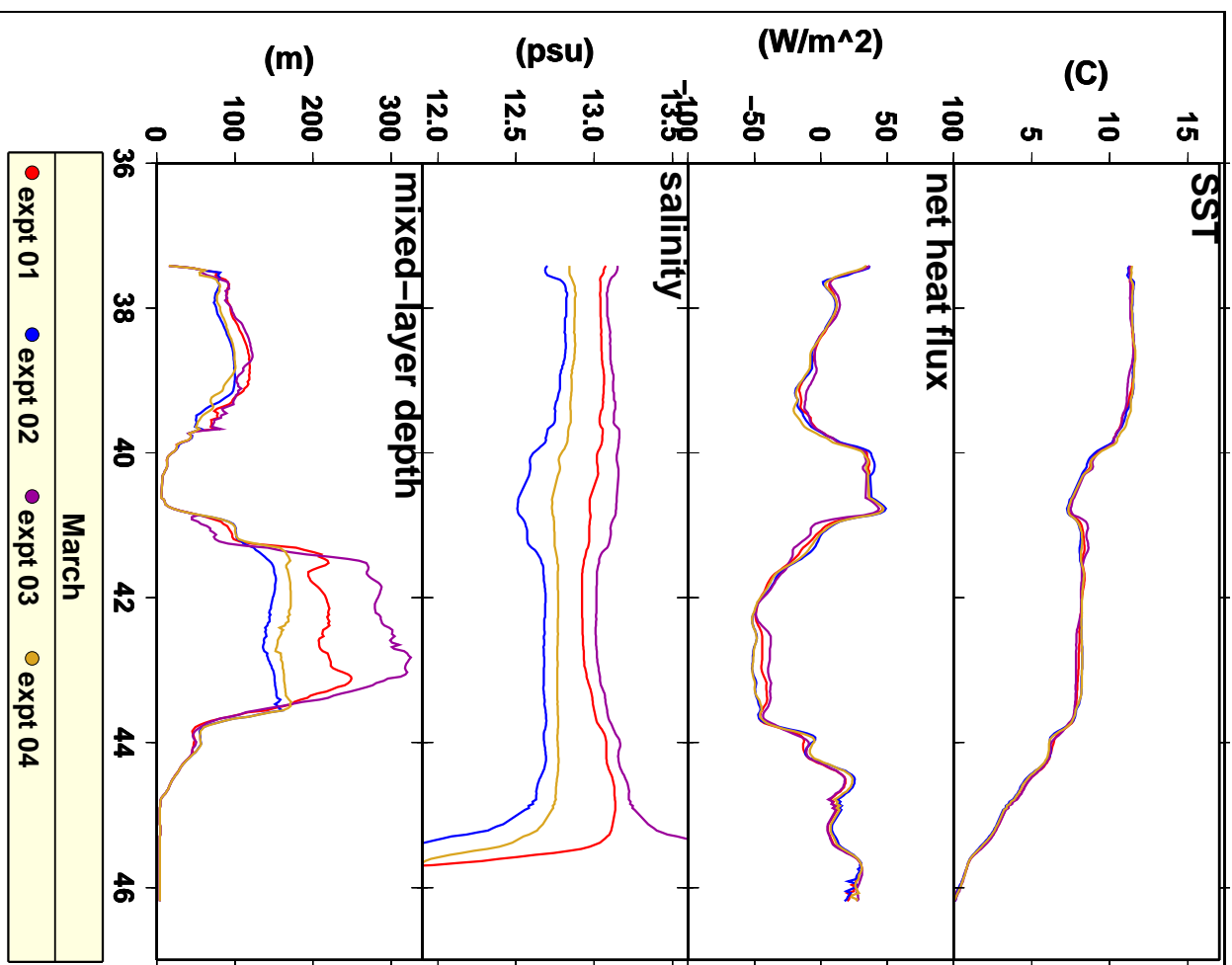


Figure 5.34: Meridionally averaged south-north cross sections of SST, net heat flux, salinity and Mixed Layer Depth (MLD) along the 50°E in March. The details of the each experiments are explained in the text.

The above experiments indicate the influence of the surface and riverine buoyancy fluxes on the MLD. It can be speculated that during low sea level (decreased Volga River input), mixing is less intense as a result of the lower stability of the water column associated with increased surface salinity. In the high sea level situation there exists less saline surface water and more intense mixing.

5.5.2 Float Experiments

In previous sections, it was shown that the eastern coast of the Caspian Sea is a dense water formation site. The float package of the HYCOM (Halliwell et. al 2003, the detailed description of the Float package can be found in Chapter 3 of this thesis) was used to investigate the timing and spatial extent of the dense water formation process along the eastern coast of the Caspian Sea. For the this purpose, a couple of experiments have been designed. Total 40 float which can move in three dimension have been released and the determined places shown in the Figure 5.35 covering the most of the coastal and interior of the Caspian Sea. The initial depth of the all floats were set to 5 m and all floats integrated 30 days from the beginning of the each month. After finishing the 30 day integration, floats were released again at the same positions as shown in Figure 5.35.

The role of the shallow eastern coast of the Caspian Sea as a possible site for the dense water formation has been emphasized earlier. The vertical temperature gradient in the eastern coast of the MCS is very weak due to the coastal upwelling along this coast. The vertical salinity gradient along the eastern coast of the SCS is also small due to the intensive evaporation in summer months. These conditions provide preconditioning for winter mixing and make the whole eastern coast of the Caspian Sea a suitable place for the development of dense water formation.

Figure 5.36 shows the trajectory of the float number 8 for the 30 days of integration beginning for three montsh (red, green, yellow corresponds to De-

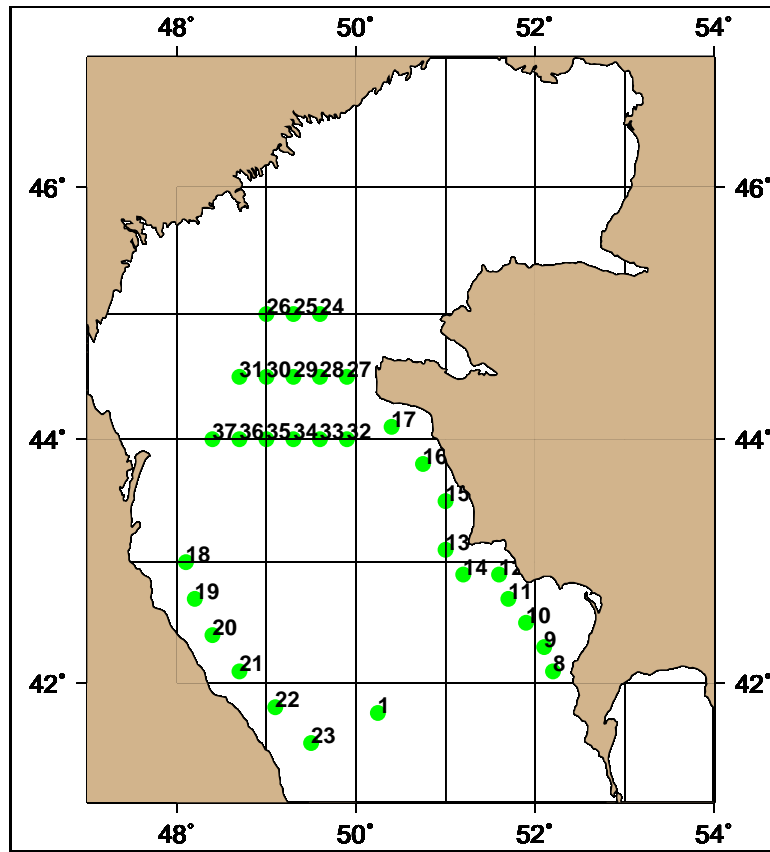


Figure 5.35: Float positions released in HYCOM, each float was integrated 30 days. The floats released again at the same location in each months. The floats can move in three dimension.

ember, January and February respectively). The important feature deduced from the deployed trajectories is the cyclonic movement of the trajectories without any sign of sinking (the floats flow the same depth as it is deployed) except the sinking of the three float at the upper northern part of the sea in December. It is concluded that December is the preconditioning month for dense water formation.

In January, Figure 5.36, the situation is different from December. All the floats along the eastern coast of the MCS sink suggesting the possible dense water formation site. The floats along the western coast of the Sea do not sink. The dense water formation in this coast is partly blocked by the intrusion of the freshwater from the Volga river.

In February, Figure 5.36 and Figure 5.37, the floats continue to sinking. Compared to January the floats sink more shallower depths. This month is the ending period of the dense water formation and after this months there is no evidence of formation of dense water.

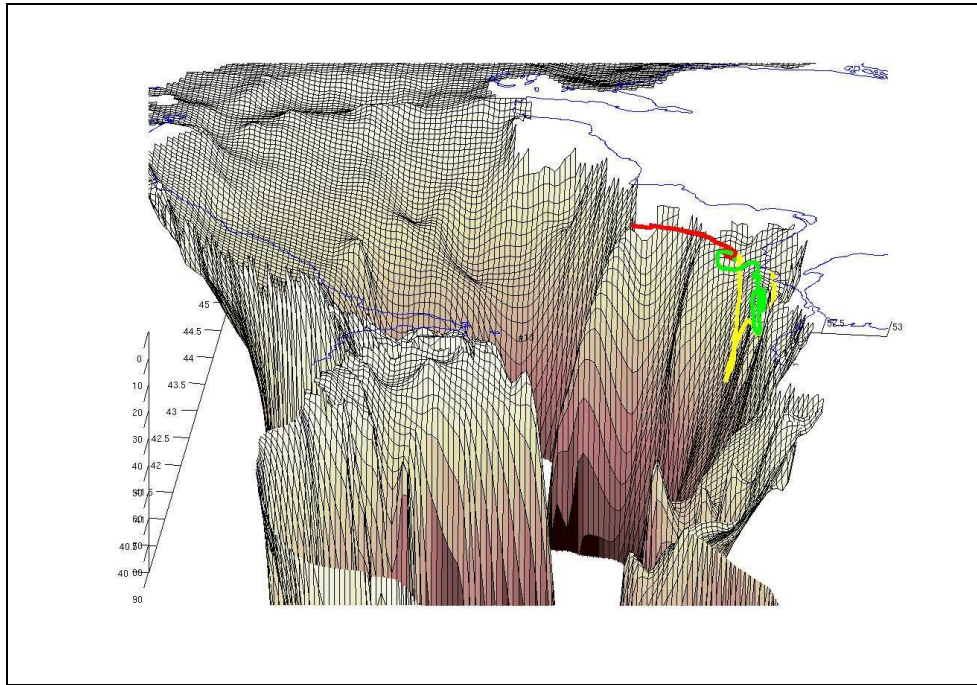


Figure 5.36: Float paths, color-coded to reveal months, red is December, green is January and yellow is February. Each float was integrated 30 days. The floats can move in three dimension.

In summary, float experiments help to prove the above proposed mechanism for the dense water formation in the Caspian Sea. While the float along the eastern coast directed toward to north in December, they begin to sink in January and this process continue to the end of the February.

The floats was also used to investigate the spatial extent of the upwelling over the eastern and western coast of the MCS. Figure 5.38 shows the float trajectories in July. The westard (eastward) Ekman drift at the sea surface is evident from the eastern (western) coast to the interior of the Sea. These

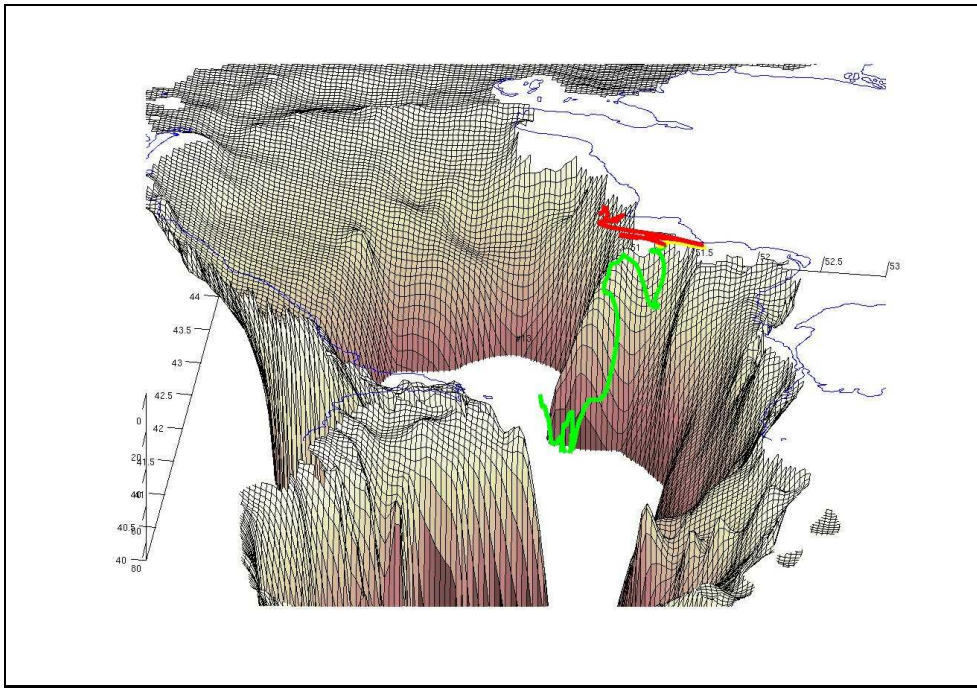


Figure 5.37: Float pats, color-coded to reveal monts, red is December, green is January and yellow is February. Each float was integrated 30 days. The floats can move in three dimension.

results proved that the origin of the cold water along the western coast of the sea is local upwelling not the soutward cold water originating from the northern Caspian Sea in summer.

Compared to eastern coast, upwelling along the western coast is more localized. Below 42° , the floats sink. Downwelling is evident at this latitude companseting the upwelling along the eastern coast.

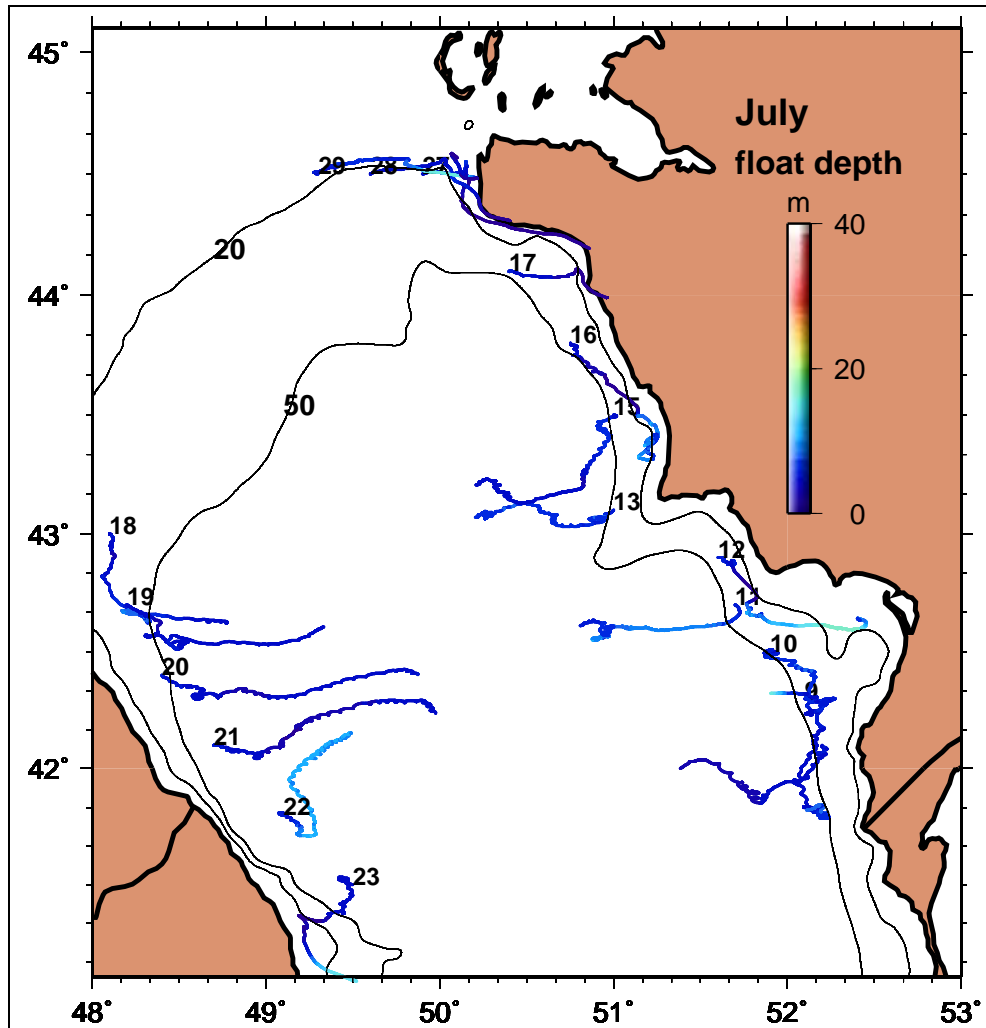


Figure 5.38: Float paths, color-coded to reveal depths along the paths, in July. The numbers indicate the release points of the floats. Each float was integrated 30 days. The floats can move in three dimension. The contours in the figure show the 20 m and 50 m depth.

CHAPTER 6

SENSITIVITY EXPERIMENTS

The effects of river discharge, surface buoyancy and momentum fluxes, and baroclinicity on the general circulation of the Caspian Sea was investigated through a number of numerical experiments in this Chapter. These experiments were designed to understand the relative importance of individual forcing mechanisms in driving the basin-wide and mesoscale circulation and to establish their roles on the intensity of upwelling / downwelling features, which are not yet fully understood.

The generation of the anticyclones along the western coasts of the MCS and the SCS appears related with downwelling along this coast to compensate for the eastern coast upwelling. These anticyclones were also observed in the model study by Schrum et al. (unpublished), which integrated the HAMSOM model in an interannual simulation using 6 hourly atmospheric forcing obtained from the 15 year ERA-15 re-analysis data set. Both HYCOM model results and those of Schrum show these features to have a typical seasonal signature.

In addition to the downwelling effect quoted above, generation of the anticyclonic circulation in the MCS could be aided by the density driven alongshore coastal jet, which follows the curved coastline towards the Apsheron peninsula. This jet advects less salty water towards the south and could have possible influence on the generation of the Derbent anticyclone. This hypothesis will be investigated in the sensitivity experiments.

6.1 Buoyancy effect

There is ample numbers of studies on buoyancy-driven currents generated by river discharges on continental shelf regions (e.g. Kourafalou et al. 1996, Lazure and Jegou 1998, Chen et al. 1999, Garvine 1999). In the Black Sea, the shelf circulation driven by freshwater inflow of the Danube river, comparable to the Volga in its volume flux, was studied by Oğuz et al. (1995), concluding that the lateral buoyancy forcing by the Danube and the Bosphorus are important factors for the mainly cyclonic general circulation of the Black Sea. It is known that the fresh water from rivers of the northern Aegean Sea influence of the circulation and hydrography of the Aegean Sea. The river runoff turns out to be very important in certain northern Aegean subbasins such as the Thermaikos Gulf (Kontoyiannis et al. 2003, Kourafalou et al. 2004), but the outflow of Black Sea originated relatively fresh water from the Dardanelles Strait is the most important buoyancy forcing, exceeding that of all rivers (Kourafalou and Barbopoulos 2003). A large number of rivers discharging into the Adriatic Sea similarly have significant influence on its circulation (Artegiani et al., 1997). In the Black Sea (coastal flow along the western continental shelf influenced by the Danube and other major rivers in the northwest), the Aegean Sea (the Evoia jet) and the Adriatic (the Po-river driven jet along the Italian coast), buoyancy driven coastal currents are unanimously generated. In all of these cases, as well as the Caspian Sea, the jet flow interacts with curved coastlines, headlands or peninsulae, sills and shelf topography, producing responses that seem to have some common features as well as differences corresponding to the actual conditions in which they are set.

The above common features observed in different seas guides us to investigate the effects of river-runoff on the circulation of the Caspian Sea. The generation of southward coastal jet-like flow along the western coast of the MCS appears to be forced by the buoyancy input from the Volga river, which is the most important source of freshwater in the entire Caspian Sea. To test this statement, an experiment was designed in which the river-runoff was

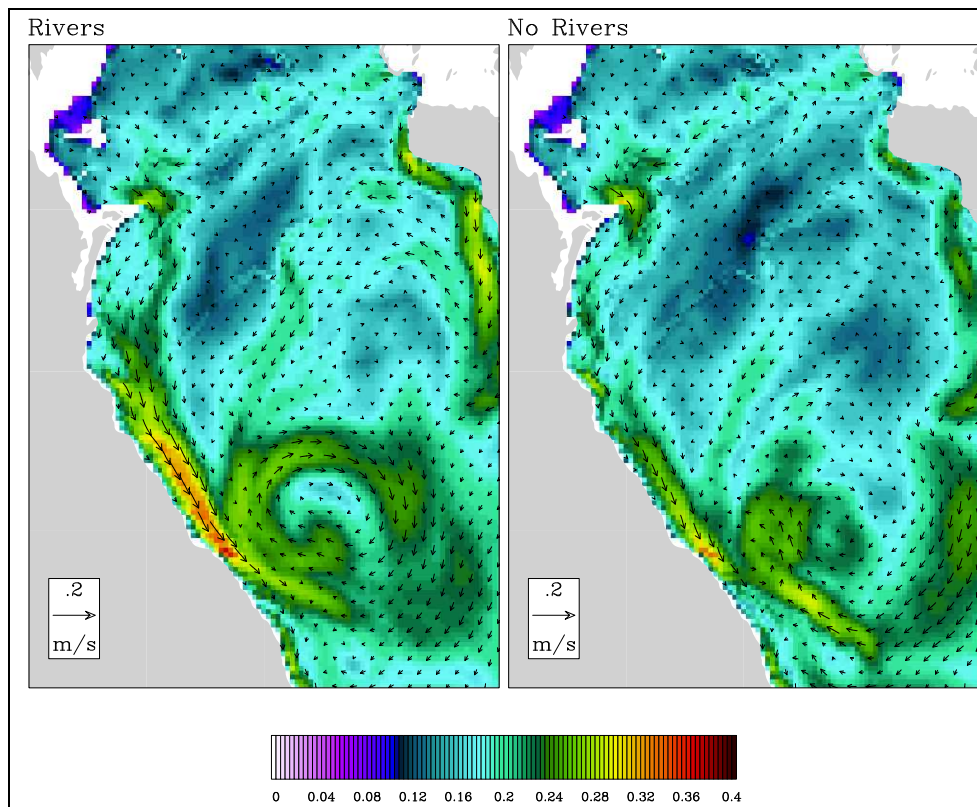


Figure 6.1: Model surface velocity vector mean and rms vector amplitude over the year simulation, with rivers and without rivers. Means are denoted with arrows while rms amplitude is color contoured. Every fourth vector is shown in the along-shore and across-shore direction.

switched off and the model was only forced with the climatological surface fluxes as in the control run.

Figure 6.1 shows the annual mean surface current and root mean square (rms) as a color contoured with and without rivers. The most striking contribution of the fresh water discharge is the generation of pronounced southward flowing current along the western coast of the MCS. This results show the relative influence of river run-off on the intensity of the coastal jet.

One of the generation mechanism for the anticyclonic gyre near the western part of the sea is the density-driven current along the western coast, which advects less salty water towards the south. Since this coastal jet less intense in without river simulation, the intensity of the anticyclonic gyre decrease also in

this simulation. Another important feature which can be detected from the Figure is the decrease in intensity of the current near the north-eastern coast of the basin. While it is transporting the waters of the NCS to the interior of the sea in river simulations, in no river simulation this current seems to be diminished partly.

In SCS, the cyclonic gyre in north-west part of the sea is very weak in no river runoff experiment during the whole year period. However, the basin-wide cyclonic gyre is more intense in no river simulation and follows the topography as in the control run.

Although the intensity of the coastal jet along the western coast of the basin decreases, it is not completely diminished stating the effects of other factors besides river run-off on the generation of this coastal jet. Wind could be another important mechanism driving the southward coastal current, the effect of wind on the general circulation of the Caspian Sea will be investigated in the next section.

6.2 Effects of wind stress and baroclinicity

To understand the relative contribution of the wind stress and baroclinicity in driving the climatological circulation, additional experiments have been carried out as described in Table 5.1. In experiment 2, a purely wind-driven and barotropic ocean is accomplished by switching off the surface thermohaline forcing and river runoff. Constant basin averaged temperature and salinity (5°C and 12 ppt) was used as initial conditions. Using this barotropic ocean, the driving of circulation was investigated by the wind stress excluding all other forcing mechanisms. Experiment 3 is the twin of the barotropic experiment (i.e. experiment 2) but instead of constant temperature and salinity initialization, the 3-D climatological temperature and salinity were used as initial conditions aiming to investigate baroclinic factors. Experiment 4 is the twin of the control run but with river runoff switched off. Table 5.1 summarizes all experiments.

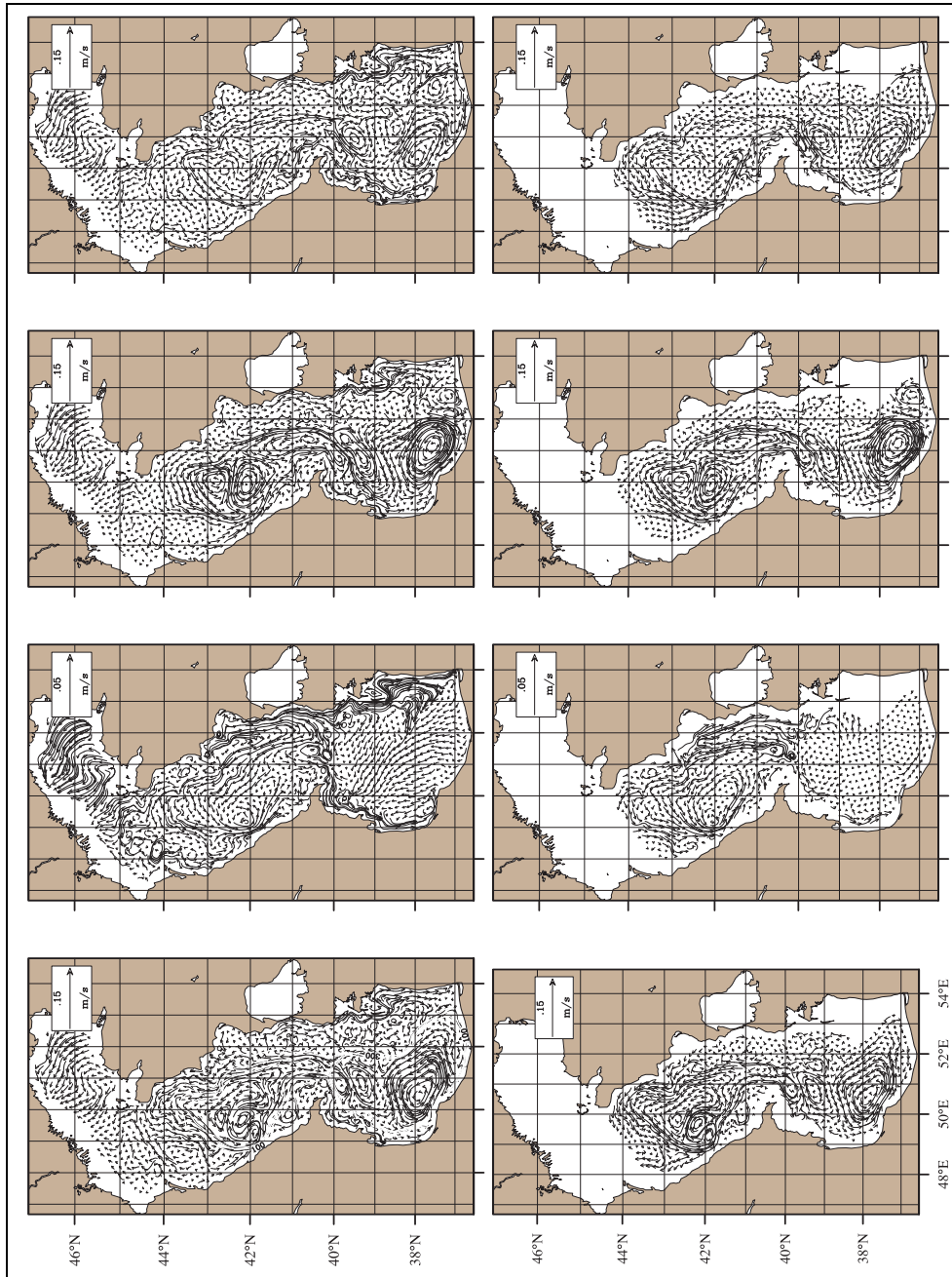


Figure 6.2: Circulation pattern averaged over different depth intervals in February for the four experiment mentioned in the text, upper figures 0-30m lower figures 30-150m

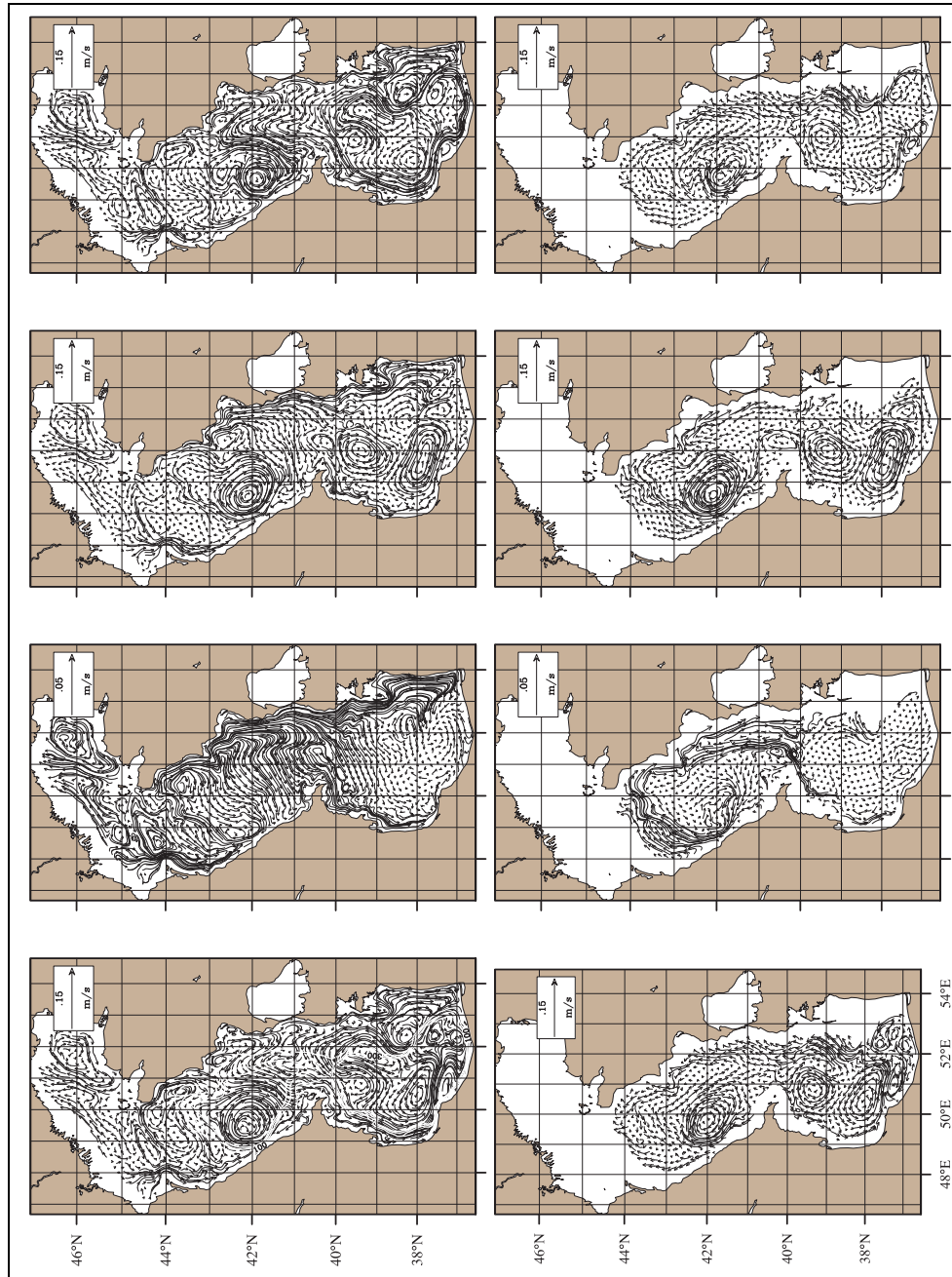


Figure 6.3: Circulation pattern averaged over different depth intervals in August for the four experiment mentioned in the text, upper figures 0-30m lower figures 30-150m

Figure Figure 6.2 and Figure Figure 6.3 show the comparison of the depth averaged circulation patterns for the above mentioned four experiments in February and August. In shallow northern basin the circulation pattern do not change too much in all four experiments. This suggest that the circulation mechanism controlling this shallow basin is purely wind stress and the effect of baroclinicity and other factors is minor.

The most striking feature of the wind-driven barotropic ocean circulation is relatively weak currents compared to control run except the southward coastal currents along the either coast of the Sea. As shown by various authots there is strong relationship between the wind and the currents along either side of the MCS. Thus the circulation is strongest in the extensive shallow shelf areas, taking the form of coastal jets in response to the wind stress. This southward currents are evident during the whole year period from surface until the 100 m depth which is the boundary of this current. It can be concluded that the southward shelf currents are the direct response of the wind driven Ekman transport.

In the interior of the basin, the circulation is dominated by westward and southwestward currents originating from the southward flowing jet along the eastern coast of the MCS. The most prominent feature of the deeper circulation of the wind driven-circulation experiment is the presence of a pair of counter-flowing current system along the eastern coast of the MCS. There is continous flow to the north passing Apsheron sill, the origion of this current is the north western coast of the SCS. In this experiment three anticylonic/cyclonic cell evident in the control run diminishes in the SCS and MCS basins stating the minor importance of the wind stress to generate these cells. The mechanism for generation of this dipole could be the variability in thermal forcing fields or baroclinic factors.

Experiment 3 which is the wind driven barolinic simulation shows very similar circulation pattern as the control run in the SCS and MCS stating the importance of baroclinicity in driving the seasonal circulation in this basins and

the minor importance of the thermal fluxes on the general circulation pattern in winter.

In all of the four experiment Ekman current due to the upwelling along the eastern coast preserved its structure, stating the dominant effects of this current.

Topography is another important factor affecting the general circulation pattern of the Caspian Sea, from above experiment it is obvious that after wind forcing generate the circulation, topography modify the currents. Most obvious evidence of the topographic influence is the Derbent depression in the western coast of the MCS, this current follows the constant depth and it thicken near the coast as bathymetry. But the affect of topography on the SCS circulation is minor. While barotropic ocean does not generate any significant circulation pattern in this basin, baroclinic run without thermal fluxes is very similar to the control run. Above fact state that the main mechanism for controlling the general circulation in the SCS is the baroclinicity not topography.

Above experiments shows that the driving mechanisms for the seasonal circulation of the Caspian Sea changes from basin to basin and each basin should be investigated seperately. Circulation in the Northern Caspian Sea is compliately wind driven due to its shallownest. In Middle Caspian Sea, wind, baroclinicity and bottom topography have an impact on the general circulation of the basin, thermal forcing is very weak compared to other forcings. In contrast, baroclinicity are the primary forcing field to form the general circulation pattern in the Southern Caspian Sea.

CHAPTER 7

LARGE SCALE CONTROLS

7.1 A possible link between North Sea Caspian Pattern (NCP) and SST over the Caspian Sea

The seas of the Euro-Asian-Mediterranean region are under the influence of large scale climatic variability associated with the atmospheric systems of North Atlantic and Eurasian regions. One of the most studied patterns in the region is the North Atlantic Oscillation (NAO). The influence of NAO on the Euro-Mediterranean region in winter is well known (Hurrell, 1995; Marshall *et al.*, 2001). Paz *et al.* (2003). Oguz *et al.* (2006) have found the combined effect of the NAO and North Sea Caspian Pattern (NCP) on the hydro-meteorological and ecological properties of the Black Sea. Ghasemi and Khalili (2007) have studied the effects of NCP on the winter temperature in Iran and concluded that NCP exerts significant influence on temperature variability. Gunduz and Ozsoy (2005) found the NCP to be the most important teleconnection pattern affecting the Euro-Mediterranean and Caspian regions. Their analysis based on the EOF (Empirical Orthogonal Functions) showed that wind stress, air temperature, and surface fluxes over the Caspian Sea is strongly affected by NCP.

We discuss here the effect of large scale weather patterns, such as those ex-

emplified by the NCP, on the Caspian Sea surface properties based on satellite SST data.

The correlation coefficient between the NCP index and SST for winter months of February-May has been calculated for the 20 year window of data available at each grid point in the Caspian Sea, as shown in Figure 7.1. This figure shows considerably high values of correlation between SST and the NCP index (up to ≈ 0.8) especially in the SCS where surface atmospheric fields associated with the pattern have most influence on SST. The correlations are very weak in the shallow northern part which is more often covered by clouds and also affected by ice formation and the consequent limitation of surface heat exchange.

One way to increase the statistical reliability of the correlation estimate is averaging over similar data points and eliminating of data low data quality flags. For this purpose, zonally averaged SST is calculated from data points with reliable quality flags, after which a better time series of quality controlled SST data for the 20 years of data available at each latitude. This considerably improves the space-time series on which the analysis is based. The computed correlation coefficient between the NCP and the zonally averaged SST in Figure 7.2 indicates correlation coefficient values of better than 0.6 at all latitudes of the MCS and SCS except for the shallow regions of the NCS north of the $44^{\circ}N$ latitude.

The lag correlations between NCP and SST with lag values of up to two months were also computed, but there was no significant improvement in correlation. It was also interesting to test correlation months window, and the correlation coefficient was found to decrease considerably when the month of January was added to the time series, most likely due to the -lack of SST data in this month. The same analysis was also made for other atmospheric teleconnection patterns like NAO and ENSO, but no significant correlation was found between SST and these large scale climate patterns.

Figure 7.3 shows the time series of SST (averaged zonally and over the

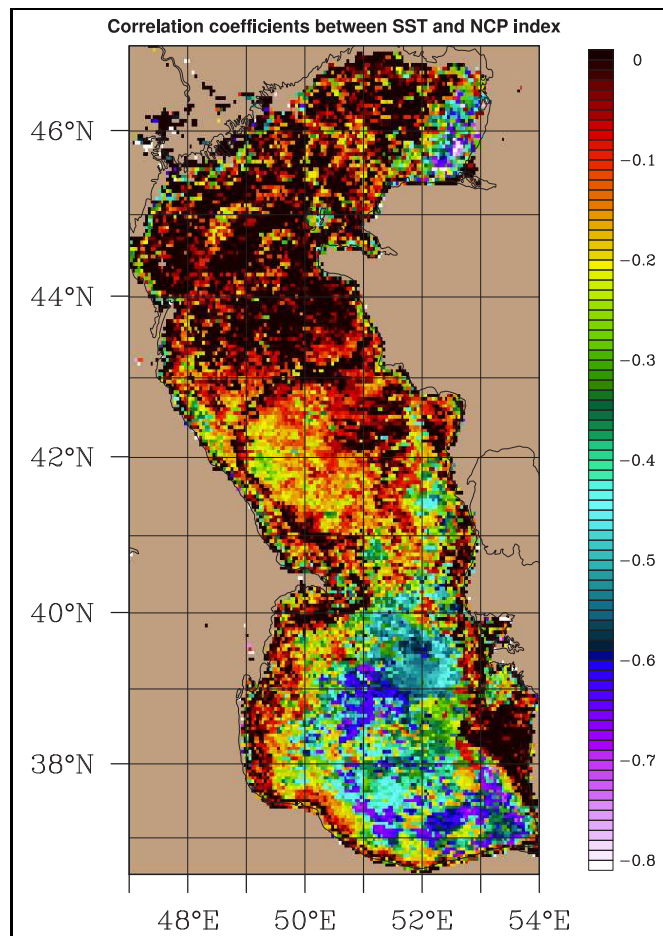


Figure 7.1: Correlation coefficients between moving averaged SST with 2 points and NCP index for the time period from February to May

36 – 38°N in the southern Caspian Sea) and the NCP index. The two time series follow each other, showing correspondence between warmer SST periods with negative NCP index and cold SST periods with positive NCP index. The correlation coefficient between these two time series is 0.5 for the entire length of record. However, considering only the period after 1990, the correlation increases dramatically to a value of 0.75.

Based on our analysis, it is found that NCP, which is one of the main atmospheric patterns affecting the study region, is highly correlated with the SST over the Caspian Sea in the February to May period.

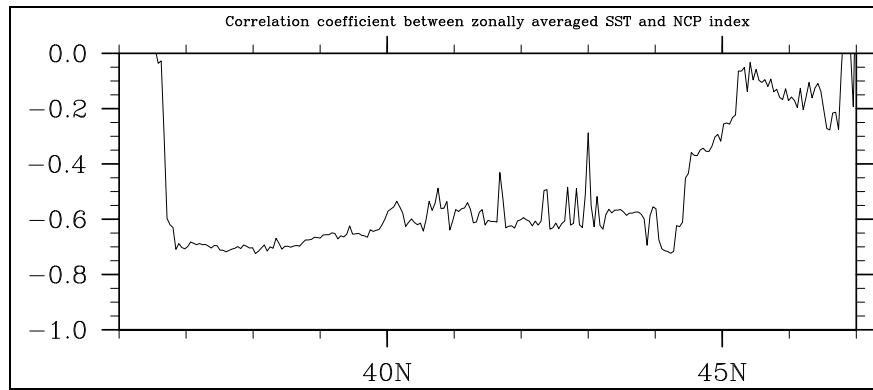


Figure 7.2: Meridional dependence of the correlation coefficient between zonally averaged SST of the Caspian Sea and the NCP index

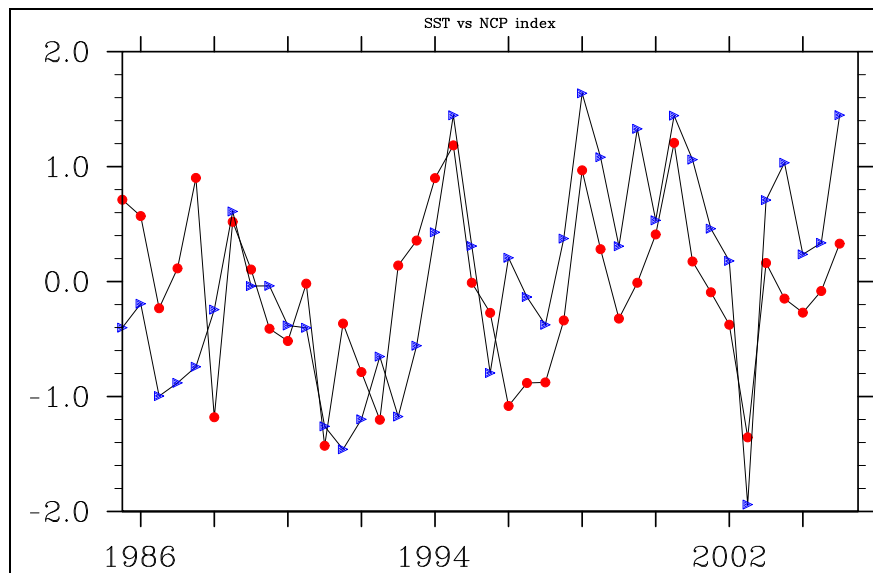


Figure 7.3: Time series of SST averaged meridionally and over the $36 - 38^{\circ}N$ (i.e southern Caspian Sea), blue triangles, and NCP index red dots. The time series was also moving averaged with a 2 point

CHAPTER 8

CONCLUSIONS

A high resolution ocean model (30 layers in the vertical and approximately 4 km horizontal resolution), available satellite data images (chl-a, SST and SSH), model trajectories and drifter observations were used together to deduce the flow characteristics and main ocean hydrodynamical processes. The model has been initialized and driven by climatological data to study the seasonal circulation and mixing characteristics as a first step to understand the physical variability of the Caspian Sea under real environmental conditions. This study represents one of the few opportunities for in-depth examination of the relevant processes, in the relatively poorly studied Caspian Sea.

Comparison of the seasonal evolution and the spatial structure of the model generated SST with the Pathfinder satellite climatology showed that the model reproduced the generally observed surface thermal structures: e.g. upwelling along the eastern coast, north to south gradient of the SST. The model sea surface height (SSH) results were also compared with sea level anomaly (SLA) obtained from altimeter measurements. Although these two data sets showed minor differences, it is shown that the large scale seasonal circulation structure of the Sea is captured by the model. The most important finding deduced from the SSH fields is the changing of circulation regime in the Middle Caspian Sea (MCS) from cyclonic in winter to anticyclonic in summer.

The main features of the general circulation in the Caspian Sea can be summarized as follows: There are southward coastal jets along either side of

the MCS. In sharp contrast to the surface southward current, an underlying northward current is evident below the mixed layer along the eastern coast. In fact, the orientation of currents also change in the offshore direction, changing with depth along the continental shelf/slope topography. This type of counter currents regime is typical of other upwelling systems such as the California Counter Currents (CCC) system. There is a basin wide shallow cyclonic circulation in the MCS and inside this gyre an anticyclonic circulation is observed. In the SCS, there is a dipole pattern, with an anticyclonic gyre in the deep northwestern part and a cyclonic gyre in the southern part that follows the coastline geometry. Although the model has been run with seasonal climatological forcing, there appears to be a very active meso-scale in most parts of the Caspian Sea. The energy in the meso-scale part of the spectrum can be expected to be much larger in realistic cases.

Three sensitivity experiments are conducted to investigate the factors driving the general circulation of the Caspian Sea. These experiments are 1- barotropic ocean, no heat fluxes, 2- baroclinic ocean, no heat fluxes 3- no river runoff. Based on these sensitivity tests, it is found that the baroclinicity is an important factor driving the general circulation of the Caspian Sea. Wind stress is the predominant forcing mechanism only in the shallow northern basin, and in the shallow coastal regions of the Sea. Although the river runoff is represented as an additional point source of surface fresh water without inducing a flux of momentum, the model seems to successfully reproduce the observed enhancement of currents along the western coast of the MCS induced by river runoff. The freshwater coming from the NCS creates density driven currents and enhances fluctuations in the surface current over the shelf along the western side of the MCS.

A set of experiments are conducted to understand the effects of buoyancy on the surface properties of the Caspian Sea. While the mixing properties of the sea change in accordance with the buoyancy forcing applied at the surface, the SST does not change significantly. Comparing the seasonal variation of

SST for different model runs, it is found that the buoyancy is not a key factor for the simulation of the SST.

One of the important ocean processes in the Caspian Sea is dense water formation. Until now, only hypotheses based on very limited observations existed for dense water formation. In this thesis, it is shown that dense water forms in the peak of winter along the entire eastern coast of the sea with a pre-conditioning period in December. Float experiments showed that the entire eastern coast of the Sea is suitable for dense water formation, as a result of preconditioning by upwelling and evaporation processes. The slope region connecting the shallow northern basin to the relatively deep MCS is also a topographically suitable region for dense water formation and overflow to deep water. The water sinking in this region flows westward following the bathymetry arriving at the interior of the MCS.

Based on our analyses, it is found that the North Sea - Caspian Pattern (NCP) which is one of the main atmospheric patterns affecting the study region is highly correlated with the Caspian Sea SST in the February to May period. The correlation strongly depends on the quality and availability of the SST data, which is partly blocked by cloudiness. If the reliability of the SST data is increased, for example by screening and zonal averaging, the correlations are also increased. The high correlation obtained over the southern Caspian Sea is partly related with less cloud cover in the region. No significant correlation could be found between Caspian Sea SST and other atmospheric indices such as the NAO or ENSO, suggesting that their far field effects do not seem to be significant for the Caspian Sea.

Further statistical analysis of the data seems to be needed, e.g. EOF analysis of the reconstructed SST to determine the main modes of variability in SST, canonical correlation analysis (CCA) between the SST and geopotential height fields, etc., to understand mutual interactions. The accurate prediction of the Caspian sea level (CSL) depends on the information on evaporation from the sea surface. Since the SST is one of the key factors to compute evaporation, the

relation between the geopotential height and SST stated in this thesis could be used to improve the quality of the CSL prediction.

The SST - NCP correlation decreases towards the north and along the coasts, most probably due to lack of satellite SST data in shallow regions. These findings are important, since it is shown for the first time in the Caspian Sea that there is strong relation with SST and 500 hPa geopotential height used in the calculation of the NCP index, and a main indicator of mid-tropospheric circulation in atmospheric models used to predict the future state of the climate.

Although the HYCOM Caspian Sea model reproduced the observed SST and SSH variability of the sea, it needs to be improved further to enable 1- forcing by a much finer resolution surface atmospheric fields, 2- realistic runs with interannual to daily and hourly scale forcing fields, 3- wetting/drying schemes to account for the effects of sea-level change in the flat regions surrounding the sea, such as along the northern coast.

The coarse resolution of the ECMWF atmospheric forcing (1.125 degree) is one of the limitations of the model. These data were the only available forcing with which to run the model at present. The space and time resolution of the forcing data is expected to significantly affect the properties of the upwelling region, the dense water formation, as well as the general circulation and mixing characteristics of the sea. In future studies, forcing by finer resolution hydrometeorological fields are needed. In fact, coupled models are needed for enclosed seas like the Caspian Sea to fully understand the hydrological cycle and dynamics of the basin including the surrounding land.

The impact of the interannual variations in the Caspian Sea is evident from observations. It is known that the mixing properties, the place of the upwelled waters of the sea can change from year to year. Since the Caspian Sea level experiences dramatic fluctuations in interannual time scales, a long time run (i.e 40 years) of the model with the available ECMWF data deserves attention in a future study. This simulation could be used to detect the interannual

variations of the general circulation, the effects of atmospheric teleconnections, and the variations in mixing properties of the sea.

REFERENCES

- [1] Arpe, K., Bengtsson, L., Golitsyn, G.S., Mokhov, I. I., Semenov, V.A. and Sporyshev, P.V., 2000: Connection between Caspian Sea Level variability and ENSO. *Geophysical Research Letters*, 27(17), 2693-2696.
- [2] Artegiani, A., Bregant, D., Paschini, E., Pinardi, N., Raicich F., and Russo, A., 1997: The Adriatic Sea general circulation. Part II: Baroclinic circulation structure, *Journal of Physical Oceanography* 27 (1997), pp. 1515-1532
- [3] Baidin, S., S., and Kosarev, A., N., 1986: The Caspian Sea. Hydrology and hydrochemistry., Nauka, Moscow (in Russian)
- [4] Barron, C. N., Kara, A. B., Martin, P. J., Rhodes, R. C., and Smedstad, L. F., 2006: Description and application of the global Navy Coastal Ocean Model (NCOM) with examination of vertical coordinate system choices. *Ocean Modelling*, 11, 347-375.
- [5] Baydin, S. S., and Kosarev, A. N. (Eds), 1986: The Caspian Sea. Hydrology and Hydrochemistry, Moscow, Nauka, 262 p. (in Russian).
- [6] Bethoux, J. P., and Gentili, B., 1994: The Mediterranean Sea, a test area for marine and climatic interactions. In: Malanotte-Rizzoli, P., Robinson, A.R. (Eds.), *Ocean Processes in Climate Dynamics: Global and Mediterranean Examples*. Kluwer Acad. Publ., pp. 239-254.

- [7] Bethoux, J. P., and Gentili, B., 1999: Functioning of the Mediterranean Sea, past and present changes related to freshwater input and climate evolutions. *Journal of Marine Systems*, 19, 33-47.
- [8] Bleck, R., 2006: On the use of hybrid vertical coordinates in ocean circulation modeling. In: *Ocean Weather Forecasting: An Integrated View of Oceanography*, Chassignet, E. P., and Verron, J., (Eds.), Springer, 109-126.
- [9] Bleck, R., 2002: An oceanic general circulation model framed in hybrid isopycnic-cartesian coordinates, *Ocean Modelling*, 4, 55-88
- [10] Bleck, R., Smith, L., 1990: A wind-driven isopycnic coordinate model of the north and equatorial Atlantic Ocean 1. Model development and supporting experiments. *Journal of Geophysical Research*, 95, 3273-3285
- [11] Bondarenko, A. L., Kosarev, A., N., 1990: On Certain Peculiarities of North Caspian Currents. *Caspian Sea. Structure and dynamics of water*. Nauka, Moscow.
- [12] Bondarenko, A. L., 1993: Currents of the Caspian Sea and formation of salinity field of the waters of the North Caspian Sea. Moscow, Nauka, 12p. (in Russian)
- [13] Buch, E., and She, J., 2005: Operational Ocean Forecasting at the Danish Meteorological Institute. *Environmental Research, Engineering and Management*, 3 (33), 5-11.
- [14] Chelton., D., B., 2005: The Impact of SST Specification on ECMWF Surface Wind Stress Fields in the Eastern Tropical Pacific. *Journal of Climate*, vol. 18, Issue 4, pp.530-550
- [15] Chelton, D., B., Esbensen, S., K., Schlax, M., G., Thum, N., Freilich, M., H., Wentz, F., J., Gentemann, C., L., McPhaden, M., J., Schopf, P., S., 2001: Observations of Coupling between Surface Wind Stress and Sea

- Surface Temperature in the Eastern Tropical Pacific. *Journal of Climate*, 14, 1479-1498.
- [16] Chen, C., Zheng, L., Blanton, J., 1999: Physical processes controlling the formation, evolution, and perturbation of the low-salinity front in the inner shelf off the Southeastern U.S.: A modeling study. *Journal of Geophysical Research*, 104, 1259-1288.
- [17] Chu, P. C., 1991: Geophysics of deep convection and deep water formation in oceans. In *Deep Convection and Deep Water Formation in the Oceans*, J.-C. Gascard and P. C. Chu, editors, volume 57 of Elsevier Oceanography Series, pages 197-213. Elsevier, Amsterdam.
- [18] Cushman-Roisin, B., 1994: *Introduction to Geophysical Fluid Dynamics*, Prentice Hall, 320 pp.
- [19] Ferronsky V.I., Brezgunov V.S., Vlasova L.S., Polyakov V.A., Froelich V.I., and Rozanski, K. 2003: Investigation of water exchange processes in the Caspian Sea on the basis of isotopic and oceanographic data. *Water Resources*, 30, (2003), 10-20
- [20] Ferry, N., Remy, E., Brasseur, P., and Maes, C., 2006: The Mercator global ocean operational analysis/forecast system: assessment and validation of an 11-year reanalysis. *Journal of Marine Systems*, in press.
- [21] Garvine, R. W. 1999: Penetration of buoyant coastal discharge onto the continental shelf. *Journal of Physical Oceanography*, 29:1892-1909.
- [22] Gawarkiewicz, G., 1991: Linear Stability Models of Shelfbreak Fronts. *Journal of Physical Oceanography*, Vol 21, 471-488.
- [23] Ghasemi, A. R., Khalili, D., 2007: The effect of the North Sea-Caspian pattern (NCP) on winter temperatures in Iran. *Theoretical and Applied Climatology*, doi:10.1007/s00704-007-0309-1

- [24] Gunduz M. and Ozsoy E., 2005: Effects of the North Sea Caspian Pattern on Surface Fluxes of Euro-Asian- Mediterranean Seas, *Geophys. Res. Letters*, 32, L21701, doi: 10.1029/2005GL024315.
- [25] Hallberg, R., 2000: Time integration of diapycnal diffusion and Richardson number dependent mixing in isopycnal coordinate ocean models. *Monthly Weather Review* Vol.128, 1402-1419
- [26] Halliwell, Jr., G. R., R. H. Weisberg, and D. A. Mayer, 2003: A synthetic float analysis of upper-limb meridional overturning circulation interior ocean pathways in the tropical/subtropical Atlantic. *Interhemispheric Water Exchange in the Atlantic Ocean*, G. Goni and P. Malanotte-Rizzoli, editors, Elsevier Publishing Company, 93-136.
- [27] Johnson, D.R., Boyer, T., P., Garcia, H., E., Locarnini, R., A., Mishonov, A., V., Pitcher, M., T., Baranova, O., K., Antonov, J., I., and Smolyar, I., V., 2006: World Ocean Database 2005 Documentation. Ed. Sydney Levitus. NODC Internal Report 18, U.S. Government Printing Office, Washington, D.C., 163 pp, Available at <http://www.nodc.noaa.gov/OC5/WOD05/docwod05.html>.
- [28] Kara, A., B., Rochford, P., A., and Hurlburt, H., E., 2000: An Optimal Definition for Ocean Mixed Layer Depth *Journal of Geophysical Research* vol. 105, no C7, 16,803-16,821
- [29] Kara, A., B., Rochford, P., A., and Hurlburt, H., E., 2002: Air-sea flux estimates and the 1997-1998 ENSO event. *Boundary - layer meteorology*. 103, 439-458
- [30] Kara, A., B., Wallcraft, A., J., and Hurlburt, H., E., 2003: Climatological SST and MLD predictions from a global Layered Ocean Model with an embedded mixed layer. *Journal of atmospheric and oceanic technology*, 20, 1616-1632

- [31] Kara, A., B., Wallcraft, A., J., and Hurlburt, H., E., 2005a: How Does Solar Attenuation Depth Affect the Ocean Mixed Layer? Water Turbidity and Atmospheric Forcing Impacts on the Simulation of Seasonal Mixed Layer Variability in the Turbid Black Sea. *Journal of Climate*, 18, 389-409
- [32] Kara, A., B., Wallcraft, A., J., and Hurlburt, H., E., 2005b: A New Solar Radiation Penetration Scheme for Use in Ocean Mixed Layer Studies: An Application to the Black Sea Using a Fine-Resolution Hybrid Coordinate Ocean Model (HYCOM) *Journal of Physical Oceanography* vol 35, 13-32
- [33] Kara, A., B., Hurlburt, H., E., Wallcraft, A., J., Bourassa, M., A., 2005c: Black Sea Mixed Layer Sensitivity to Various Wind and Thermal Forcing Products on Climatological Time Scales *Journal of Climate* vol. 18 5266-5293
- [34] Klevtsova, N., D., 1967, Sea currents regime near east coast of the Middle and South Caspian Basins, In: *Proceeding of Baku Hydrometeobservatory*, Baku, Issue 3, 44-49. (in Russian)
- [35] Klevtsova, N., D., 1968, Sea currents near west coast of the Middle and South Caspian Basins In: *Proceeding of Baku Hydrometeobservatory*, Baku, Issue 4, 153-159. (in Russian)
- [36] Klinge, R., K., Myagkov, M., S., 1995: Changes in the water regime of the Caspian Sea. *Geojournal* 23, 299-307
- [37] Kontoyiannis, H., Kourafalou, V. H., Papadopoulos, V., 2003: The seasonal characteristics of the hydrology and circulation in the northwest Aegean Sea (eastern Mediterranean): Observations and modeling. *Journal of Geophysical Research*, 108, 3302, doi:10.1029/2001JC001132.
- [38] Kosarev, A. N., and Tuzhilkin, V. S., 1995: Climatic Thermohaline Fields of the Caspian Sea (GOIN, MGU, Moscow) (in Russian).

- [39] Kostianoy A., Lebedev S. 2006: Satellite altimetry of the Caspian Sea / 15 Years of Progress in Radar Altimetry Symposium, Venice Lido, Italy, 13-18 March, 2006. Abstract Book. P. 56.
- [40] Kostianoy A., Kosarev A., (eds) 2005: The Handbook of Environmental Chemistry. Vol. 5, Part P. The Caspian Sea Environment. Springer Verlag. Berlin.
- [41] Kourafalou, V. H., Oey, L. Y., Wang, J. D., Lee, T. N., 1996: The fate of river discharge on the continental shelf. 1. Modeling the river plume and inner shelf current. *Journal of Geophysical Research*, 101, 3415-3434.
- [42] Kourafalou, V. H., Barbopoulos, K., 2003: High-resolution simulations on the North Aegean Sea seasonal circulation. *Ann. Geophys.*, 21, 251-265.
- [43] Kourafalou, V. H., Savvidis, Y. G., Koutitas, C., G., Krestenitis, Y., N., 2004: Modeling studies on the processes that influence matter transfer on the Gulf of Thermaikos (NW Aegean Sea). *Continental Shelf Research*, 24, 203-222.
- [44] Kosarev, A., N., Tsiganov, V., F., 1972: Some Statistical Characteristics of the Caspian Level Fluctuations. *Meteorologiya i gidrologiya* no.2, pp. 49-55.
- [45] Kosarev, A., N., 1975: Hydrology of the Caspian and Aral Seas. Mosk Gos Univ, Moscow. (in Russian)
- [46] Kosarev, A., N., 1990: The Caspian Sea. Water structure and dynamics. Nauka, Moscow (in Russian)
- [47] Kosarev, A., N., and Yablonskaya, E., A., 1994: The Caspian Sea, SPB Academic Publishing, The Hague, 259 pages.
- [48] Kosarev, A., N. and Tuzhilkin, V., S., 1995: Climatological thermohaline fields of the Caspian Sea. Moscow University Press and State Oceanographic Institute, Moscow (in Russian)

- [49] Kutiel, H., Benaroch, Y., 2002: North Sea-Caspian Pattern (NCP) - an upper level atmospheric teleconnection affecting the eastern Mediterranean: Identification and definition. *Theoretical and Applied Climatology*, 71, 17-28.
- [50] Kutiel, H., Maheras, P., Turkes, M., Paz, S., 2002: North sea-Caspian Pattern (NCP) - an upper level atmospheric teleconnection affecting the eastern Mediterranean: Implication on the regional climate., *Theoretical and Applied Climatology*, 72, 173-192
- [51] Large, W., G., McWilliams, J., C., Doney, S., C., 1994: Oceanic vertical mixing: A review and model with a nonlocal boundary layer parameterization. *Reviews of Geophysics*, 32, 363-403
- [52] Lazure, P., Jegou, A. M., 1998, 3D modelling of seasonal evolution of tLoire and Gironde plumes on Biscay Bay continental shelf. *Oceanologia Acta*, 21, 165-177.
- [53] Leveque, R., L., 2002: *Finite Volume Methods for Hyperbolic Problems*. Cambridge University Press, 578 p.
- [54] Michael, J. B., Barciela, R., Hines, A., Martin, M., McCulloch, M., Storke, D., 2006: The Forecasting ocean asssimilation model (FOAM) system. In: *Ocean Weather Forecasting: An Integrated View of Oceanography*, Chassignet, E. P., and J. Verron (Eds.), Springer, 109-126.
- [55] Morel, Y.,G., Darr, D.,S., Talandier, C., 2006: Possible Sources Driving the Potential Vorticity Structure and Long-Wave Instability of Coastal Upwelling and Downwelling Currents. *Journal of Physical Oceanography* 36(5): 875
- [56] Murphy, A., H., 1992: Climatology, persistence, and their linear combination as standards of reference in skill skores, *Weather and Forecasting*, 7, 692-698

- [57] Nihoul, J.C.J., Zavialov, P.O., Micklin, P.P. (Ed.). 2004: Dying and dead seas: climatic versus anthropic causes: proceedings of the NATO Advanced Research Workshop, Liège, Belgium, 7-10 May, 2003. Nato Science Series: 4. Earth and Environmental Sciences, 36. Kluwer Academic Publishers: Dordrecht, The Netherlands. ISBN 1-4020-1902-5. viii, 384 pp.
- [58] Oguz, T., Dippner, J. W., Kaymaz, Z. 2006: Climatic Regulation of the Black Sea hydro-meteorological and ecological properties at interannual-to-decadal time scales. *Journal of Marine Systems*, 60,235-254.
- [59] Özsoy, E., On the Atmospheric Factors Affecting the Levantine Sea. European Centre for Medium Range Weather Forecasts, Reading, Berkshire, UK, Technical Report No.25, 29pp.
- [60] Özsoy, E. and Ünlüata, Ü., 1997: Oceanography of the Black Sea:a review of some recent results. *Earth Science Review*. 42, 231-272,1997
- [61] Özsoy, E., 1999: Sensitivity to Global Change in Temperature Euro-Asian Seas(The Mediterranean, Black Sea and Caspian Sea):A Review, in P. Malanotte-Rizzoli and V.N. Eremeev, (editors) *The Eastern Mediterranean as a Laboratory Basin for the Assessment of Contrasting Ecosystems*, NATO Science Series 2, Environmental Security ,51, Kluwer Academic Publishers, Dordrecht, pp. 281-300
- [62] Peffley, M. B. and O'Brien, J. J., 1976: A three-dimensional simulation of coastal upwelling off Oregon. *Journal of Physical Oceanography*, 6:164-180.
- [63] Pinardi, N., Allen, I., Demirov, E., De Mey, P., Korres, G., Lascaratos, A., Le Traon, P. Y., Maillard, C., Manzella, G., and Tziavos, C., 2003: The Mediterranean ocean Forecasting System: first phase of implementation (1998-2001). *Annales Geophysicae*, 21, 3-20.
- [64] Polonsky, A., Voskresenskaya, E., Belokopytov, V., Variability of North-western Black Sea Hydrography and River Discharges as a part of Global

Ocean-Atmosphere Fluctuations. - In book: Sensitivity to Change: Black Sea, Baltic Sea and North Sea (Edited by E.Ozsoy and A.Mikaelyan). NATO ASI Series.- 2. Environment-1997, Vol.27,.11-24.

- [65] Pringle, J.M., 2002: Enhancement of Wind-Driven Upwelling and Downwelling by Alongshore Bathymetric Variability. *Journal of Physical Oceanography*, 32, 3101-3112.
- [66] Rachev, N., H., and Stanev, E., V., 1997: Eddy processes in semi-enclosed seas. A case study for the Black Sea. *Journal of Physical Oceanography* 27, pp. 1581-1601.
- [67] Rodionov, S., N., 1994: Global and regional climate interaction:the Caspian Sea experience, 241 pp., Kluwer Academic Publ., Dordrecht, The Netherlands.
- [68] Sanson, Z., L., Serravall, R., Carnevale, G., F., van Heijst, G., J., F., 2005: Experiments and simulations on coastal flows in the presence of a topographic slope. *Journal of Physical Oceanography*, 35, 2204-2218.
- [69] Smagorinsky, J., S., 1963: General circulation experiments with the primitive equations. I: The basic experiment. *Monthly Weather Review*, 91, 99-164
- [70] Song, Q., Cornillon, P., Hara, T., 2006: Surface wind response to oceanic fronts, *J. Geophys. Res.*, 111, C12006, doi:10.1029/2006JC003680.
- [71] Stockman, W., 1938: Investigation of current kinematics at the western shore of the central part of the Caspian Sea. *Transactions of the Azerbaidjan Scientific-Investigative Fishery station*. Vol 1, Baku, 76 p. (in Russian)
- [72] Sur, H. Ä°, Ozsoy E., Ibrayev R., 2000: Satellite - Derived Flow Characteristics of the Caspian Sea, in: D. Halpern (editor), *Satellites, Oceanography and Society*, Elsevier Oceanography Series, 63, Elsevier, pp. 289-297.

- [73] Tatli, H., 2007: Synchronization between the North Sea spian pattern (NCP) and surface air temperatures in NCEP. *International Journal of Climatology* 27(9): 1171
- [74] Terziev, F., S., Kosarev, A., N., Keromov, A., A., (Eds.) 1992: Hydrometeorology and hydrochemisrtry of Seas. Vol VI, Caspian Sea. Issue 1, Hydrometeorological conditions, Hydrometeoizdat, 359 p. (in Russian)
- [75] Trukhchev D. I., Kosarev A. N., Ivaniva D., Tuzhilkin V. S., 1995: *C R Acad Bulg Sci* 48:31
- [76] Tsytsarev, A. N., 1967: Peculiarities of drift currents near Kura river mouth, In: *Proceeding of Baku Hydrometeobservatory, Baku, Issue 3*, 50-57. (in Russian)
- [77] Tuzhilkin V.S., Kosarev A. N., Trukhchev D. I., Ivanova D. P., 1997: *Meteorol Gidrol* 1:91 (in Russian)
- [78] van Leer, B., 1977: Towards the ultimate conservative difference scheme IV. A new approach to numerical convection. *Journal of Computational Physics*, 23, 276-299.
- [79] Vilibic, I., Grbec, B., Supic, N., 2004: Dense water generation in the north Adriatic in 1999 and its recirculation along the Jabuka Pit. *Deep-Sea Research I*, 51, 1457-1474.
- [80] Vilibic, I., Supic, N., 2005: Dense water generation on a shelf: the case of the Adriatic Sea. *Ocean Dynamics*, DOI 10.1007/s10236-005-0030-5.
- [81] Vörösmarty, C., J., Sharma, K., Fekete, B., M., Copeland A., H., Holden, J., Marble, J., Lough, J., A., 1997: The storage and aging of continental runoff in large reservoir systems of the world. *Ambio*, 26, 210-219
- [82] Wallcraft, A., J., Kara, B., A., Hullburt, H., E., Rochford, P., A., 2003: The NRL Layered Global Ocean Model (NLOM) with an embedded

mixed layer submodel: Formulation and tuning. *Journal of Atmospheric and Oceanic Technology*, 20, 1601-1615.

[83] Wallcraft, A. J., Kara, A. B., Hurlburt, H.E., Metzger, J. E., Chassignet, E. P., Halliwell, G. H., 2006: Value of Bulk Heat Flux Parameterizations for Ocean SST Prediction. Submitted to *Journal of Climate*.

[84] Zubov, N. N., *Dynamic Oceanology*. Gidrometeoizdat, Moscow-Leningrad, 1947, 430p

VITA

Murat Gunduz

Institute of Marine Sciences

Middle East Technical University (METU)

Phone: (90 324) 5213434, Fax: (90 324) 5212327

PK.28, 33731, Erdemli, Mersin, Turkey.

`gunduz@ims.metu.edu.tr`

Personel

Date of birth: July 05, 1979 Nationality: Turkish

Place of birth: Malatya, Republic of Turkey

Languages: Turkish (native), English (advanced)

Gender: Male Marital status: Single

Education

Ph.D. Physical Oceanography, METU

supervisor, Emin Ozsoy

Institute of Marine Sciences, METU, January 2008

Modelling seasonal circulation and thermal structure of the Caspian Sea by HYCOM model.

MSc. Physical Oceanography, METU

supervisor, Emin Ozsoy

Institute of Marine Sciences, METU, 2000–2002

Principal Component and time series analysis of air-sea interactions in the "seas of the old world"

B.S. Physics

Mersin University, 1995–1999

Research Experience

Summer Research Assistant

NATO, NURC, La Spezia, Italy, July–September 2006

Development of a new technique to improve the drawbacks of multi-model superensemble under the supervision of the Dr. Micheal Rixen.

Publications

Gunduz M., and Ozsoy E., 2007, A possible link between North Sea Caspian Pattern (NCP) and SST over the Caspian Sea. *in progress*.

Gunduz M., and Ozsoy E., 2005, Effects of the North Sea Caspian Pattern on Surface Fluxes of Euro-Asian- Mediterranean Seas. *Geophys. Res. Letters*. L21701, doi: 10.1029/2005GL024315

Gunduz M., and Ozsoy E., 2003, Climate variability of the Eastern Mediterranean and Black Sea based on empirical orthogonal functions (EOFs) analysis. *Oceanography of the Eastern Mediterranean and Black Sea*. Ed. Yilmaz A., 2003 TÜBİTAK Publisher. Pp.162-167

Posters/Oral Presentations

Gunduz M., Kara B., Wallcraft A., Metzger J., 2007 Application of the Creeping Sea-Fill Methodology to the wind speed over the Caspian Sea. *Rapp. Comm. Int. Mer Medit*. Vol. 38 - page 155 38th CIESM Congress 9-13 April 2007, Istanbul -Turkey

Ibrayev R., Sattarzade R., Gunduz M., Romanets A., Sarkisyan A., Ozsoy E., Towards Climatic Modelling of the Caspian Sea Thermo-Hydrodynamics.

Gunduz M., Ozsoy E., Effects of the North Sea Caspian Pattern on Surface Fluxes of Euro-Asian-Mediterranean Seas. European Geosciences Union General Assembly 2006 Vienna, Austria, 02 - 07 April 2006.

Gunduz M., Ozsoy E., Climate variability of the Mediterranean and Black Sea based on empirical orthogonal functions (EOFs) analysis (314). Oceanography of the Eastern Mediterranean and Black Sea: Similarities and Differences of two interconnected Basins. 14-18 October 2002, Ankara, Turkey

Computing skills

Linux, Unix, Matlab, Fortran, L^AT_EX

Ferret, Generic Mapping Tools (GMT), NCAR Command Language (NCL),
Windows, Word, Excel, Powerpoint

Projects Involved

NATO SfP PROJECT No:981063

"Multidisciplinary Analysis of the Caspian Sea Ecosystem" (MACE)

Tubitak PROJECT 05G029

"Meteorology / Oceanography Network of Excellence" (MOMA) Pilot Project:
Development of Satellite and in-situ Observation, Data Assimilation, Prediction, Early Warning and User Services.

SESAME

Southern European Seas : Assessing and Modelling Ecosystem changes

Participated Major Research Cruises

Participated in several research cruises onboard R/V Bilim covering the seas of Turkey (Black Sea, Aegean Sea, Marmara Sea and Eastern Mediterranean Sea). Experience in handling and processing of various oceanographic instruments such as CTD, ADCP, XBT and drifters.

Recently attended cruises:

R/V Bilim – 2007

for the Project 104Y277, Chief Scientist: Zahit Uysal (METU-IMS),
Eastern Mediterranean, January 10–17 2007.

R/V Bilim – 2007

for the Project SESAME, Chief Scientist: A.C. Gucu (METU-IMS),
Sea of Marmara, Bosphorous March 16–21 2007.

R/V Bilim – 2007

for the Project ASCABOS, Chief Scientist: Erhan Mutlu (METU-IMS),
Black Sea, May 7–23 2007

Attended Schools/Courses

Summer School, Climate Changes Impact on Marine Ecosystems

14 - 26 August 2006, Ankara, Turkey

NATO ASI Summer School, Seasonal to Interannual Climate Variability:
its Prediction and Impact on Society

23 May - 3 June 2005, Gallipoli, Italy

GODAE International Summer School of Oceanography An Integrated
view of Oceanography:

Ocean Weather Forecasting in the 21st Century.

20 September - 1 October 2004, Lalonde les Maures, France